Exploitation of Jet Properties for Energy Scale Corrections for the CMS Calorimeters

Diplomarbeit
am Institut für Experimentalphysik
Universität Hamburg

Henning Kirschenmann

Abgabedatum:
14. Dezember 2010

1. Gutachter:
Prof. Dr. Peter Schleper
2. Gutachter:
Prof. Dr. Robert Klanner

Zusammenfassung

Jets sind wichtige Ereignissignaturen in Proton-Proton-Kollisionen am LHC[1] und die genaue Messung ihrer Energie ist eine Grundvoraussetzung für eine Vielzahl physikalischer Studien.

Jets, die nur auf der Basis von Kalorimetermessungen rekonstruiert werden, sind bisher innerhalb der CMS-Kollaboration[2] auf breiter Front für Analysen eingesetzt worden. Allerdings hängt das Antwortverhalten der Kalorimeter für eintreffende Teilchen stark von deren Energie ab und darüber hinaus wurde bereits bei früheren Experimenten festgestellt, dass sich für Jets, abhängig davon ob sie durch leichte Quarks oder Gluonen verursacht wurden, im Mittel die Multiplizität geladener Teilchen und die radiale Verteilung der Konstituenten stark unterscheiden. Zusammen mit der Nichtlinearität der CMS-Kalorimeter trägt dies zu einer im Mittel von Eins abweichenden Energieantwort für Kalorimeterjets verschiedenen Flavours bei.

In dieser Arbeit wird eine Jetenergiekorrektur beschrieben, die zusätzlich zu den standardmäßigen Energiekorrekturen der CMS-Kollaboration angewandt werden soll. Diese Korrektur zielt darauf ab, die „Flavour-Abhängigkeit“ der Energieantwort der Jets zu verringern und die Energieauflösung zu verbessern. Da viele verschiedene Effekte zur beobachteten Energieantwort von Jets beitragen, wird eine Reihe von Observablen eingeführt und Korrekturen, die auf diesen Observablen basieren, werden im Hinblick auf die vorher definierten Ziele untersucht. Eine Jetbreiten-Variable, die durch Messung der Energiedepositionen im Kalorimeter bestimmt wird, zeigt das beste Verhalten: Eine Korrektur, die auf dieser Observablen basiert, verbessert die Energieauflösung für Jets mit einem hohen Tranversalimpuls im zentralen Detektorbereich um bis zu 20% und verringert die Flavour-Abhängigkeit der Energieantwort von Jets um etwa die Hälfte. Mithilfe von Simulationen wird eine Parametrisierung der Korrektur abgeleitet und validiert. Zur Validierung der Korrektur werden auch erste Ergebnisse aus der Anwendung der Jetbreitenkorrektur auf Daten vorgestellt. Die vorgeschlagene Jetbreitenkorrektur zeigt auch hier eine deutliche Verbesserung der Energieauflösung.

---

[1] Large Hadron Collider

[2] Compact Muon Solenoid

Abstract

Jets form important event signatures in proton-proton collisions at the Large Hadron Collider (LHC) and the precise measurement of their energy is a crucial premise for a manifold of physics studies.

Jets, which are reconstructed exclusively from calorimeter information, have been widely used within the CMS collaboration[3]. However, the response of the calorimeters to incident particles depends heavily on their energy. In addition, it has been observed at previous experiments that the charged particle multiplicity and the radial distribution of constitutents differ for jets induced by light quarks or by gluons. In conjunction with the non-linearity of the CMS calorimeters, this contributes to a mean energy response deviating from unity for calorimeter jets, depending on the jet-flavour.

This thesis describes a jet-energy correction to be applied in addition to the default corrections within the CMS collaboration. This correction aims at decreasing the flavour dependence of the jet-energy response and improving the energy resolution. As many different effects contribute to the observed jet-energy response, a set of observables are introduced and corrections based on these observables are tested with respect to the above aims.

A jet-width variable, which is defined from energy measured in the calorimeter, shows the best performance: A correction based on this observable improves the energy resolution by up to 20% at high transverse momenta in the central detector region and decreases the flavour dependence of the jet-energy response by a factor of two. A parametrisation of the correction is both derived from and validated on simulated data. First results from experimental data, to which the correction has been applied, are presented. The proposed jet-width correction shows a promising level of performance.

---

[3] Compact Muon Solenoid

Contents

Chapter 1.

Introduction

Mankind has always posed questions concerning the where, when, and how of existence. In the strive for knowledge, many different models to explain the world around us have been proposed, tried, and dismissed.

In recent decades, scientists from all over the world have worked together to form a new understanding of fundamental particles and forces: The Standard Model of particle physics. Collimated sprays of particles, the so-called jets, are observed in high-energy particle collisions and can be understood within this model.

These observable signatures of fundamental interactions are also a key for understanding and probing the Standard Model. The following analysis aims at improving the measurement of these observables at the Compact Muon Solenoid (CMS) experiment at CERN, the European Organisation for Nuclear Research.

Jets that are reconstructed from measured energy depositions in the calorimeters, and jets that are reconstructed from simulated particles typically have different energies, for which the non-linear and non-uniform response of the CMS calorimeters is the main reason. The jet-energy calibration performed by CMS relates, on average, these two energies.

In the following, the term jet response refers to the ratio of the measurement of the transverse momentum p_{T} of the jet and the "true" jet-p_{T}, which is mostly determined from simulations. Due to the non-linear response of the CMS calorimeters, there is a dependence of the jet response on the momentum spectrum of the jet constituents and their radial distribution. For these quantities differences are expected between jets induced by light quarks or gluons. As a consequence, the mean response of jets induced by light quarks or gluons differs significantly as is shown in Figure 1.1. Jet-width variables are thought to give a handle on these properties and one of these, the second central moment of the jet profile in transverse momentum $\sigma_{\varphi\varphi}$, has been studied extensively in a previous diploma thesis[1].

In order to decrease the difference observed in Figure 1.1 and to further improve the energy resolution of jets, the correlation of several variables with the jet-energy response from simulations (often referred to as "Monte Carlo") is examined and corrected for. As the following analysis focusses on jets, which are reconstructed from calorimeter

---

[1] Kolodzey, B. "Studie zur Flavour-Abhängigkeit von Jet-Korrekturen zum CMS-Kalorimeter bei LHC" - "Studies on the flavour dependence of jet-energy corrections for the CMS calorimeters", diploma thesis, University of Hamburg, 2010

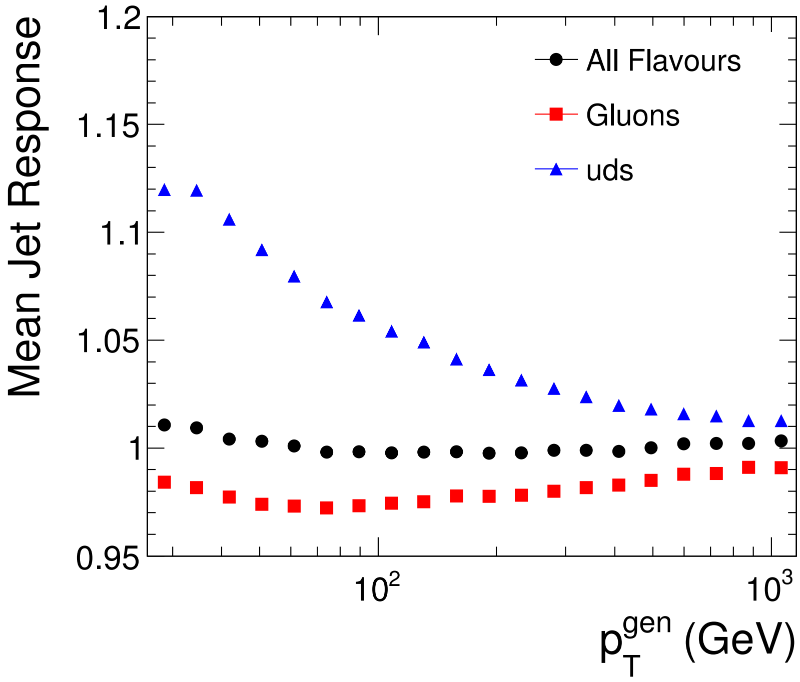

Figure 1.1.: Mean jet response (i.e. ratio of the transverse momentum p_T (see Section 3.3 for the definition of transverse momentum at CMS) of reconstructed calorimeter jets with standard CMS jet-energy corrections and “true“ p_T known from Monte Carlo event generators p_T^{L2L3}/p_T^{gen}) for average QCD flavour jets (mixture as in PYTHIA QCD simulation), gluon, and light quark jets (see Chapter 4 for details on jet reconstruction and jet-energy corrections at CMS)

information, the observables are required to be calculated only from measured energy in the calorimeters.
A full parametrisation of a correction for the best-performing variable is developed and validation tests with simulated data and events from proton-proton collisions, recorded during the 2010 run of the Large Hadron Collider (LHC), are performed. Data from collider experiments will in the following be referred to as ”data“, data from simulations using the Monte Carlo technique will be referred to as ”simulated data“.

The thesis is structured as follows:
Some physics aspects following from the Standard Model of particle physics are summarised in Chapter 2. The concept of jets and their description is discussed, and electromagnetic and hadronic showers, which form the signature of jets in particle physics detectors, are touched upon.
The LHC accelerator complex at CERN provides the CMS experiment with collisions of high-energetic proton and heavy-ion beams. The LHC and the experiments associated with it are described in Chapter 3 and some basic features of the CMS experiment are discussed.

The different approaches to jet reconstruction at CMS are mentioned in Chapter 4 and the current approach to jet-energy corrections is summarised.

A set of candidate variables are introduced in Chapter 5. A study to compare their performance with respect to improving the jet-energy resolution and decreasing the dependence of the mean jet-energy response on the jet-flavour is presented. The best variable with respect to these aspects is selected for further study.

In Chapter 6, the correlation of the mean jet-energy response and the selected variable is examined, using simulated events, and corresponding correction factors are parametrised. Such a correction is applicable in addition to the currently recommended jet-energy corrections within CMS. The correction factors are determined utilising the Kalibri framework, which is developed by the University of Hamburg CMS group for the derivation of jet-energy corrections.

The performance of the parametrised jet-energy correction is studied in Chapter 7 using simulated data. The dependence on the selected variable vanishes and a considerable improvement of the calibration is demonstrated.

The discussion of the proposed correction concludes in Chapter 8 with an evaluation of the performance on data recorded during the 2010 proton-proton run of LHC. A balancing technique is used for dijet events and allows for qualitative results of the performance of the correction applied to data.

In Chapter 9, a summary of the results obtained and an outlook on the perspectives of the proposed correction is given.

Chapter 2.

Theory

This chapter describes some of the basic ideas concerning the Standard Model of particle physics, the concept of jets, and calorimetry.

2.1. The Standard Model of particle physics

During the first decades of the 20th century, a coherent picture of matter was established. The knowledge of electrons, protons, and neutrons allowed to explain the composition of atoms and the periodic table of the chemical elements. However, the existence of more and more new particles was unveiled (e.g. muons 1936, charged pions[1] 1947) and in the 1960s — after the introduction of more powerful particle accelerators — a large number of particles was discovered.

This “zoo“ was simplified by introducing the quark concept [7]. This is now part of the Standard Model of particle physics, a theory developed in the 1960s and 1970s to describe the elementary particles and their interactions. It combines the understanding of the electromagnetic, weak, and strong interactions in the framework of quantum field theories into a coherent picture comprising three generations of matter (fermions, spin 1/2) and the force carriers (bosons, integer spin) as illustrated in Figure 2.1. Interactions between the fermions are described by the exchange of gauge bosons and depend on the coupling constants of the corresponding type of interaction. Such interactions are often illustrated in the form of Feynman diagrams, which are also graphical representations for terms of the perturbative calculation of the interactions. Textbooks discussing various experimental and theoretical aspects of particle physics in general and the Standard Model in particular include [1–4]. Glashow, Salam, and Weinberg were awarded the Nobel Prize in 1979 “for their contributions to the theory of the unified weak and electromagnetic interaction between elementary particles, including, inter alia, the prediction of the weak neutral current“ [8]. The Standard Model has proven extremely successful in the last decades,

---

[1] Pions belong to the group of mesons, which are compound particles consisting of two quarks (one quark and one antiquark to neutralise the colour charge of the quarks). The most familiar mesons are pions(π^+: $u\bar{d}$, π^0: $d\bar{d}/u\bar{u}$ and π^-: $d\bar{u}$) and kaons(K^+: $u\bar{s}$, K^0: $d\bar{s}/s\bar{d}$ and K^-: $s\bar{u}$).
Compound objects of three quarks are called baryons, most notably the proton and the neutron (p: uud; n: udd)

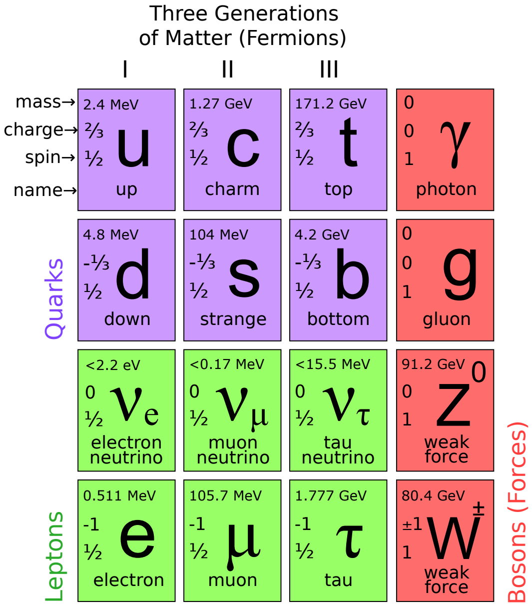

Figure 2.1.: Sketch of the elementary particles as incorporated in the Standard Model of particle physics: Three generations of up- and down-type quarks, three generations of charged and neutral leptons, force carriers of the electromagnetic interaction (photon), the strong interaction (8 gluons), and the weak interaction ($W^{\pm}$ and Z^0); [6]

predicting the existence of elementary particles before their discovery, such as the W and Z bosons, the gluons, and the top and charm quarks.

One building block of the Standard Model is the Higgs particle. This particle has been predicted in the context of the so-called Higgs-mechanism allowing the fermions and the a-priori massless gauge bosons (required to be massless by SU(2) × U(1) gauge symmetry) to acquire mass in the process of electroweak symmetry breaking. It is the only particle of the Standard Model that has not yet been discovered. The mass of the Higgs particle is a free parameter of the Standard Model. At present, the experiments at the Tevatron collider at Fermilab are excluding a Higgs mass range of $158 < m_H < 175\,\text{GeV}$ [9]. In addition, the mass of the Higgs boson is expected to be in the range of $115 < m_H < 158$ GeV as a light Higgs is preferred by global fits of the parameters of the Standard Model to experimental results and lower masses have already been excluded by direct searches at the LEP collider [5].

Even though the Standard Model has proven so successful, it still has some considerable drawbacks and some kind of ”new physics” is expected to emerge at the TeV-scale, probed by the Large Hadron Collider. For example, there is the hierarchy problem, namely the expected mass of the Higgs boson is many orders of magnitude lighter than the Planck mass, i.e. of the order of 10^{19} GeV. Unless there is an extreme fine-tuning between quadratic radiative corrections and the bare Higgs mass, one would expect the mass of the Higgs boson to be much higher. This fine-tuning can be resolved by introducing an additional (and the last possible) symmetry into the Poincaré group called supersymmetry [10]. For all existing particles, partners are postulated that have a different spin (all fermions have bosonic partners and vice versa). Some supersymmetric extensions also supply dark matter candidates. In addition to the complications when trying to explain cosmological observations [11, 12], it should also be noted that the Standard Model does not attempt to incorporate the gravitational force. Results obtained at the LHC will probe many proposed extensions of the Standard Model by examining phase space regions unaccessible at previous collider experiments.

2.2. Jets

High-energy phenomena in Quantum Chromodynamics (QCD)[2] [13, 14] are discussed in terms of quarks and gluons. However, due to confinement objects with a net colour charge can not exist freely. The produced quarks or gluons thus are not observed in nature. Instead, the process of hadronisation leads to a collimated spray of colour neutral hadrons which is referred to as a jet. However, the definition of jets and their connection to the initial partons is conceptually difficult and has been a matter of study for over 30 years [15]. Even though the production of jets is in principle described by QCD, our current understanding is based on a factorised description (including phenomenological models) in the framework of Monte Carlo generators [16]. This factorised approach is illustrated in Figure 2.2:

1. Two protons cross each other and two of their constituents (quarks and gluons) interact with each other. The probability that determines which of the constituents interact, is governed by the parton distribution functions $f(x, Q^2)$, which depend on the momentum fraction x of the interacting parton and the momentum transfer Q^2 in the interaction.
2. The interaction of the two resolved partons is described by matrix element calculation.
3. Parton showering refers to the branching of single partons into two partons. For a branching of initial partons one speaks of initial state radiation (ISR), for a branching of final state partons, the term final state radiation (FSR) has been established.
4. Due to colour confinement, only colour neutral objects are observed in nature. This leads to the hadronisation of the partons originating from the parton shower.
5. Most of the heavier hadrons have a short life time and decay quickly so that jets observed in particle physics detectors consist of relatively few particle types.
6. After the hard scattering of two of the partons, the proton remnants are not colour neutral and will thus hadronise themselves.

These steps will be discussed in more detail in the following paragraphs.

---

[2] QCD, the theory of strong interactions

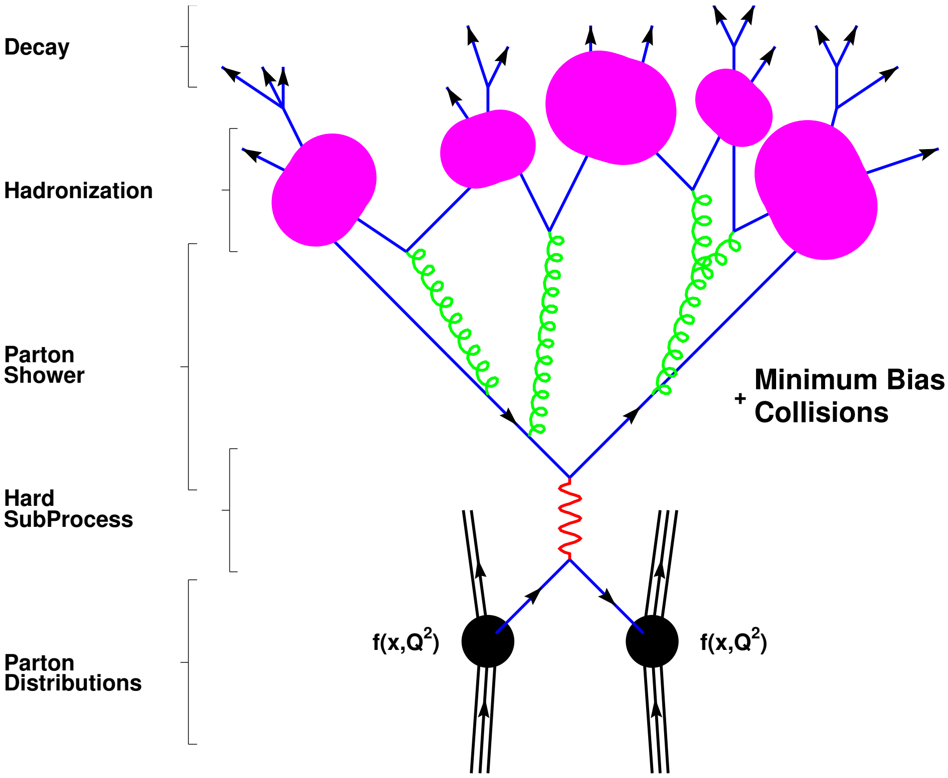

Figure 2.2.: Schematic illustration of the basic structure of event generation for hadron collisions; see [16]

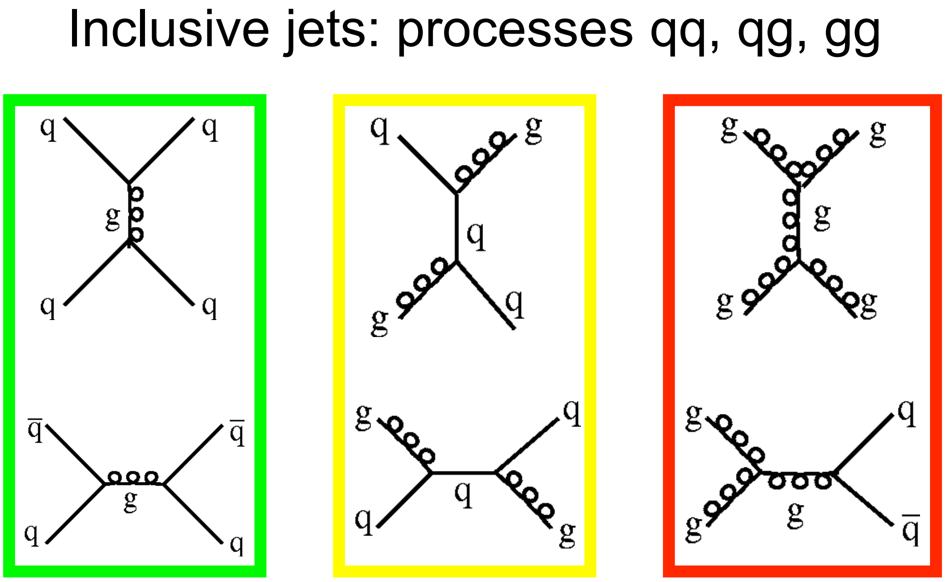

Figure 2.3.: Leading order Feynman diagrams for dijet production at hadron colliders; see [17]

2.2.1. Parton distribution functions and hard scattering

At the LHC, jets are produced in proton-proton collisions. Protons are compound objects and in fact their constituents (valence quarks, sea quarks, and gluons) interact when jets are formed. The factorisation theorem of QCD [18] allows to disentangle high-Q^2 (perturbative) and low-Q^2 (absorbed in parton distribution functions) processes and calculate the cross sections as (see [19])

$$\sigma_{ij \to kl} = \sum_{i,j} \int dx_1 dx_2 f_i^1(x_1, Q^2) f_j^2(x_2, Q^2) \hat{\sigma}_{ij \to kl} \tag{2.1}$$

with the longitudinal momentum fraction of the interacting partons $x_{1/2}$, the momentum transfer Q^2, the perturbative QCD cross section $\hat{\sigma}_{ij \to kl}$ for the process $ij \to kl$, and the parton distribution functions $f_i^{1/2}(x, Q^2)$ for colliding beams 1 and 2.

The parton distribution functions are defined as the probability density for finding a parton with a specified x at a certain Q^2. They can not be calculated by perturbative QCD and are instead obtained using experimental data. For example, the results from deep inelastic scattering (DIS) at HERA play an important role in determining these, due to the large phase space in Q^2 and x. Most of the collaborations compiling sets of PDFs, such as CTEQ and MRST, use experimental data from various collider experiments and different processes to constrain the PDFs in global fits. One of the parametrisations is depicted in Figure 2.5 for two different scale parameters μ^2 (Q^2). For high-momentum-transfer reactions, the parton distribution functions are dominated by gluons leading to the fact that many physics processes observed at the LHC are gluon-dominated, such as the production of top quarks.

The partonic cross sections for the hard scatter $\hat{\sigma}_{ij \to kl}$ can be determined by calculations in perturbative QCD for high-Q^2 as the strong coupling constant becomes sufficiently small. The running of the coupling can be approximated in lowest order by

$$\alpha_s(Q^2) = \frac{4\pi}{(11 - \frac{2}{3}n_f) ln(\frac{Q^2}{\Lambda^2})} \tag{2.2}$$

where n_f denotes the number of quark flavours (at a specific Q^2) and Λ is the experimentally determined scale parameter of QCD (see Figure 2.4 for a sketch of α_s at different values of Q^2). The "running“ of the strong coupling constant is also interesting with respect to confinement: Where perturbative corrections break down (low Q^2), the confinement of quarks in hadrons is observed. Feynman diagrams of lowest order relevant for the production of dijets are depicted in Figure 2.3. General purpose Monte Carlo generators such as PYTHIA [20] or HERWIG [21] have the analytical formulae for a large number of physics processes implemented. For the general purpose event generators the implementation is often limited to lowest order calculations, but they can be interfaced with specialised matrix element generators [16] such as ALPGEN [22] or MadGraph [23] that include Next-to-Leading Order (NLO) or even higher-order perturbative calculations.

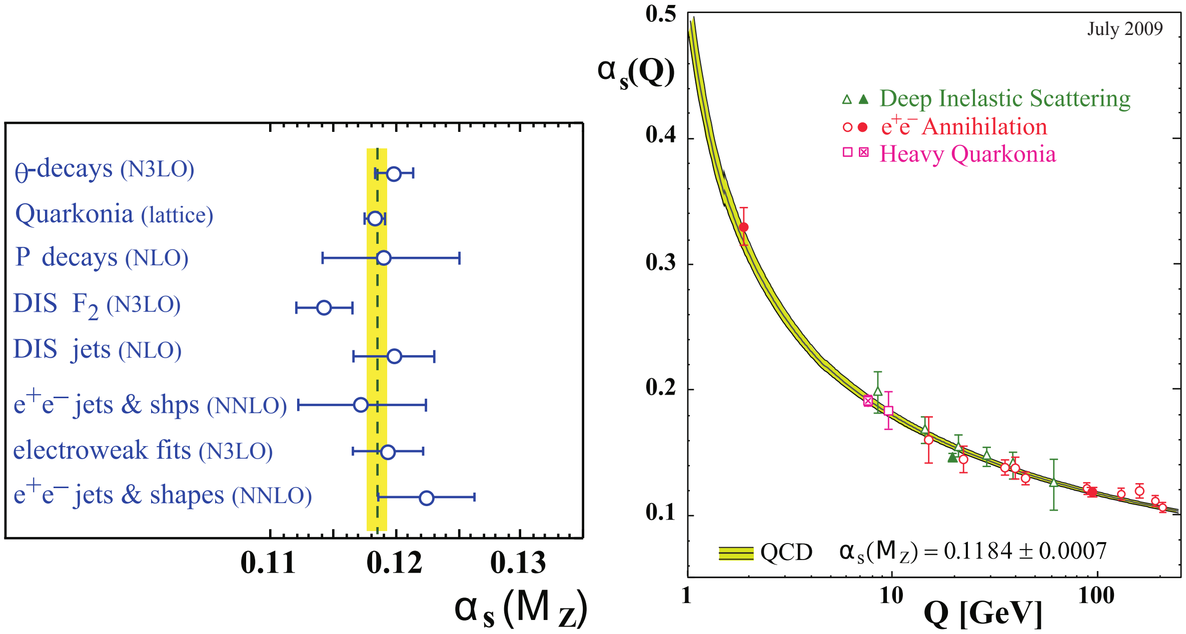

Figure 2.4.: Sketch of the structure constant of the strong interaction as a function of Q (right) and (left) several measurements of the constant forming the world average at the mass of the Z-boson; [5]

2.2.2. Parton showering and fragmentation/hadronisation

Once the hard scattering producing outgoing partons has taken place, a perturbative evolution gives rise to a shower of quarks and gluons. This can in principle be calculated as a systematic expansion in α_s, but as the needed calculations in higher orders are very time-consuming and not widely available, current event generators perform a more generic approach called parton showering to circumvent the problem of the missing higher-order calculations. Initial state and final state radiation is superimposed on the underlying hard scattering by using a leading $\log(Q^2)$-approximation. The radiation of gluons from quarks and the splitting of gluons into $q\bar{q}$-pairs is approximated using the DGLAP-equations [24] which give the probability for a parton to branch.

A mother parton a is considered to branch into two daughter partons b and c. The measure z determines the sharing of momenta between b and c. Daughter b takes the fraction z of the initial momentum of a, daughter c takes (1-z) of the initial momentum. For a convenient description, the scale-dependent parameter t can be defined:

$$t = \ln(Q^2/\Lambda^2_{QCD}) \Rightarrow dt = \frac{dQ^2}{Q^2} \tag{2.3}$$

The differential probability dP_a for a parton a to branch is given as

$$dP_a = \sum_{b,c} \frac{\alpha_{abc}}{2\pi} P_{a\to bc}(z) dt dz \tag{2.4}$$

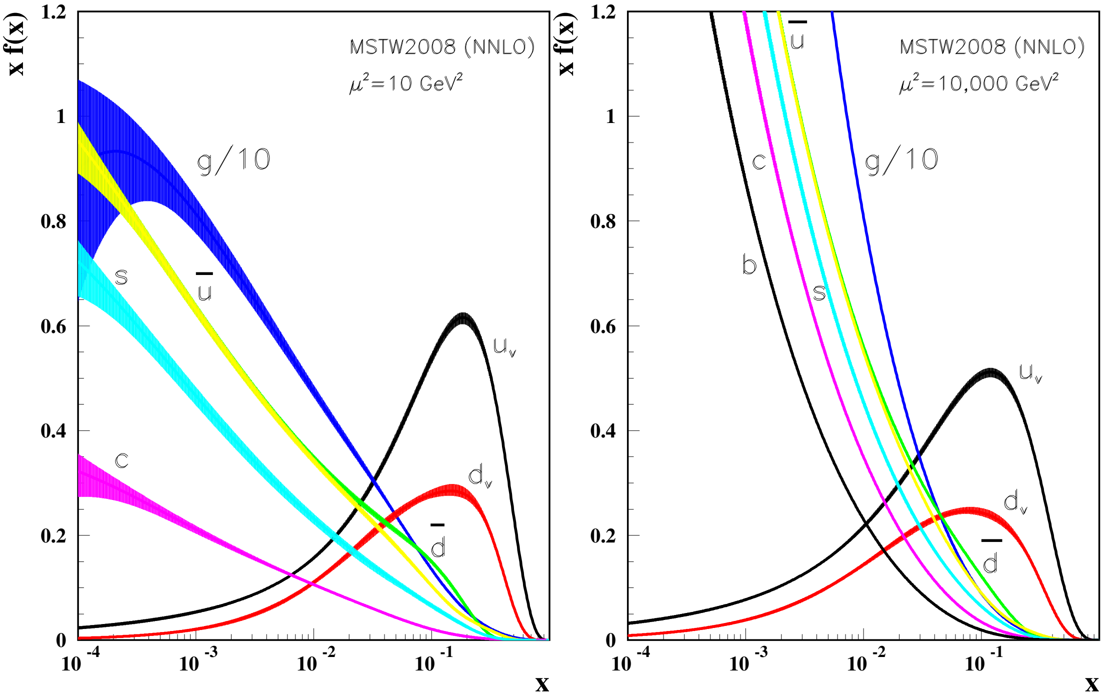

Figure 2.5.: Distributions of x multiplied by the unpolarised parton distributions $f(x)$ (where $f = u_v, d_v, u, d, s, c, b, g$ and their associated uncertainties using the NNLO MSTW2008 parameterisation at a scale $\mu^2 = 10\,\mathrm{GeV}^2$ and $\mu^2 = 10000\,\mathrm{GeV}^2$); [5]

Where the sum runs over all allowed branchings (allowing the radiation of photons as well) and the factor α_{abc} corresponds to α_s or α_{QED} depending on the splitting. The splitting kernels $P_{a\to bc}(z)$ for the corresponding branchings are given as

$$
\begin{aligned}
P_{q\to qg}(z) &= C_F \frac{1+z^2}{1-z} \\
P_{g\to gg}(z) &= N_C \frac{(1-z(1-z))^2}{z(1-z)} \\
P_{g\to q\bar{q}}(z) &= \frac{n_f}{2}(z^2 + (1-z)^2) \\
P_{q\to q\gamma}(z) &= e_q^2 \frac{1+z^2}{1-z} \\
P_{l\to l\gamma}(z) &= e_l^2 \frac{1+z^2}{1-z}
\end{aligned}
$$

where $C_F = 4/3$ is the colour factor, $N_C = 3$ is the number of colours, n_f corresponds to the number of quark flavours, and $e_{l/q}$ corresponds to the electric charge of the lepton/quark in units of the elementary charge e. This branching can occur iteratively, leading to softer and softer splittings. As the description becomes invalid for too-

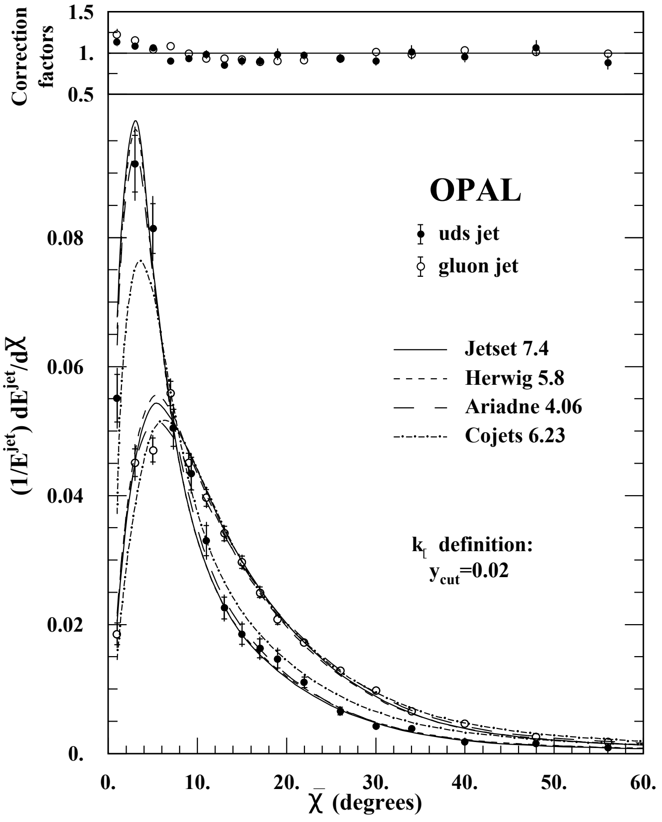

Figure 2.6: The normalised distribution of jet energy with respect to the jet axis for uds and gluon jets as observed by the OPAL collaboration with k_t-jets and in comparison to the prediction by various MC event generators; errors include statistical and systematic terms (statistical uncertainties correspond to the small horizontal bars). See [26]

soft splittings (α_s approaching 1), a lower cutoff-scale is introduced at the order of $Q^2 = 1\,\mathrm{GeV}^2$, and the branching probabilities are weighted with the Sudakov form factor in order to avoid unphysical behaviour (if a parton has already branched at $t' < t$ it can no longer branch at t). More details on the parton showering are available in [20, 25].

In order to perform the transition from few-parton to many-hadron states (particle jets) the various available event generators use different fragmentation models. These models had to be developed as the perturbation theory breaks down for large distances, when α_s diverges (see Figure 2.4).

For the fragmentation process, two different approaches are widely used in Monte Carlo event generators. For example, the string fragmentation model is used by PYTHIA and the cluster fragmentation method is used by HERWIG. [5]

The string fragmentation model considers the colour field between the partons to be the cause of fragmentation. This string can be interpreted as a colour flux tube that is formed by self-interacting gluons when two coloured partons fly apart. While the two partons are moving apart it becomes energetically favoured for the string to break up by producing additional $q\bar{q}$-pairs. This is due to the assumed potential that increases linearly with the distance (neglecting a short-distance Coulomb term). The pairs are produced according to the tunnelling probability $\exp(-\pi m^2_{q,\perp}/\kappa)$, which depends on the transverse mass squared $m^2_{q,\perp} \equiv m^2_q + p^2_{q,\perp}$ and the string tension $\kappa \approx 1\,\mathrm{GeV/fm}$. The behaviour is governed by the string-fragmentation function $f(z)$ with two empirical parameters that are adjusted to agree with data. This model suppresses the production of heavy quarks (mass in tunnelling probability) and is therefore adapted to be in agreement with

experimental observations.
The cluster fragmentation as adapted by HERWIG takes the remaining gluons at the end of the parton shower evolution and splits them non-perturbatively into quark-antiquark pairs, assuming a local compensation of colour. Clusters of quarks and antiquarks with a typical mass of a couple of GeV are formed and then decay directly into two hadrons (or to a single hadron, when they are too light, or into two clusters when they are too heavy). The cluster fragmentation has a very compact description with a few parameters.
It has been experimentally verified that the fragmentation differs for gluon and light quark induced jets. For example, OPAL has published a comparison of uds quark jets to gluon jets in 1996 [26], in which the ratio of the mean charged particle multiplicities of gluon and light quark jets was found to be

$$\frac{\langle n^{ch} \rangle_{gluon}}{\langle n^{ch} \rangle_{uds}} = 1.390 \pm 0.038(stat.) \pm 0.032(syst.) \tag{2.5}$$

This was a hint on a softer particle spectrum of gluon jets and indeed the gluon jets have been found to be broader (see Figure 2.6, where the normalised distribution of jet energy as a function of the angle with respect to the jet axis is shown). Other studies on differences between gluon and light quark jets include [26–29].

2.2.3. Decay of unstable particles

A significant fraction of the hadrons produced in the hadronisation process are unstable. Their lifetimes are usually well known and their decays are simulated accordingly (in PYTHIA all particles with $c\tau < 10$mm are allowed to decay). For example the decay of π^0(usually into two photons) is already handled by PYTHIA.

2.2.4. Underlying event

Considering Figure 2.2, the different steps for the description of jet events have been discussed. However, the proton remnants also carry a net colour charge, when constituents are hard-interacting and thus removed from the initial proton. These remnants hadronise and contribute to the underlying event. Multiple parton interactions (MPI) also contribute to the underlying event - these are additional "semi-hard" scatterings between partons other than the partons involved in the initial hard scattering.

2.2.5. Description of experimental data

For the jet production at existing experiments (pre-LHC), a good agreement between simulations and data is observed over a wide phase space [30]. This is illustrated in Figure 2.7, where data-over-theory ratios for the inclusive jet production are depicted as a function of transverse momentum of the jet. It still remains a matter of study how well the description will be at LHC-energies. In Figure 2.8, the cross sections are compared for the centre-of-mass energies of the Tevatron and the LHC [31]. The reach for jets with a high transverse energy is significantly extended due to the higher centre-of-mass energy. Jets of unprecedented transverse momenta have already been observed at LHC and the study of jets promises new insights not only in itself, but also provides a foundation for a wide area of sophisticated analyses of physics scenarios within the Standard Model and beyond.

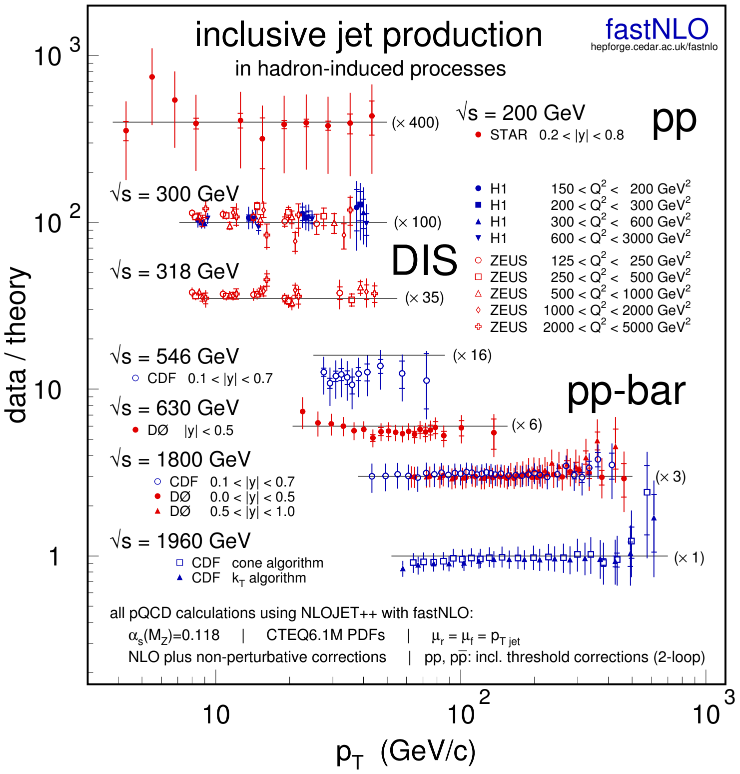

Figure 2.7.: Ratios of experimental data and theory predictions for inclusive jet cross sections as a function of the transverse momentum of the jet. The different ratios are scaled by arbitrary factors as indicated in parentheses. Theoretical predictions at Next-to-Leading Order accuracy with parameters as given at the bottom of the plot; [5]

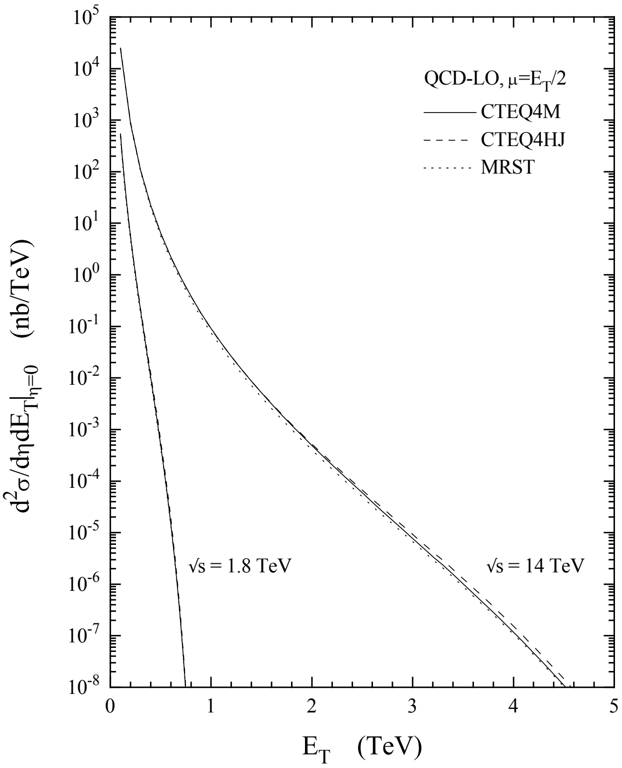

Figure 2.8: Inclusive jet cross section vs. jet transverse energy at the LHC compared with the Tevatron. Figure taken from [31]

2.3. Calorimetry

Calorimeters are used in particle physics to measure the energy and position of incident particles or jets by total absorption of these particles. During the process of absorption, showers are generated by cascades of interactions. The energy loss of the shower particles leads to a signal (e.g. light) that is received, amplified, and related to the incident particle's energy. Two different kinds of showers are observed, namely electromagnetic showers initiated by electrons or photons, and hadronic showers initiated by incident hadrons. Electromagnetic and hadronic showers differ in their topology and physics processes and it is beneficial for the determination of the jet energy to separate the two components. A detailed discussion of calorimetry in high energy physics is given in [32]. Briefer summaries are given in references [33–37].

2.3.1. Electromagnetic showers

When interacting with matter, the production of e^+e^--pairs is the dominant process for high-energy photons and bremsstrahlung is the primary energy loss mechanism for high-energy electrons. The cross section of these reactions becomes almost independent of energy above particle momenta of 1 GeV (see Figure 2.10). The characteristic scale of electromagnetic showers and for the processes taking place at high energies is the radiation length X_0. It corresponds to the mean distance it takes a high-energy electron to loose all but $1/e$ of its energy by bremsstrahlung and is equal to 7/9 of the mean free path for e^+e^--pair production by high-energy photons.
An approximation of the radiation length is given in [5]:

$$X_0 = \frac{A \cdot 716.4\,\mathrm{g \cdot cm^{-2}}}{Z(Z+1)\ln(287/\sqrt{Z})}, \tag{2.6}$$

where Z is the atomic number and A is the atomic weight of the traversed material.
The fractional energy loss per radiation length as a function of electron or positron energy is depicted in Figure 2.10(a), the photon cross sections as a function of the photon energy are given in Figure 2.10(b). A cascade as depicted in Figure 2.9 develops through repeated interactions of electrons and photons by the above mentioned mechanisms, leading to more and more electrons and photons. The shower maximum is at the point where the average energy of the shower particles falls below the point, where the rate of ionisation and bremsstrahlung energy losses is equal. This threshold is denoted the critical energy and can be approximated as

$$E_c = (800\,\mathrm{MeV})/(Z + 1.2) \tag{2.7}$$

where Z is the atomic number. Below this critical energy, ionisation becomes the dominant energy loss mechanism for electrons and positrons. Photons primarily interact via the photoelectric effect at low energies and via Compton scattering at intermediate

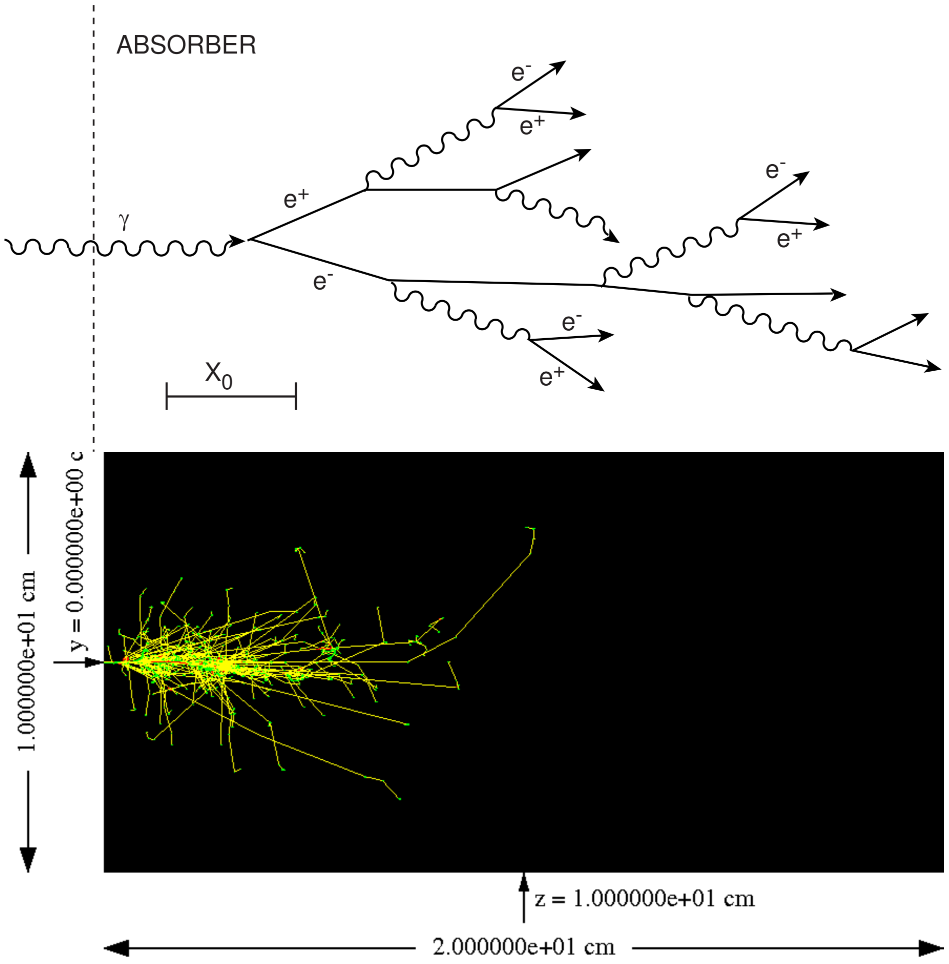

Figure 2.9.: Upper plot: Sketch of the beginning of an electromagnetic shower, see [38]
Lower plot: Simulation of 1 incident electron (1 GeV) on a tungsten absorber, generated using the web interface in [39]

energies, before pair production becomes dominant at higher energies (see Figure 2.10(b)).

An approximation of the mean longitudinal profile of an electromagnetic shower is given in [33] as

$$\frac{dE}{d(x/X_0)} = E_0 b \frac{(b(x/X_0))^{a-1} e^{-b(x/X_0)}}{\Gamma(a)} \tag{2.8}$$

with $b \approx 0.5$ and a determined from the maximal energy deposition at

$$(x/X_0)_{max} = (a-1)/b = 1.0(\ln(E/E_c) + C_j) \tag{2.9}$$

with $C_j = -0.5$ for cascades induced by electrons and $C_j = 0.5$ for photon-induced showers. The longitudinal energy deposition of electromagnetic showers is very regular and the transverse shower development scales with the "Molière radius" R_M. On average,

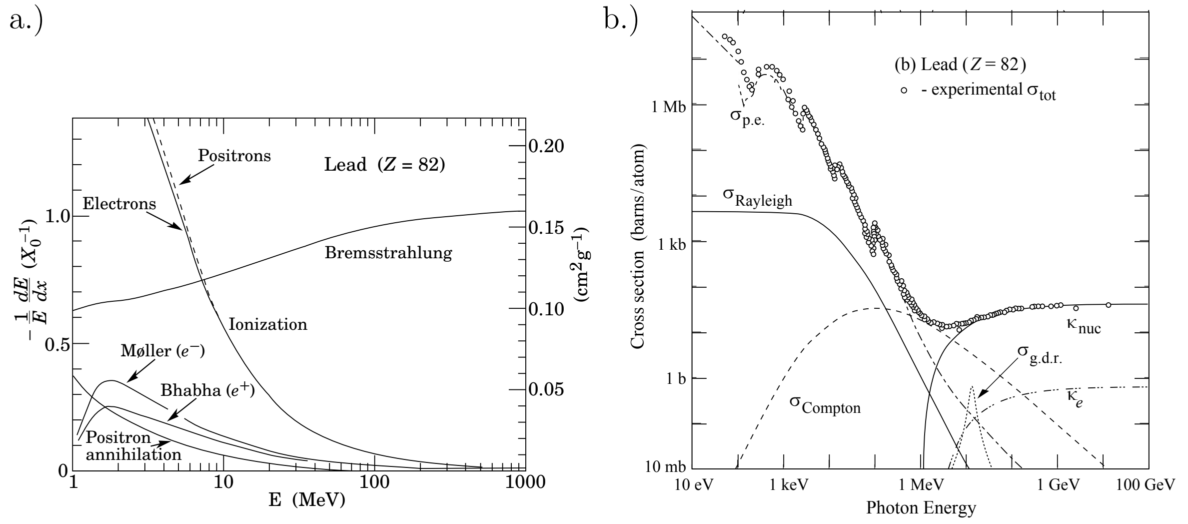

Figure 2.10.: a.) Fractional energy loss per radiation length in lead as a function of electron or positron energy; [33]
b.) Photon cross sections as a function of photon energy in lead (contribution by pair production in the nuclear and electron field: κ_{nuc} and κ_{nuc}); [33]

only 10 % of the energy is deposited outside of a cylinder of radius R_M and approximately 99 % is contained in a cylinder with $R = 3.5R_M$. The characteristic radius is approximated as

$$R_M = X_0 E_s/E_c \,\text{with}\, E_s \approx 21\,\text{MeV} \tag{2.10}$$

Electromagnetic calorimeters: Electromagnetic calorimeters are used to measure the energy of incident electrons and photons. In order to discriminate electromagnetic showers from hadronic showers, the absorption material is chosen to maximise the ratio of the interaction length λ_{int} (see section on hadronic showers) and the radiation length λ_{int}/X_0 which is approximately proportional to $Z^{1.3}$ according to [40]. This leads to the choice of material with a high Z (e.g. lead tungsten crystals in the electromagnetic calorimeter of CMS). The electromagnetic calorimeter is built sufficiently thick in X_0 in order to contain the full electromagnetic shower. A signal proportional to the amount of deposited energy is measured in some active material. Even though the shape and length of showers is mainly determined by high-energy processes, most of the energy is deposited by very soft shower particles. The active material for readout can either be identical with the absorption material, such as in homogeneous crystal calorimeters, or can be some other material as is the case in sampling calorimeters.

The creation of an electromagnetic shower is a statistical process with inevitable fluctuations regarding the particle multiplicity and signal creation. Provided that these fluctuations follow Poisson statistics, the standard deviation is $\sigma = \sqrt{N}$. Assuming

$N \propto E$ one can define the stochastic term of the energy resolution:

$$\frac{\sigma(E)}{E} \propto \frac{1}{\sqrt{E}} \tag{2.11}$$

This is the dominant contribution to the energy resolution over a wide range of the particle energies examined with calorimeters. Sampling fluctuations inherent to sampling calorimeters increase this contribution leading to a potentially poorer performance in comparison to homogeneous calorimeters.

In reality, other effects contribute to the energy resolution as well: Relatively energy-independent instrumental effects such as noise, whose relative contribution decreases with

$$\frac{\sigma(E)}{E}_{Noise} \propto \frac{1}{E} \tag{2.12}$$

and a constant term limiting the performance of calorimeters at high energies. Contributions to this constant uncertainty are due to instrumental effects such as non-uniformities and non-linearities of detector components for signal detection (e.g. photomultipliers).

2.3.2. Hadronic showers

When the incident shower particles are hadrons, the showers that develop are much more irregular and less well understood than electromagnetic showers. The strong interaction as described by QCD is responsible for the additional reactions taking place. In the upper plot of Figure 2.11 some features of hadronic showers are schematically illustrated. On the one hand inelastic hadronic interactions lead to the production of hadronic shower particles of which $\approx 90\%$ are pions. On the other hand nuclear reactions take place in the atomic nuclei. Neutrons, protons, and heavy fragments can be released.

The characteristic length of hadronic showers is the nuclear interaction length λ_{int}. It is determined by the inelastic cross section for a hadronic interaction σ_{inel} as well as the atomic weight A and the density of the traversed absorption material ρ:

$$\lambda_{int} = \frac{A}{\sigma_{inel} N_A \rho}, \tag{2.13}$$

where N_A is the Avogadro constant. In comparison to the radiation length X_0, the interaction length is much larger for high-Z materials (up to a factor of 30, see also Figure 3.6 for the example of the CMS configuration). It corresponds to the average distance hadrons travel before they undergo a nuclear interaction.

A simple parameterisation of the average shower shape as given in [35] yields

$$l_{max} \approx [0.6 \log(E) - 0.2] \lambda_{int} \tag{2.14}$$

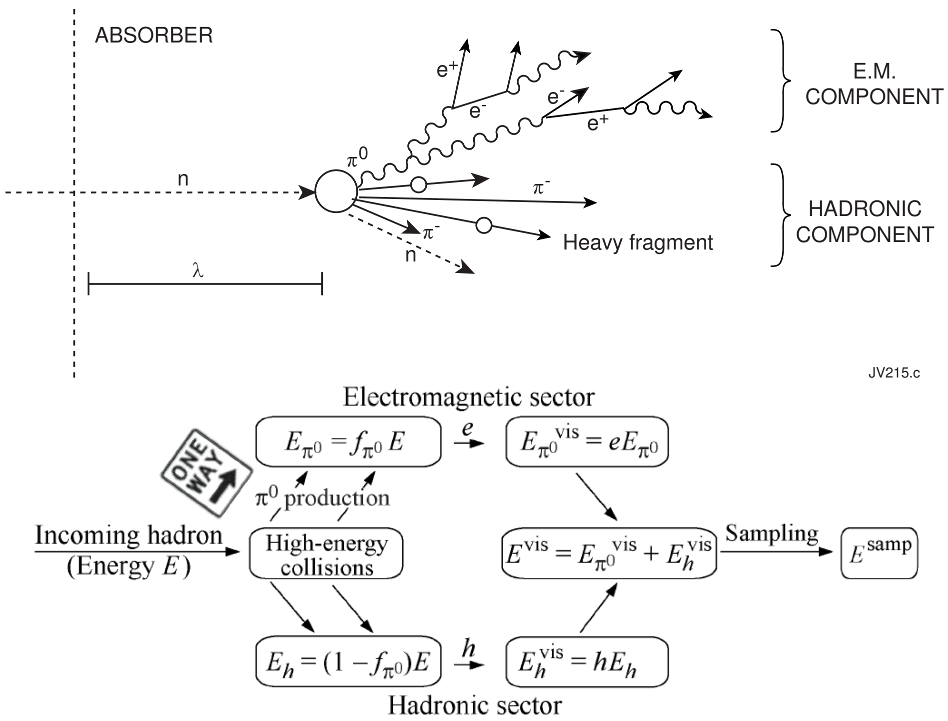

Figure 2.11.: Upper plot: sketch of the initiation of a hadronic shower - an incident high-energy hadron interacts strongly producing a hadronic component (mainly charged pions) and π^0s migrating energy into electromagnetic showers; [38]
Lower plot: Energy flow in a hadronic cascade. A fraction f_{π^0} (with the mean of f_{π^0} increasing in energy) of the total energy is transferred into electromagnetic showers. This is due to repeated inelastic hadronic collisions leading to π^0-production (i.e. photons); [37]

for the shower maximum and

$$l_{95\%} \approx l_{max} + 4E^a \lambda_{int} \tag{2.15}$$

as the depth for 95% containment of the shower with E in GeV and $a = 0.15$. However, this has to be seen in the context that the shape of individual hadronic showers is much more irregular than that of average electromagnetic showers. Only when the average distribution of a large number of hadronic showers is compared to the average distribution of electromagnetic showers they look very similar. Four examples of the energy depositions in a sampling calorimeter induced by hadronic showers are depicted in Figure 2.12.

The shape depends strongly on the fluctuating π^0-component as π^0s themselves initiate electromagnetic showers. The relative energy fraction of this electromagnetic component inherent to the hadronic showers increases with energy as neutral pions can be produced in each of the subsequent inelastic hadronic reactions.

The shape also depends on the relative fraction of energy in the hadronic component that is not visible to the detector. A major part of this invisible component is made up of the nuclear binding energy that has to be overcome to release fragments from

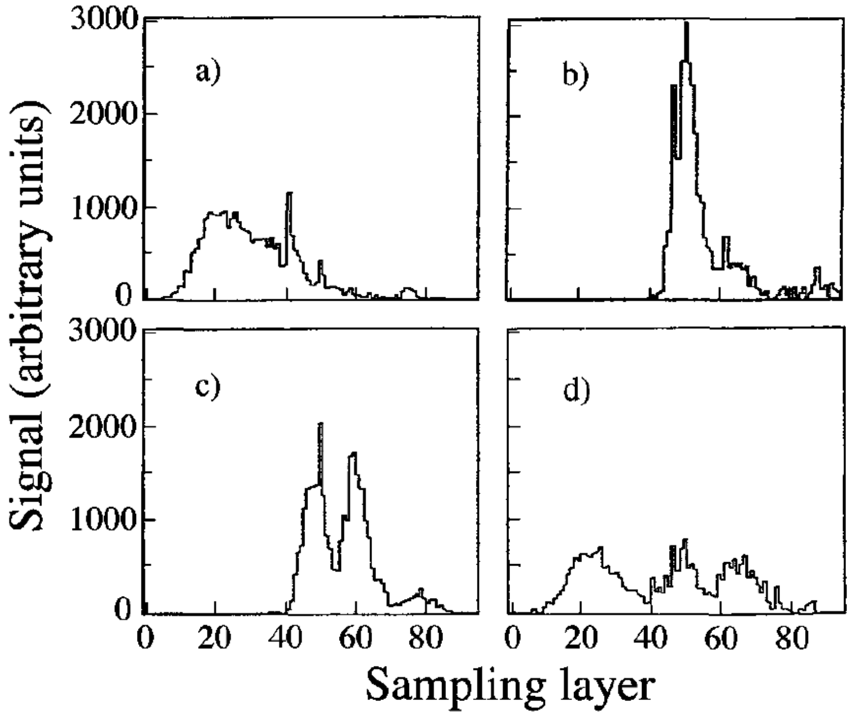

Figure 2.12.: Longitudinal profile of four different showers in a sampling calorimeter that were induced by 270 GeV pions; [36]

atomic nuclei. A minor contribution is due to the escape of particles such as muons and neutrinos. These particles can leave the calorimeter undetected (neutrinos) or with only a small energy loss due to ionisation (muons, mostly minimal-ionising-particles (MIPs)).

Hadronic calorimeters: The wide variety of physics processes and interplay between the electromagnetic and hadronic sector of the shower results in an increased uncertainty in the measurement of the energy of incident particles. In the lower plot of Figure 2.11, the energy flow into these two sectors is depicted.
The energy of the incident particle is split up into an electromagnetic fraction f_{π^0} and the hadronic cascade with an energy fraction of $(1 - f_{\pi^0})$. On average, a certain fraction of the energy is diverted from the hadronic sector in each inelastic hadronic interaction by π^0-production (indeed the fraction is below 1/3 which would correspond to an equal distribution on π^-, π^+, and π^0) and the number of these interactions increases with the energy of the incoming hadron. This leads to an increase of f_{π^0} with energy and would asymptotically result in almost exclusively electromagnetic showers for infinite energies. In reality, the fraction of this electromagnetic component increases from $\approx 30\%$ at 10 GeV to $\approx 50\%$ at 100 GeV [36].
Due to the invisible energy linked to the reactions in the hadronic sector, the calorimeter response for the hadronic sector is in general smaller than that for the electromagnetic sector, if no additional measures are taken. This is reflected in the factors e and h in the energy flow sketch, where each factor stands for the response for the electromagnetic

fraction (e) and the hadronic fraction (h). If $e \neq h$, one speaks of a non-compensating calorimeter, typical values for the ratio are between 1.5 and 2.0. Active compensation for the invisible energy can be achieved by amplifying the signal from neutrons through various techniques. An example of a compensating calorimeter is the Uranium calorimeter deployed in the ZEUS experiment [32].

Experimentally, the e/h-ratio is not directly accessible. Instead, the response of electrons and pions can be measured in test beams which allow to determine the e/π response-ratio and is related to e/h as

$$\frac{e}{\pi} = \frac{(e/h)}{1 - f_{\pi^0}(1 - e/h)} \tag{2.16}$$

For a non-compensating calorimeter, the energy dependent f_{π^0} leads to a non-linear response to incident hadrons.

In comparison to electromagnetic calorimeters, existing hadronic calorimeters have a worse energy resolution due to the additional complications discussed above. Different approaches are evaluated for future calorimeters such as calorimeters with a very fine granularity [41] or calorimeters with a dual readout to determine the electromagnetic fraction f_{π^0} on an event-by-event basis [42] in order to improve the energy measurement of hadronic showers.

Chapter 3.

LHC and the LHC experiments

3.1. The LHC accelerator

The Large Hadron Collider (LHC) is a particle accelerator at CERN, the European Organisation for Nuclear Research [43, 44]. The design centre-of-mass energy of 14 TeV achieved via the collision of two 7 TeV proton beams provides a significant increase in comparison to all previously built storage rings as depicted in Figure 3.1.

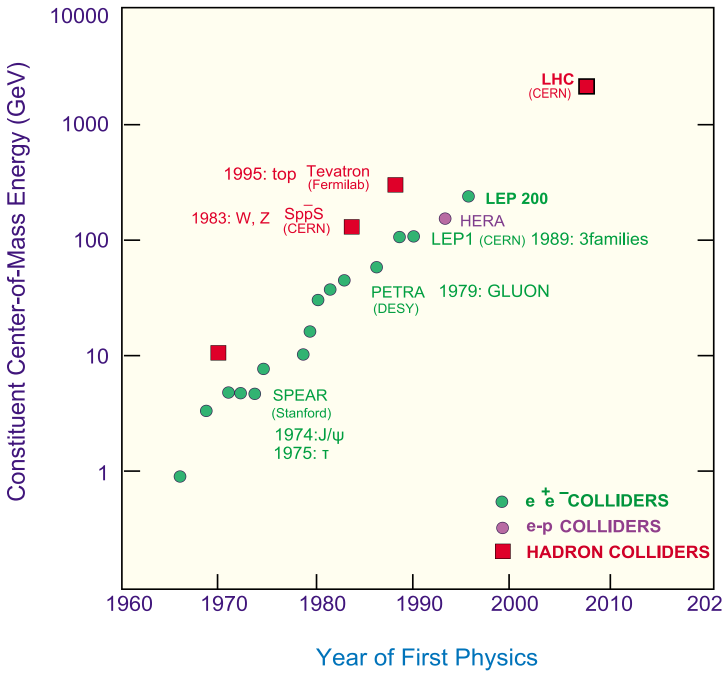

Figure 3.1.: The Livingston-Plot shows the history in the development of particle accelerators. Figure taken from [45], updated with respect to year of first LHC physics.

The Tevatron at the Fermilab[1] can be seen as the predecessor of the LHC as a hadron collider. Beams of protons and antiprotons are accelerated to 980 GeV each and are

---

[1] The term "Fermilab" refers to the Fermi National Accelerator Laboratory in Batavia, Illinois

Key parameters of the LHC	
Circumference	26.659 km
Centre-of-mass energy(protons)	14 TeV
Centre-of-mass energy(ions)	1150 TeV
Peak luminosity	$10^{34}\mathrm{cm}^{-2}\mathrm{s}^{-1}$
Number of filled bunches	2808
Number of particles per bunch	$1.5 \cdot 10^{11}$
Average bunch length (collision)	7.6 cm
Stored energy per beam(collision)	362 MJ
RMS beam size at CMS interaction point	16.7 μm
Collision rate	40 MHz

Table 3.1.: LHC key parameters with design values taken from the LHC TDR Volume 1, compare [43]

brought to collision inside the CDF and DØ detectors with a centre-of-mass energy of about 1.96 TeV. In 1995, the top quark, the last undiscovered quark predicted by the Standard Model, was discovered there [46, 47]. The LHC surpasses the possibilities for research previously carried out at the Tevatron once enough data is recorded.

The LHC complex utilises the tunnel and various other facilities previously used by LEP, the Large Electron-Positron collider. LEP operated from 1989 until 2000, supplying four general purpose detectors (Aleph, Delphi, Opal, and L3) with e^+e^--collisions. Several important results have been obtained during the runtime: The masses of the W- and Z-bosons were determined with great precision and the number of light neutrinos was constrained to three [48, 49]. After the operation of LEP was shut down, the construction of the LHC began.

The storage ring of the Large Hadron collider measures slightly less than 27 kilometres in circumference (see Figure 3.2 for an overview) and is situated between 50 and 150 m below ground, crossing the Swiss/French border twice near Geneva. For some key parameters of the accelerator components see table 3.1. 1232 superconducting dipole magnets and 392 superconducting quadrupole magnets are installed to guide and focus the two proton beams.

At design luminosity, 2808 of the 3564 possible bunches in the storage ring are filled [43, 44]. Before the proton beams are injected into the LHC, they are preaccelerated in the Linac 2, PSB, PS and SPS (see Figure 3.2 for details).

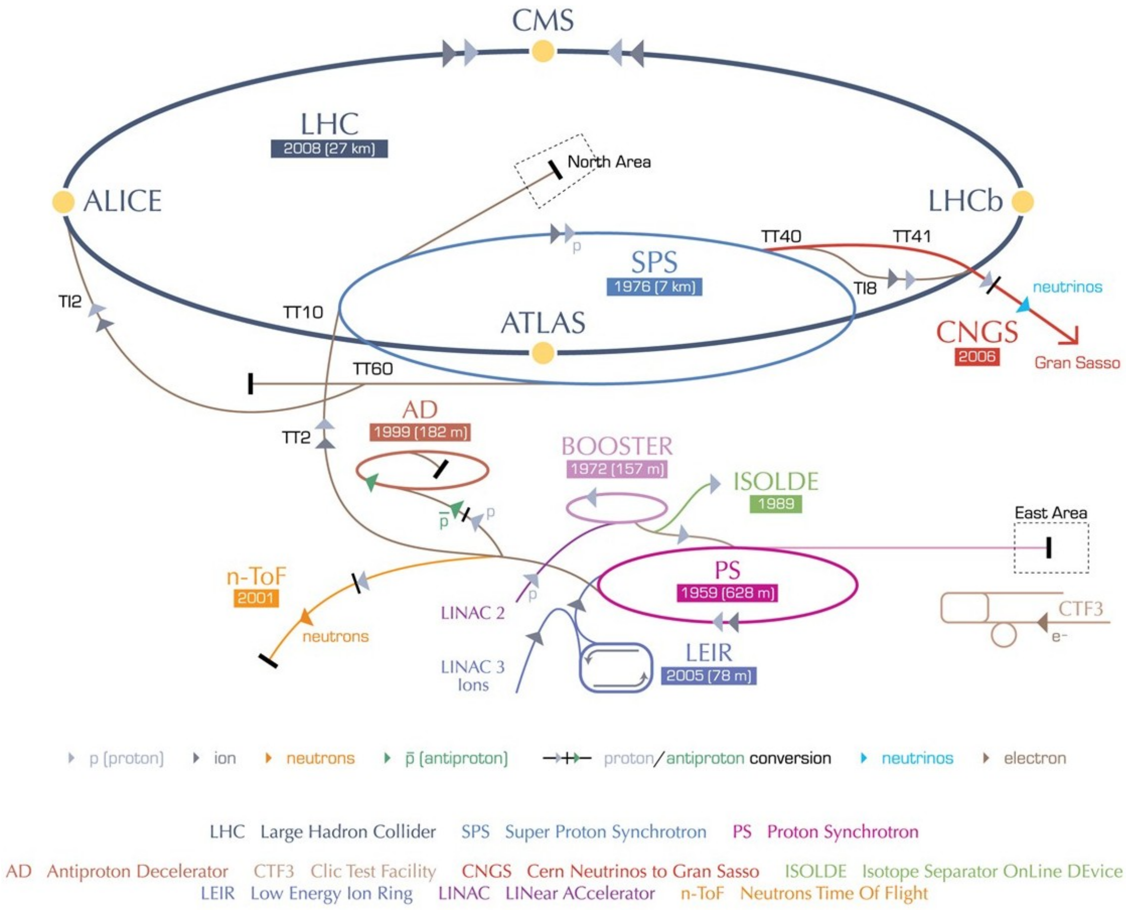

Figure 3.2.: The LHC with experiments and its preaccelerators: Proton beams originate from the linear accelerator Linac 2 (50MeV) and are subsequently accelerated to 1.4 GeV (Proton Synchrotron Booster - PSB), 26 GeV (Proton Synchrotron - PS) and 450 GeV (Super Proton Synchrotron - SPS) before being injected into the LHC, where they are further accelerated to up to 7 TeV. Figure taken from [50]

3.2. Experiments at the LHC

Several detectors have been planned for the physics programme of the LHC. CMS (Compact Muon Solenoid) and ATLAS (A Toroidal LHC ApparatuS, [51]) are general purpose detectors. They are constructed in such a way that the range of physics studies that can be performed using their data is maximised. CMS will be discussed in detail in the following sections. ALICE (A Large Ion Collider Experiment, [52]) is specifically designed to investigate the results of the collision of heavy ions; i.e. lead ions with a centre-of-mass energy of 5.5 TeV per nucleon – equivalent to 1150 TeV total ($m_{Pb} = 207$u). LHCb (Large Hadron Collider beauty, [53]) is specifically designed to investigate the properties of b-hadrons and particularly the expected CP violation in their interactions. The LHCf (Large Hadron Collider forward, [54]) is split into two components, each 140 m from the ATLAS interaction point, and measures the number and energy of neutral pions from collisions there. TOTEM[2] [55] shares the interaction point with CMS and is – similar to LHCf – situated very close to the beam. Protons from elastic or quasi-elastic reactions with very low angles relative to the beam will be detected as well as the overall rate of inelastic reactions will be measured.

3.3. CMS – General overview

The Compact Muon Solenoid is one of the two general purpose detectors at LHC. It has a total weight of 12500 tons, a length of 21.5 m and a diameter of 15 m. In Figure 3.3, the essential setup of the detector is shown. Some of the main design concepts of the detector are represented in its name:

- *Compact:* The tracking system and all calorimeters are contained in a cylinder with a radius of 2.5 m. Adding the solenoid, return yokes, and muon chamber to the configuration increases the size significantly, but in comparison to ATLAS the detector covers only an eighth of the volume.
- *Muon:* Most muons observed in the detector originate from the decay of heavier particles and are therefore a good indicator for interesting physics processes occurring in the interactions (e.g. some of the proposed decay modes of a Higgs with a mass of $m_H \geq 150$ GeV [58]). Due to the massive amount of material between the interaction point and the muon chamber, almost exclusively the high-penetrating muons leave a signal in the muon chambers. This clean signature facilitates their use by the trigger system discussed in Section 3.6.
- *Solenoid:* CMS has a large superconducting solenoid at a radius of 3 m covering the tracking system and calorimeters with a 3.8 Tesla magnetic field. Tracks of charged particles are bent strongly in the transverse plane, which makes possible a precise momentum measurement by the tracker (see Figure 3.5).

CMS coordinate system: The coordinate system used by CMS has the origin centred at the nominal collision point inside the experiment. The x-axis is pointing radially inward towards the centre of the LHC, the y-axis is pointing vertically upward. The z-axis points along the beam direction toward the Jura mountains from LHC Point 5. The azimuthal angle φ is measured from the x-axis in the x-y plane (also called the transverse plane). The polar angle θ is measured from the z-axis. This defines the transverse momentum p_T, often used throughout the following, as

$$p_\mathrm{T} = p \cdot \sin(\theta) \tag{3.1}$$

---

[2] Total cross section, elastic scattering and diffraction dissociation measurement at the LHC

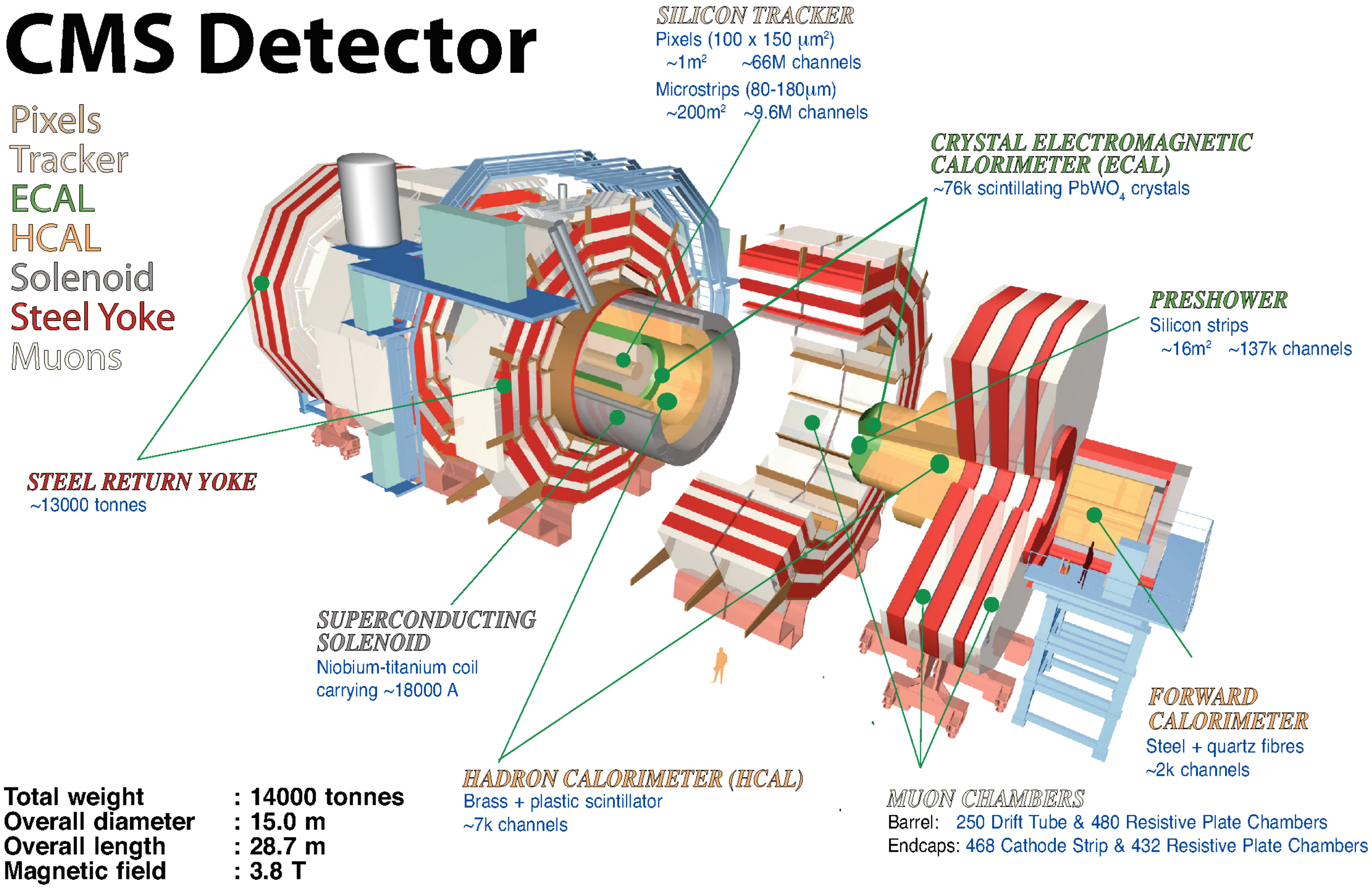

Figure 3.3.: Sketch of the CMS detector with key parameters and individually labelled subdetectors. Figure taken from [56]

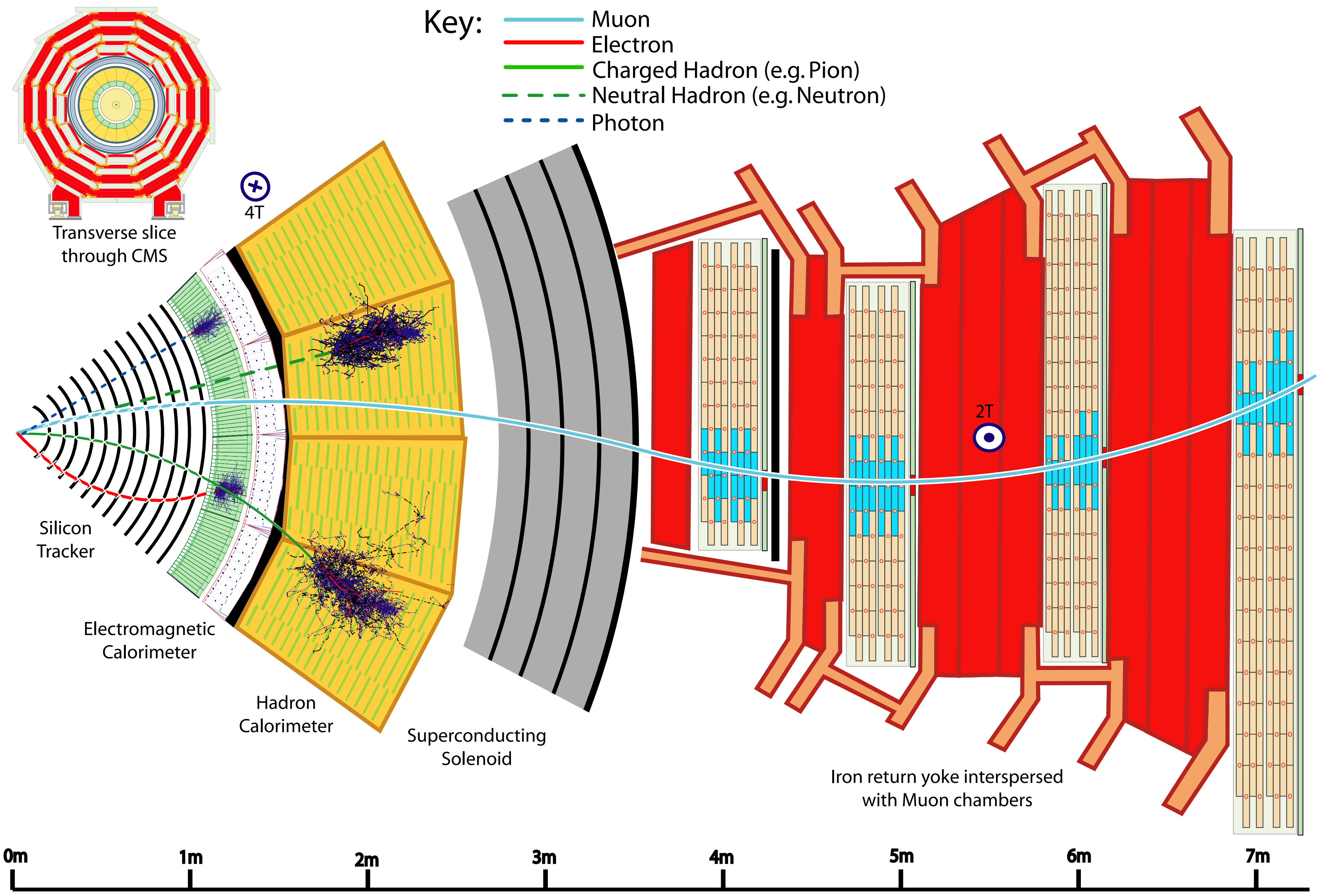

Figure 3.4.: Transverse slice through the CMS detector indicating the different onion-like particle detection layers. Indicated trajectories of particles show typical interactions and signal depositions in the detector. Figure taken from [57]

η denotes the pseudorapidity and is defined as

$$\eta = -\ln\left[\tan\left(\frac{\theta}{2}\right)\right] \tag{3.2}$$

The pseudorapidity ranges from infinity (parallel to the beam axis) to 0 (transverse to the beam axis) in this context. The pseudorapidity for massless particles is equal to the rapidity defined as

$$y = \frac{1}{2}\ln\left[\frac{E+p_z}{E-p_z}\right] \tag{3.3}$$

where E denotes the energy of the particle and p_z its momentum along the z-axis. It is a convenient observable in hadron collider physics, because the particle production is roughly constant in a wide rapidity range in terms of $\frac{dN}{dy}$ and differences of rapidities are Lorentz invariant.

Particle detection: In order to be able to reconstruct the particles created in the collision of the proton beams it is important to determine energy, momentum and the trajectories of the observable particles precisely. If this information is measured sufficiently accurate, it is possible to reconstruct the initial hard interactions.
Some particles leave the detector without interacting, i.e. they are invisible to the detector (e.g. neutrinos and some proposed SUSY-particles). These particles can only be reconstructed by building the detector as hermetically as possible and reconstructing the missing transverse energy $E_{\mathrm{T}}^{\mathrm{miss}}$ by forming the negative sum of all four momenta of detected particles and invoking momentum conservation.
In order to observe as many different particle types as possible in the detector there are different layers installed, each offering the ability to examine different classes of particles. For an illustration of the signals caused by different particles see Figure 3.4. The detector is described in detail in the technical design report [58, 59] and an article in the Journal of Instrumentation [60]. Some major aspects are summarised here:

1. *The tracker:* The tracker consists of silicon sensors that measure the position and energy loss of (charged) particles via ionisation. Due to the magnetic field of the solenoid, this allows to determine the trajectory, momentum, and sign of charge of the particles. Next to the beam pipe is a pixel detector with three barrel layers and two pairs of end disks. In outer regions, a silicon strip detector is employed with 10 layers in the barrel region and discs/endcaps at each end. The momentum resolution for muons is shown in Figure 3.5.
   The pixel detector is sensitive in the $|\eta| < 3.0$ region, the silicon strip detector is sensitive in the $|\eta| < 2.5$ region.

2. *Electromagnetic Calorimeter (ECAL) [61]:* The ECAL is built around the silicon tracker and is made of scintillating lead tungstate crystals ($PbWO_4$), making the ECAL sensitive to photons and electrons resulting in a precise measurement of their energies. See Section 3.4 for more details.
   The electromagnetic calorimeter is sensitive in the $|\eta| < 3.0$ region of the detector.

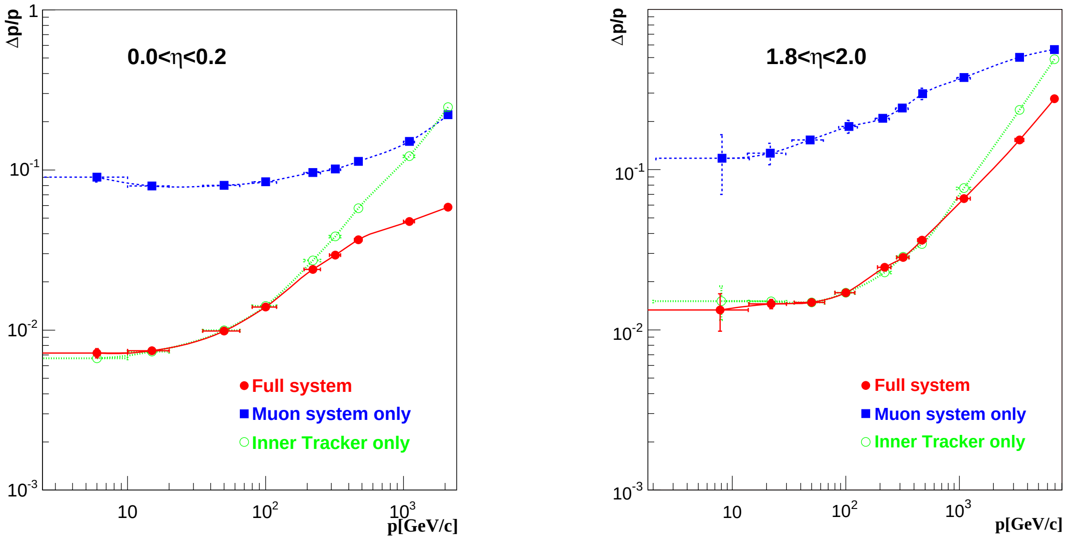

Figure 3.5.: The muon momentum resolution versus p using the muon system only, the inner tracker only, or both (full system). a) barrel, $|\eta| < 0.2$; b) endcap, $1.8 < |\eta| < 2.0$. [59]

3. *Hadronic Calorimeter (HCAL):* The HCAL is situated behind a lot of material in terms of radiation lengths, electrons and photons have already showered in the ECAL. It measures the energy of neutral and charged hadrons. See Section 3.5 for more details.
   The hadronic calorimeter is sensitive in the $|\eta| < 5.0$ region.

4. *Muon detectors:* The muon detector uses three different types of gaseous detectors to identify the muons and measure their momenta. The different types are adapted to the expected particle flux and radiation background. Drift tubes (DT) are installed in the barrel region, cathode strip chambers (CSC) in the endcaps, and resistive plate chambers (RPC) in both parts.
   A second measurement of the momentum in addition to that in the tracker is possible, because there is a strong magnetic field (2 Tesla) in the reverse direction of the solenoid's field induced by the return yokes in the muon chamber. The combination of both detector components improves the momentum resolution for high p_{T} muons significantly (see Figure 3.5).
   The muon chamber is sensitive in the $|\eta| < 2.4$ region.

3.4. CMS – Electromagnetic calorimeter

The electromagnetic calorimeter is built of 61200 lead tungstate crystals in the barrel part and 7324 crystals in each endcap. Lead tungstate has a high density ($8.3\,\mathrm{g/cm^3}$), a short radiation length (0.89 cm), and a small Molière radius [59] (2.2 cm), allowing for the construction of a very compact calorimeter with a fine granularity. The material budget

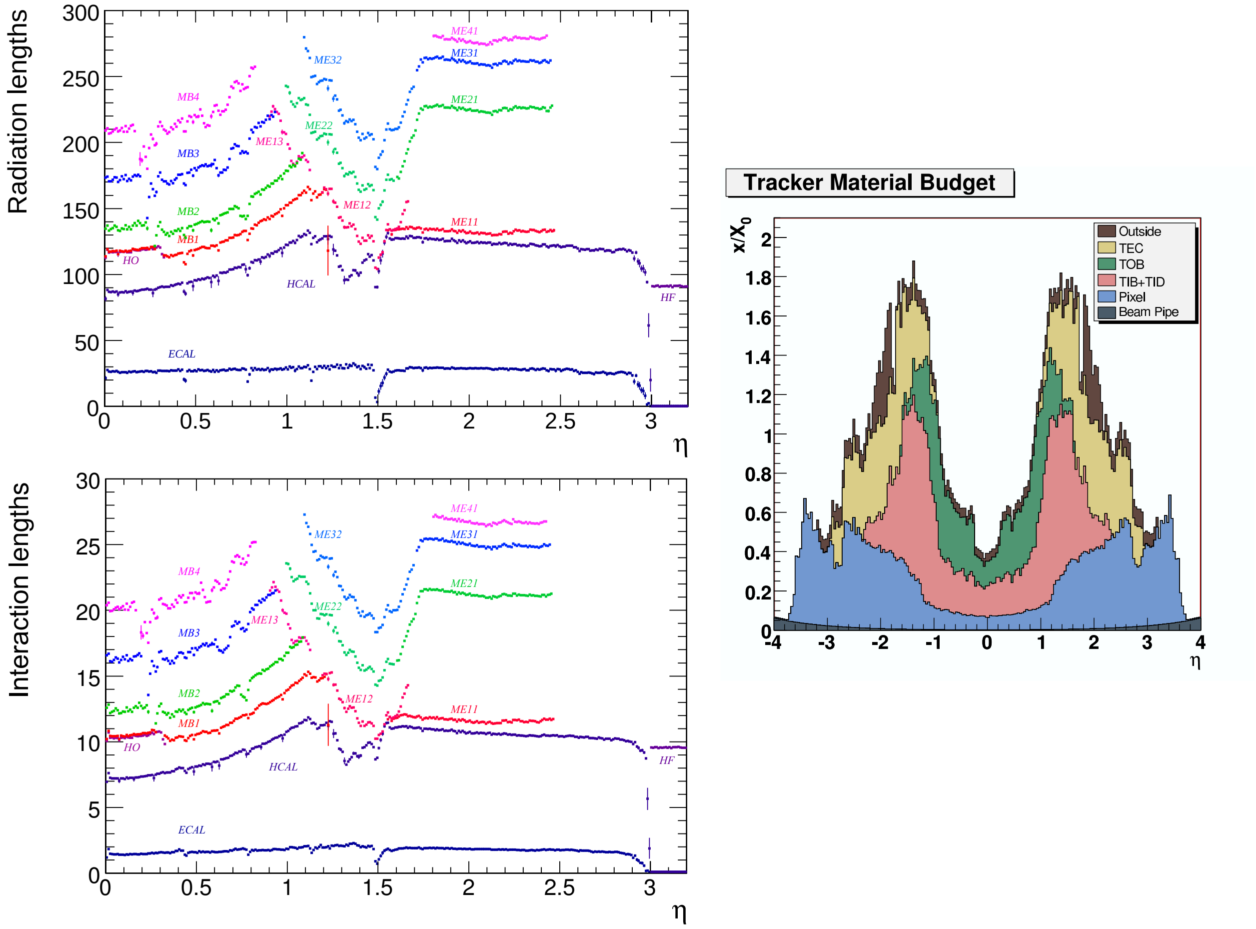

Figure 3.6.: Top left: material budget in terms of the radiation length as a function of the pseudorapidity after the ECAL, HCAL and at different muon stations; Lower left: material budget in units of interaction length as a function of the pseudorapidity after the ECAL, HCAL and at different muon stations; Right plot: material budget in units of the radiation length as a function of η for the inner detector (tracker); [59] and [60]

in front of the electromagnetic calorimeter has been a major concern for the construction of CMS as any material in front of the calorimeters can lead to interactions of electrons and photons with the material, distorting the measurement in the calorimeter. The material budget in terms of the radiation length and the interaction length is depicted in Figure 3.6.

Lead tungstate is relatively radiation hard and the scintillation process is very fast (80 % of the photons are emitted within 25 ns). Silicon avalanche photodiodes in the barrel and vacuum phototriodes in the endcaps are used as sensitive photodetectors for the readout. These detectors have an intrinsic gain and can therefore make use of the low photon yield (approximately $30\gamma/\,\text{MeV}$). In order to circumvent the temperature dependence of the crystals' and photodetectors' sensitivity, the temperature is stabilised.

The energy resolution of the electromagnetic calorimeter has been evaluated in test beam data [59] yielding

$$\left(\frac{\sigma}{E_{\text{electron}}}\right)^2 = \left(\frac{3.63 \pm 0.1\%}{\sqrt{E_{\text{electron}}/\,\text{MeV}}}\right)^2 + \left(\frac{124\,\text{MeV}}{E_{\text{electron}}}\right)^2 + (0.26 \pm 0.01\%)^2 \tag{3.4}$$

Barrel: The barrel section (EB) has an inner radius of 129 cm and covers the pseudorapidity range of $0 < |\eta| < 1.479$. The crystals are mounted quasi-projective such that they cover 0.0174 in $\Delta\varphi$ and $\Delta\eta$. The crystals have a length of 23 cm, corresponding to $25.8\,X_0$ and have a front area of $\approx 22 \times 22\,\text{mm}^2$.
Endcap: The endcaps (EE) cover the pseudorapidity range of $1.479 < |\eta| < 3.0$ and are situated ± 314 cm from the nominal vertex. The crystals have a length of 22 cm, corresponding to $24.7\,X_0$, and have a front area of $\approx 28.6 \times 28.6\,\text{mm}^2$. The crystals are mounted in 5×5 units called "supercrystals" on semi-circular aluminium plates. In front of the endcaps a preshower detector is placed. It aims at identifying photons originating from neutral pions within $1.653 < |\eta| < 2.6$.

3.5. CMS – Hadronic calorimeter

Similarly to the ECAL, the hadronic calorimeter measures the energy of the incident particles. The design of the HCAL has been constrained strongly by the size of the solenoid magnet surrounding it. A maximal amount of material in terms of interaction length has to be placed in the available volume. A combination of brass plates and thin slices of plastic scintillators, i.e. a sampling calorimeter, has been chosen for the barrel and endcap region. The calorimeter is mounted and segmented quasi-projective. The signal of all sampling layers in these projective "towers" is combined for readout. A detailed table of the segmentation of the HCAL readout towers is given in the Appendix C
.
The performance of the hadronic calorimeter is usually expressed in terms of the jet-energy resolution. The jet-energy resolution has been estimated in the barrel region using simulations in [59] as

$$\left(\frac{\sigma}{E_T}\right)^2 = \left(\frac{1.25}{\sqrt{E_T/\,\text{GeV}}}\right)^2 + \left(\frac{5.6\,\text{GeV}}{E_T}\right)^2 + (0.033)^2 \tag{3.5}$$

where E_T is the transverse energy of jets.

Hadron Barrel: The barrel part covers the pseudorapidity range of $0 < |\eta| < 1.305$ with a segmentation of 0.087 in $\Delta\varphi$ and $\Delta\eta$, which corresponds to 2304 towers in total. The towers consist of 15 brass plates (each 5 cm thick), the plastic scintillator layers are 3.7 mm thick (first layer after ECAL 9 mm).
Hadron Outer: The hadron outer system is situated inside the barrel muon system and covers the pseudorapidity range of $0 < |\eta| < 1.26$. It enhances the effective thickness of

the hadronic calorimeter to more than 10 interaction lengths and thus contains energy from highly penetrating hadronic showers. Thereby it can reduce the tails in the energy resolution function and improve the resolution of missing transverse energy. However, it is not yet used for physics studies.

Hadron Endcap: The endcap part covers the pseudorapidity range of $1.3 < |\eta| < 3.0$ with 14 towers in η with a varying segmentation on $\Delta\varphi$ and $\Delta\eta$. In the two endcaps there are 2304 towers in total (as many as in the barrel part).

Hadron Forward: The HF extends the sensitive region out to $|\eta| < 5$ and is needed for forward jet physics and a good resolution of the missing transverse energy. The front face of the absorber is placed 11.2 m from the interaction vertex, the depth of the absorber is 1.65 m. The HF is made of steel/quartz fibres of different lengths in which the signal is caused by Cerenkov light emitted in the quartz fibres. There are 900 towers in the HF in total.

3.6. CMS – Trigger

Once the LHC is running at nominal conditions, the proton bunches will collide at a rate of 40 MHz. For each of these bunch crossings about 20 proton-proton interactions will take place at the same time (the so called pile-up). This huge amount of data is unmanageable by current data storage systems and it is indeed not necessary to store all data: Most of the interactions are very soft (i.e. with a low momentum transfer) and have been studied in detail before. The cross sections expected for previously undiscovered physics are so low that only very few such events are expected in the large background of QCD-events. This is depicted in Figure 3.7, in which the cross sections and rates of various physics processes are depicted as a function of the centre-of-mass energy.

Currently, data from about 100 bunch crossings/s can be archived. In order to reduce the event numbers by such an amount (factor of 10^6), CMS has adopted a two-fold triggering system: A fast Level-1 trigger with custom-built electronics and a high level trigger system that is running on a large scale processor farm and is very adaptable.

Level-1 trigger: The Level-1 trigger decision relies mainly on p_T-thresholds and cuts on global variables like the sum of E_T and the missing transverse energy $E_\mathrm{T}^\mathrm{miss}$. Reduced-granularity and reduced-resolution data from the calorimeters and the muon-system are the information used to decrease the number of events by roughly a factor of 1000.

The Level-1 trigger decision has to be very fast as the full resolution data can only be stored in pipelined memories on the experiment for a short time (order of $5\,\mu$s). This is achieved by custom hardware processors. Once a positive trigger decision is made, the data are transferred to front-end readout buffers, where they are available for the higher level trigger.

High-Level triggers (HLT): Starting from the readout buffers, the total event size is reduced to about 1.5 MB per pp-interaction by signal processing and data compression. The events are then transferred at a rate of 100 kHz to processor farms. The software for the HLT decision is based on the CMS software also used for analyses of the final data. As the HLT-software does not need to run on custom hardware, it can be adapted

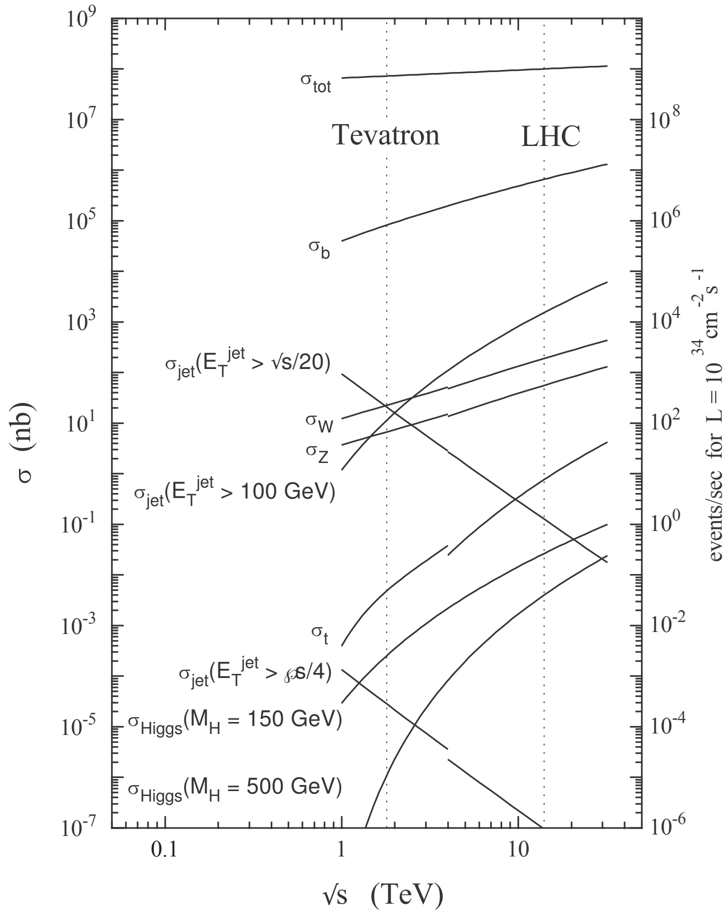

Figure 3.7: Cross section and rates for various processes in (anti)proton-proton collisions at nominal luminosity of the LHC; [62]

to current needs. The output rate is of the order of 100 events per second. These events are then permanently stored.

3.7. 2010 pp run

During the 2010 running period of the LHC, the accelerator was operated at a beam energy of 3.5 TeV. The operation at higher energies has been delayed due to an incident on 19 September 2008 [63]. Nevertheless, the 2010 run has been a big success for all LHC experiments: During the data taking period from 30 March 2010 until 29 October 2010, a total integrated luminosity of 47.03 pb^{-1} has been delivered by LHC at the CMS experiment. As of the beginning of November, 34.74 pb^{-1} have been recorded and certified for data analysis within CMS (see Figure 3.8 for delivered and recorded integrated luminosity). All subdetectors of CMS have been working with a high efficiency during the data taking period. A peak instantaneous luminosity of $2.04 \cdot 10^{32}\text{cm}^{-2}\text{s}^{-1}$ could be achieved during the last week of pp-runs. With these first high energy data, many new results have already been published [64, 65], including the CMS publication on the “Observation of long-range, near-side angular correlations in proton-proton collisions at the LHC ” (see [66] for details).

After a heavy-ion running period and a technical shutdown, the LHC is planned to again operate proton beams at the end of February 2011 and to collect data of the order of 2 fb^{-1} during the 2011 run (see [67] for a review of LHC operation).

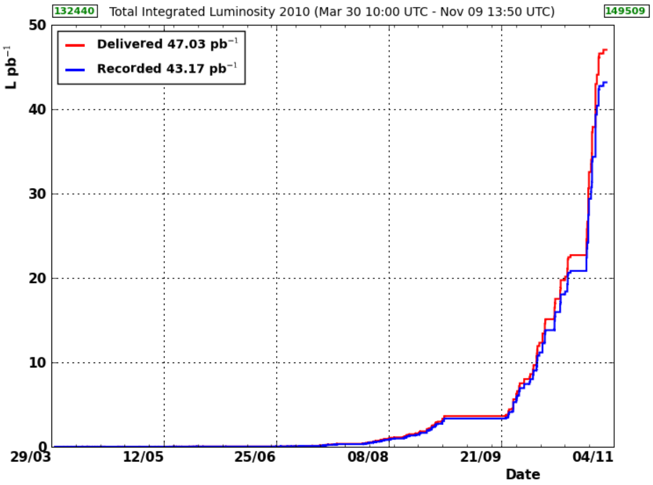

Figure 3.8.: Total integrated luminosity at LHC point 5 (CMS) for stable beams at 7 TeV centre-of-mass energy; see [68]

Chapter 4.

Jet reconstruction and jet-energy corrections at CMS

In the following, the jet reconstruction at CMS will be described. As discussed in Section 2.2, jets in high-energy proton-proton collisions can be traced back to the initial hard scattering process of two incoming partons producing outgoing partons. These outgoing partons produce a shower of partons predominantly collimated along the direction of the outgoing partons. The partons in these showers hadronise to observable colourless particles. These particles propagate through the detector and interact with the material. Combining energy depositions in the calorimeters with jet algorithms (see Section 4.1) leads to jets at the calorimeter level, the so-called CaloJets mainly used in this thesis; the different jet types available within CMS are briefly discussed in Section 4.2.

In order to relate the electronic signals from the detector with physics processes initiated by the hard scattering, simulations are an important tool. Starting from the level of stable particles discussed in Section 2.2, the propagation of these particles and their interaction with the material and magnetic field in the detector are simulated within the CMS software (CMSSW) utilising the GEANT 4-toolkit [69]. Simulated energy deposits in the detector are then processed within CMSSW to simulate the response of the sensors and the readout electronics. Starting from these signals, the event reconstruction is the same for data and simulated data.

In Section 4.3, the jet-energy correction approach of CMS is presented. It relates, on

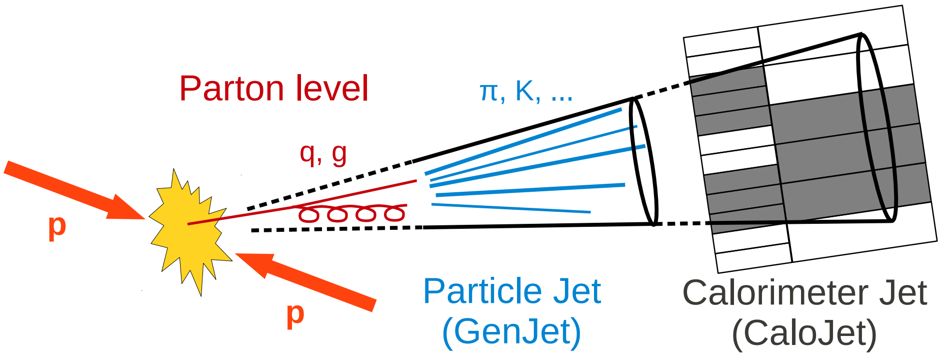

Figure 4.1.: Different levels of jet interpretation, adapted from [70].

average, the measured jets to a jet definition independent of the detector response, the "particle level jet" as depicted in Figure 4.1. These particle level jets are determined by applying jet-finding algorithms to the stable particles from simulations and are called GenJets at CMS.

4.1. Jet-finding algorithms

Even though jets can be easy-to-spot objects in events with little other activity, the definition and study of jet-finding algorithms is a subject of intensive scientific study. Jet-finding algorithms provide a set of rules for grouping input objects (ideally particles) into jets, depending on one or more parameters (usually at least a distance parameter). The input objects used for the clustering may vary as is discussed in Section 4.2. Traditionally, the energy depositions in the calorimeters are the starting point for clustering jets.

Key requirements for jet-finding algorithms (that were not fulfilled by early jet-finding algorithms) are that they are insensitive to the addition of soft radiation (infrared safe) and collinear splitting of particles (collinear safe). Some of the key points of the different types are summarised here, a detailed study of different jet-finding algorithms is performed in [71]. Within the CMS collaboration, the FastJet implementation [72] of jet algorithms is used for reconstruction. In general, there are two main types of jet-finding algorithms: Cone-type algorithms and sequential-clustering algorithms. Figure 4.2 illustrates differences in the clustering for a cone-type and three sequential-clustering algorithms.

4.1.1. Cone-type algorithms

These algorithms are based on the idea that the hadrons produced during the fragmentation process following a hard scattering form a collimated shower in the direction of the initial partons. A cone in η and φ, approximately in the direction of the jet-initiating parton, is then defined to include the energy depositions of the jet. The cone is usually defined with a radius $R = \sqrt{\Delta\eta^2 + \Delta\varphi^2}$. The first jet algorithm was a cone-type algorithm and is described in [15]. Since then, a lot of effort has been put into improving these cone algorithms. The main issues faced included the choice of where to place the cones and how to handle potentially overlapping cones.

Iterative cone algorithm: The Iterative Cone algorithm is used by CMS for triggering purposes as it is a very fast algorithm. However, the algorithm is not infrared and collinear safe. It takes a p_T-ordered list of all input objects and starts with the highest p_T-object as a seed. A trial cone with the radius R is formed and the four-momenta of all input objects within the radius are summed. In the direction of the trial jet axis, a new trial cone is formed. This procedure is repeated until the direction of the trial jet changes by less than $\Delta R = 0.01$ and the energy of the trial jet changes by less than 1% between iterations. Then, the trial jet is declared as stable and all input objects included in the jet are removed from the list.The clustering ends, when no energy depositions

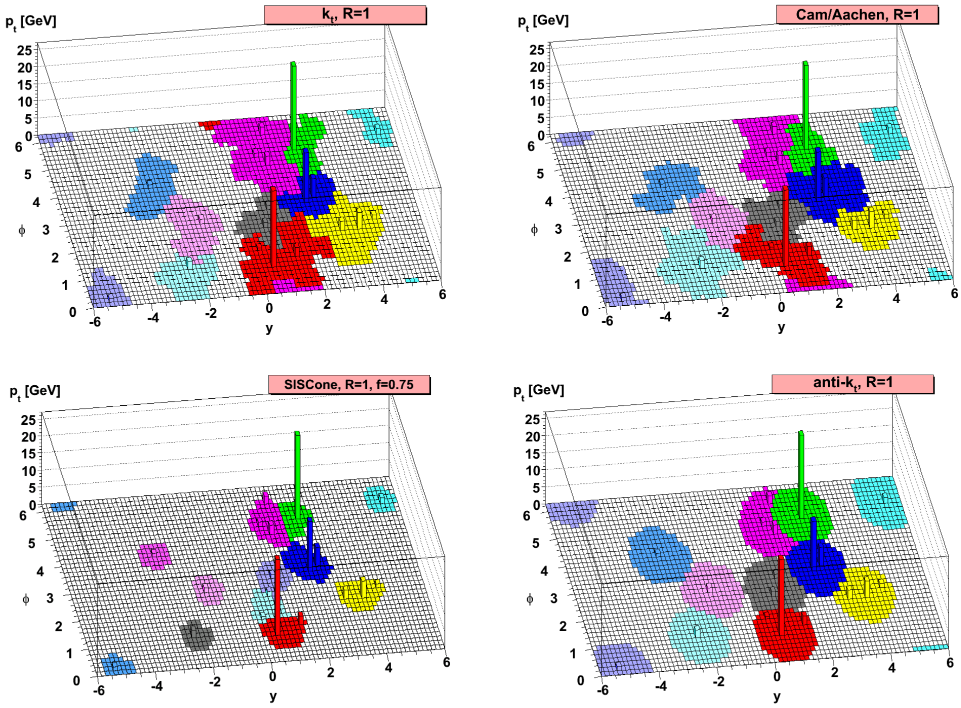

Figure 4.2.: A sample parton-level event (generated with Herwig). Many random soft ghosts have been added to illustrate the "active area" of the jets; taken from [73]

exceeding the seed threshold remain unclustered.

Seedless infrared safe cone algorithm: The so-called SIScone algorithm as described in [74] has been developed to be both explicitly collinear and infrared safe. It does not use seeds, but instead considers all possible stable jet cones and has a dedicated split and merge procedure for overlapping jets. However, the algorithm is very CPU-time-consuming for events with many input objects and thus not used as the standard algorithm within the CMS collaboration.

4.1.2. Sequential-clustering algorithms - anti-k_t

The jets resulting from sequential-clustering algorithms do not necessarily have a regular shape comparable to cone algorithms. Instead they can form jets of quite irregular shapes as depicted in Figure 4.2. The anti-k_t-algorithm belongs to a family of clustering algorithms (k_t and Cambridge/Aachen) based on a similarly defined distance measure between the objects that are to be clustered.

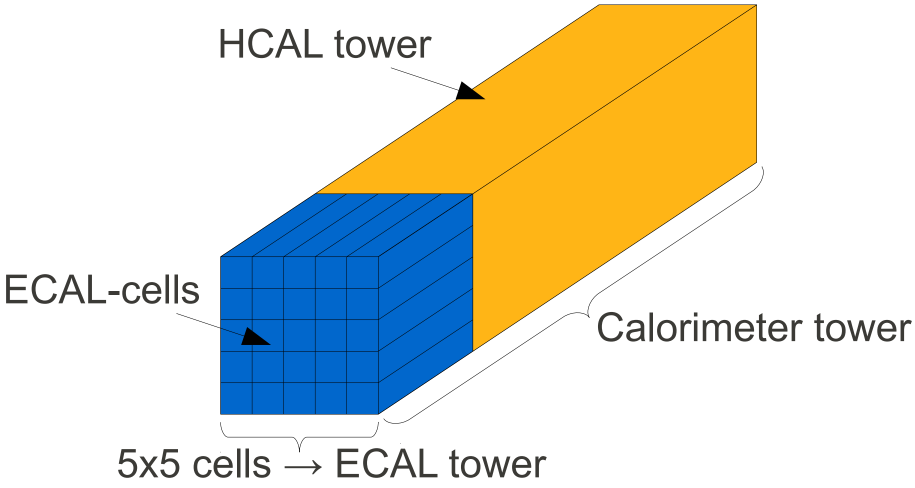

Figure 4.3.: Sketch of calorimeter towers used for jet clustering. 5x5 ECAL-cells and one HCAL tower are logically combined to form a calorimeter tower in the barrel region. The granularity differs in other detector regions.

The distance measures used by the three jet algorithms are

$$d_{ij} = min(p_{T,i}^{2k}, p_{T,j}^{2k})\frac{\Delta_{ij}^2}{R^2} \tag{4.1}$$

$$d_{iB} = p_{T,i}^{2k} \tag{4.2}$$

where R is the distance parameter, $k = 1$ for the k_t-algorithm, $k = -1$ for the anti-k_t-algorithm, and $k = 0$ for the Cambridge/Aachen-algorithm. Δ_{ij} denotes the distance in η-φ space as

$$\Delta_{ij}^2 = (\eta_i - \eta_j)^2 + (\varphi_i - \varphi_j)^2 \tag{4.3}$$

All distances d_{ij} and d_{iB} are calculated and the minimal distance among all distances is determined. In the case where the minimum is d_{ij}, objects i and j are recombined into a single new object by addition of their four-momenta and all distances are recalculated. In case the minimum is d_i, this object i is regarded as a jet and removed from the input list. This process continues until all input objects are clustered.
The anti-k_t-algorithm produces jets with a very regular shape. It is regarded as an infrared and collinear safe replacement of the iterative cone algorithm and has become the standard jet-finding algorithm at CMS. It is discussed in detail in [73]. In the following analysis, jets reconstructed with the anti-k_t-algorithm and a distance parameter of $R = 0.5$ are used.

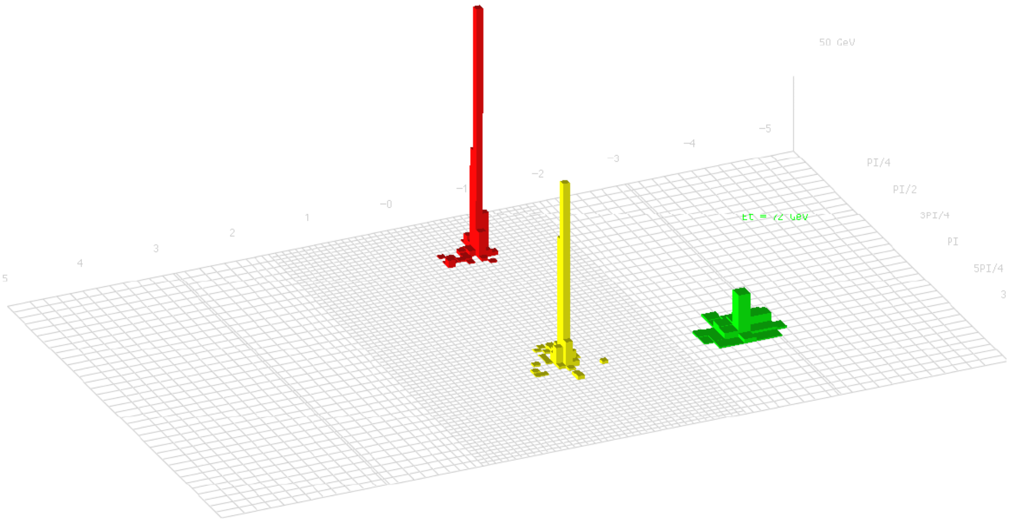

Figure 4.4.: Segmentation of the HCAL towers in η and φ; [59]

4.2. Reconstructed jet types at CMS

Calorimeter jets - CaloJets: In the case of calorimeter jets, the input objects for the jet clustering are formed from measurements of the energy depositions in the electromagnetic and the hadronic calorimeter.

Starting from electronic signals delivered by the detector (or a simulation), a local reconstruction and calibration is performed separately for the ECAL and HCAL cells. The hadronic calorimeter has a coarse granularity in comparison to the ECAL. Therefore, the HCAL-granularity determines the size of projective "towers" that combine the measurement of cells from both calorimeters. A sketch of the so-called "calorimeter towers" is shown in Figure 4.3 for the barrel region. The energy of these towers is calculated by summing up the energy of all contributing readout cells passing the online zero-suppression threshold and additional offline thresholds (current readout thresholds in [75]). The resulting measurement of energy depositions is the starting point for jet-finding algorithms, which take these measured depositions as four momenta of massless particles with the direction determined by the centre of the tower and the interaction point. The segmentation of 0.087 in $\Delta\varphi$ and $\Delta\eta$ in the barrel becomes coarser in the endcap and forward region. A table of the HCAL-segmentation is given in Appendix C. There are 4176 towers in total as depicted in Figure 4.4.

As calorimeter jets are only reconstructed from one type of detectors, they are the simplest reconstructed jet type. Calorimeter jets have been used at previous experiments and have been used extensively for physics studies at CMS [58]. However, their performance suffers from the relatively poor energy resolution of the very compact hadronic calorimeter of CMS. In the following, it will be discussed, whether additional jet-energy corrections help to improve on this.

JPT jets: Other jet types utilising more subdetectors are explored and used at CMS.

For the so-called Jet-plus-track jets (JPTJets) tracks are associated to jets based on the distance between the jet axis and the track at the interaction vertex. These tracks are classified as in-cone tracks and out-of-cone tracks depending on whether they reach the calorimeter within the jet reconstruction cone or not. The expected calorimeter measurements of the in-cone tracks are subtracted from the calorimeter measurement and replaced by the precise momentum measurement of the tracker. The measurement of out-of-cone tracks is also taken into account so that it is possible to improve the jet-energy resolution significantly (for details see [76]).

Particle flow jets: Particle flow (PF) is an attempt to identify and reconstruct individually each particle originating from the proton-proton collisions combining the information from all sub-detectors. The resulting reconstruction of jets leads to an improved performance with respect to the jet-energy resolution. Particle-flow jets (PF-jets) are composed of individually identified charged hadrons, photons, electrons, and neutral hadrons in the barrel region, i.e. within the reach of the ECAL and the tracker. In the forward regions, they are built of measured hadronic and electromagnetic energy deposits as only the HF calorimeter extends to this region with its long and short fibres. The detailed reconstruction is explained in [77] and the commissioning in data from pp-collisions is discussed in [78]. In the particle flow approach, charged hadrons are identified to carry, on average, 65% of the jet energy in the tracker-covered region, photons 25%, and neutral hadrons 10% of the jet energy, restricting the influence of the HCAL resolution to the small contribution of neutral hadrons.

Particle jets - GenJets: When studies are performed on simulated data, an additional jet type, already mentioned before, is available. The so-called GenJets are clustered from "stable particles" as defined in Monte Carlo event generators (see Section 2.2.3). They are independent of the detector response and therefore regarded as a reference, when the energy of measured jets is calibrated as discussed in the following Section 4.3.

4.3. Jet-energy corrections at CMS

It is the goal of jet-energy corrections at CMS to correct the detected jets on average to an observable definition that is independent of the response of the CMS detector. This is achieved by correcting the energies of uncorrected CaloJets, on average, to the energy of corresponding GenJets.

The ratio of the measured transverse momentum and the transverse momentum of GenJets is defined as the jet-energy response

$$R = \frac{p_T^{meas}}{p_T^{gen}} \tag{4.4}$$

The strategy deployed within CMS for jet-energy corrections, is discussed in [79], where a factorised approach to jet-energy corrections has been proposed. The current status of jet-energy corrections at CMS is presented in [80].

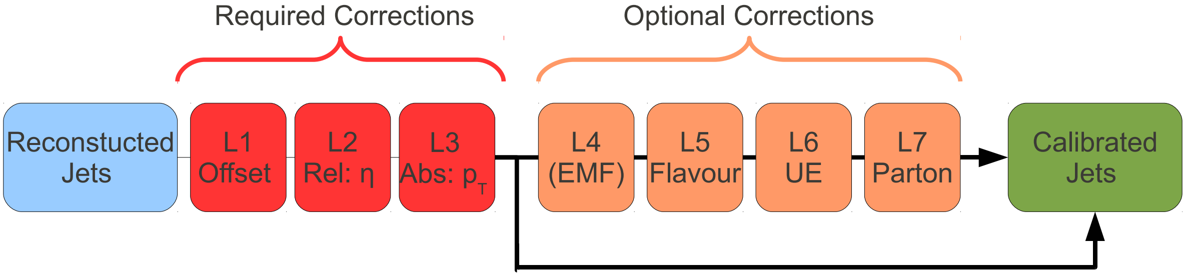

Figure 4.5.: Sketch of factorised approach to jet-energy corrections

4.3.1. Factorised approach

In the factorised approach adapted by CMS, the jet-energy calibration is a sequential procedure, divided into levels as depicted in Figure 4.5. The correction factors corresponding to each level are applied in this fixed sequence. Even though there can be correlations between these factors, this factorisation allows for a reduction of the systematic uncertainties: Each level is studied and determined individually, providing the possibility to parallelise the correction determination and get a better understanding of the different sources of systematic uncertainties.

This has proven beneficial at the Tevatron experiments, where it was possible to use collider data to determine the jet-energy scale in separate steps using individual physics processes due to the factorisation. At present, the CMS jet-energy corrections are determined from simulations so that they avoid biases that would be introduced by data-driven methods [79] (e.g. biases due to the energy resolution and p_T-spectrum). In order to avoid these biases, the corrections are determined and validated as a function of p_T^{gen}.

The corrections derived from simulated data are applied up to level 3 as default. In the case of data analysis, an additional residual correction determined from data is applied to the data, in order to match the results from simulations and data. Higher levels of jet-energy corrections are planned to be incorporated in the future, but are not yet fully deployed.

4.3.2. Required corrections

The "required" corrections up to to level 3 are compulsory to relate, on average, the energy of reconstructed jets to that of GenJets. The level 1 correction accounts for pile-up and electronics noise, level 2 corrects for the relative response difference with respect to the barrel as a function of η, and level 3 corrects for the p_T-dependence of the absolute jet-energy scale.

L1 - Offset: When the jet energy is determined, there are inevitable additional contributions to the measured calorimeter energy depositions that lead to an offset of the measured jet energy. These contributions are due to pile-up events (additional proton-

proton collisions close in time to the hard scattering process of interest[1]) and electronics noise. Electronics noise produces an energy offset that can be subtracted from the jet energy.

In [81], the offset has been found to be below 4 GeV in energy and below 0.3 GeV in mean p_{T} when examining Zero Bias and Minimum Bias events[2]. The typical number of pile-up events in the dataset used in that study and in the analysis on data, described in Chapter 8, was approaching one on average [80], thus there is no explicit offset correction applied and the offset observed is incorporated into the systematic uncertainties as given in [80].

L2 - Relative: The level 2 correction aims at removing the dependence of the jet response on the pseudorapidity η as depicted in Figure 4.6(a). Right now, the relative correction is determined as described in [84] from simulations. The current parametrisation uses an 82-fold binning in η, corresponding to the HCAL-granularity.

The barrel region is the easiest to calibrate in absolute terms, contains the largest statistics, provides the highest p_{T}-reach, and only a slight η-dependence is observed there. It is therefore chosen as reference region to which the jet response in other pseudorapidity regions is scaled.

The current parametrisation [85] reads as:

$$c_{L2}(p_{\mathrm{T}}) = \sum_{i=0}^{3} b_i \left(\log_{10}(p_{\mathrm{T}})\right)^i + b_4 \left(\frac{p_{\mathrm{T}}}{500}\right)^3 \tag{4.5}$$

L3 - Absolute: After the application of the relative correction, the mean response as a function of p_T^{gen}still differs from unity (see Figure 4.6(b) and Figure 4.7). The absolute correction (L3) corrects for this dependence of the jet response on the jet's transverse momentum p_{T} and provides the complete correction back to the particle jet level. As the response is uniform in η after the L2-correction, the absolute scale only has to be fixed precisely in an arbitrary pseudorapidity region. The natural choice is again the barrel region as it is equipped with precise tracking and the high-resolution electromagnetic calorimeter. At present (November 2010), the correction factors are derived from simulations using the following parametrisation [85]:

$$c_{L3}(p_{\mathrm{T}}^{L2}) = b_0 + \frac{b_1}{\log_{10}^{b_2}(p_{\mathrm{T}}^{L2}) + b_3} \tag{4.6}$$

where p_{T}^{L2} is the transverse momentum of the L2-corrected jet. After the application of the jet-energy corrections including the L3-correction, the absolute and relative average energy scale of jets is regarded as correct at CMS. The jet response of L2L3-corrected

---

[1] Both, in-time pile-up from the same bunch crossing and out-of-time pile-up from previous and following bunch crossings, can contribute to the total offset

[2] Collisions of hadrons with a high momentum transfer (hard collisions) between the interacting partons can be described successfully by perturbative QCD. However, most of the collisions are soft interactions with a low momentum transfer referred to as “Minimum Bias“ events. It is expected that about 20 such events will occur during every bunch crossing at nominal luminosity at LHC. To trigger on “Zero Bias“ events no event activity is required at all, it is triggered on the bunch-crossing time. [20, 82, 83]

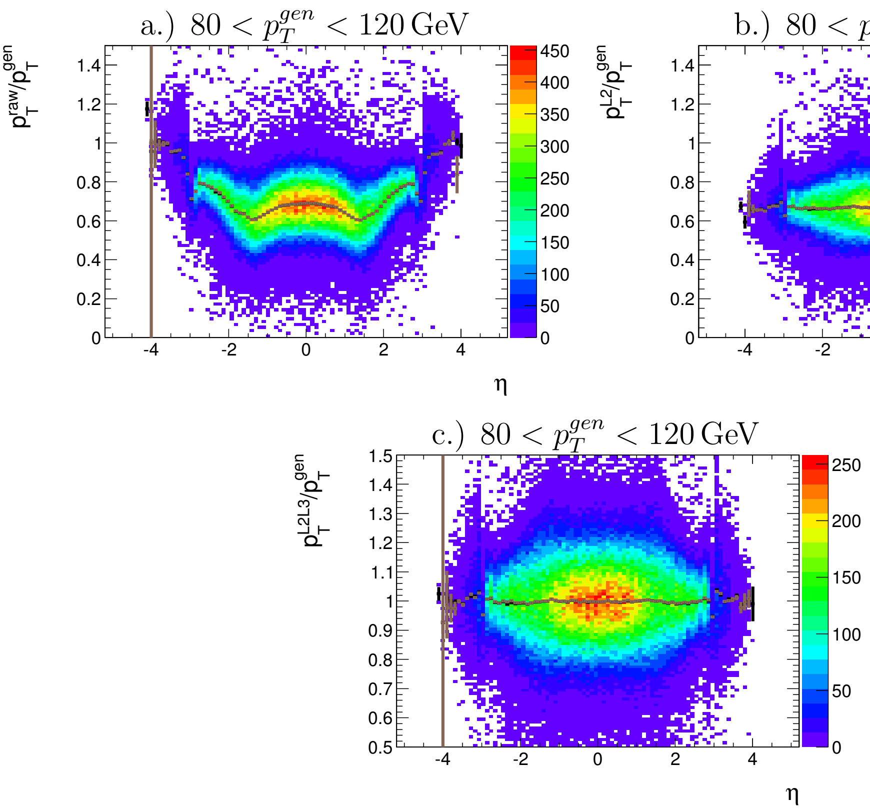

Figure 4.6.: Jet-energy response of uncorrected calorimeter jets (a), L2-corrected calorimeter jets (b), and L2L3-corrected calorimeter jets (c, different y-scale) as a function of η for $80 < p_T^{gen} < 120\,\mathrm{GeV}$, generated using a PYTHIA QCD simulation with GEANT simulation of the CMS detector. Black: Mean of response in bins of η; Brown: Gaussian mean of response in bins of η.

jets is defined as

$$R_{L2L3} = \frac{p_T^{L2L3}}{p_T^{gen}} \tag{4.7}$$

where p_T^{L2L3} is the transverse momentum of the L2L3-corrected jet. The jet response after the L2L3-corrections is, on average, equal to one (see Figure 4.7).

4.3.3. L4 - Electromagnetic fraction

The so-called L4-correction is the first of several optional corrections in addition to the compulsory L2L3-corrections. It will be studied in chapters 5-7, to what extent an additional correction, depending on characteristics of the jets, improves the overall resolution of the energy measurement of individual jets. A level 4 correction using the electromagnetic fraction EMF has been examined in [86]. Currently, there is no active development on the EMF-correction as it has been found to yield only small resolution improvements [86, 87].

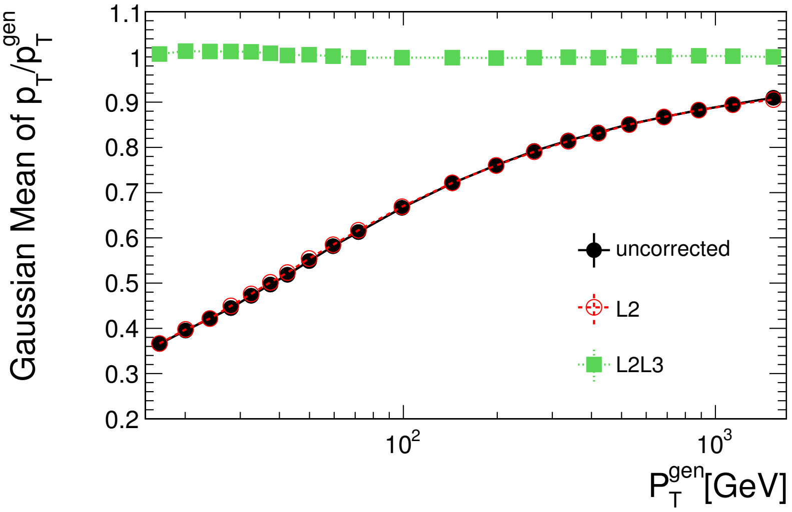

Figure 4.7.: Gaussian mean of the uncorrected response (black circles), the L2-corrected response (red open circles), and the L2L3-corrected response (green squares) for calorimeter jets in the barrel region.

4.3.4. Other optional corrections

In the factorised jet-energy correction approach of CMS, more optional correction steps are planned. Whether they need to be applied or not depends strongly on the individual event selection and analysis strategy, and not all optional corrections are fully functional in current releases of the CMS software. With increasing integrated luminosity, these optional corrections will become more important for lowering systematical uncertainties.
L5 - Flavour: The jet-energy corrections up to level 5 are derived under the premise that the event samples, the corrections are applied to, have the same flavour composition as the PYTHIA QCD dijet samples used for the derivation of the corrections. Here and in the following, the flavour is determined using the ”algorithmic definition“ as given in [88]. It determines the jet flavour from a spatial matching in $\Delta R < 0.3$ of the GenJet and the final state partons, i.e. after showering and radiation. A jet is labelled as a b- or c-jet, if a b- or c-quark is within this cone. Otherwise the flavour of the parton with the highest p_T within $\Delta R < 0.3$ is assigned as the jet flavour. As a strong dependence of the mean jet response on the flavour is observed (see Figure 4.8) for calorimeter jets, a different flavour composition can lead to a significantly differing mean jet response. A large fraction of this effect is assigned to a different particle composition and particle p_T-spectrum of the jets. However, the corrections planned for level 5 require a flavour hypothesis for the parton, from which the jet originated. This complicates their application. The current status of flavour specific jet-energy corrections is summarised in [89, 90].
L6 - Underlying event: The underlying event as discussed in Section 2.2.4 can lead to additional energy depositions in the detector. It is not clear to which extent the underlying event can be separated from the jet itself, but it is planned to supply a generic

a.)

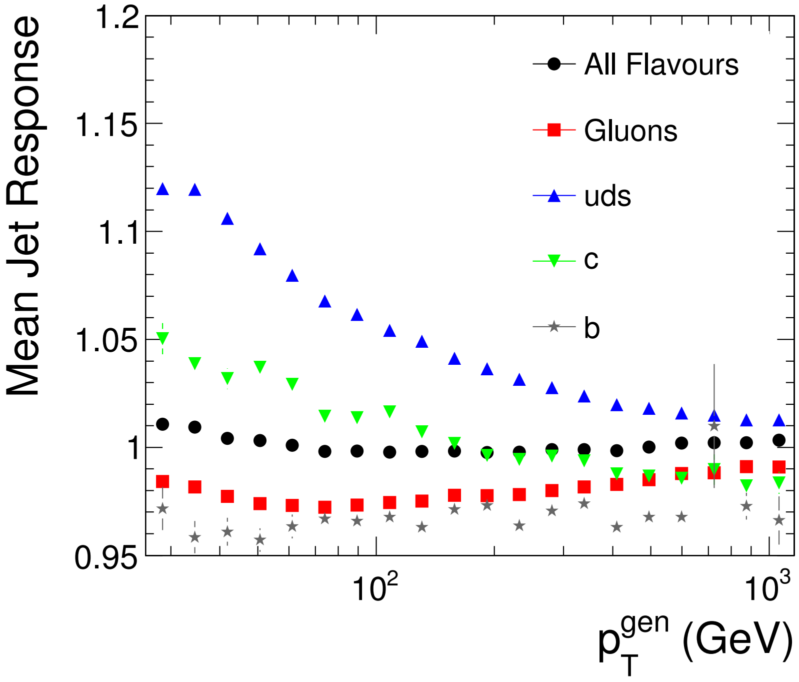

b.) $30 < p_T^{gen} < 35\,\mathrm{GeV}$

$230 < p_T^{gen} < 300\,\mathrm{GeV}$

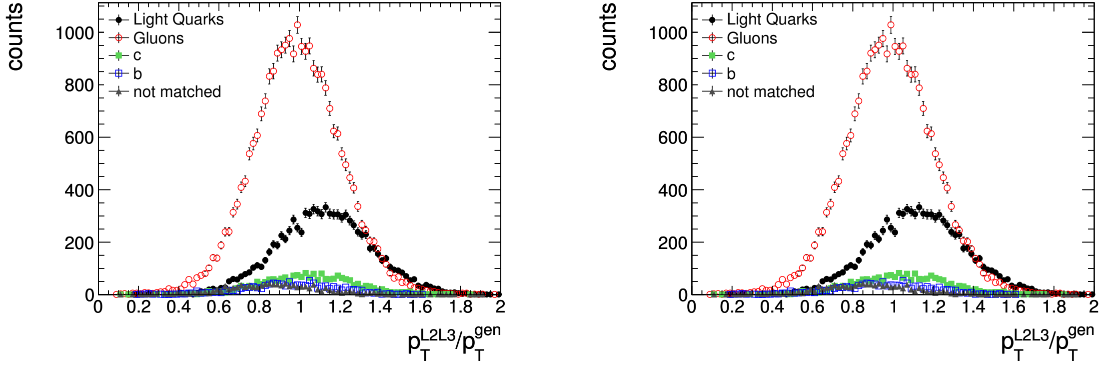

Figure 4.8.: a.) Mean jet response of L2L3-corrected jets matched to various flavours as a function of p_T^{gen}.
b.) Distribution of R_{L2L3} for various flavours in two p_T^{gen}-regions.

correction as a component for the correction to the parton level that has to be adapted for specific analyses [79].

L7 - Parton: The parton correction aims to correct the energy of the particle level jet back to the parton level (see Figure 4.1) and has been discussed in [91]. This is conceptually difficult as the connection of parton p_T and particle jet p_T depends strongly on the modelling of the event generators used for the underlying event and multiple parton interactions. Depending on the jet reconstruction algorithm and the physics process this correction has in general to be tailored to a specific analysis.

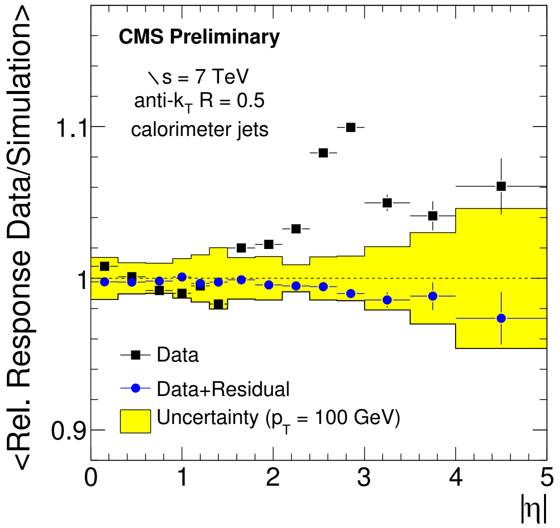

Figure 4.9.: Ratio of the relative response in data and simulations as a function of the pseudorapidity η for L2L3-corrected calorimeter jets; black squares: Data, blue circles: Data with residual correction applied. Taken from [80].

4.3.5. L2L3-Corrections on data and their uncertainties

As of now, the default jet-energy corrections used within the CMS collaboration are the L2L3-corrections. These corrections are derived from simulations and are intended to be applied to the data as well.

However, data-driven techniques are used to validate the absolute and relative jet-energy scale. Such techniques include the γ+jet balance and the Z($\to e^+e^-$ and $\to \mu^+\mu^-$)+jet balancing. These techniques benefit from the superior precision of the electromagnetic calorimeter and the tracker respectively. The calibration using γ+jet-events for p_T-balance and the missing E_T projection fraction method (MPF) is described in [92], the techniques for Z+jet-balance are introduced in [93] and [94]. Current results on the absolute jet-energy scale in data agree within 1 % to simulations and are available in [80].

The validity of the relative jet-energy scale is determined via dijet balance as described in [80] and [95]. The same method is used in Chapter 8 for a validation of the results of the following analysis on data. Here, a residual correction is extracted from this method by evaluating the relative response as a function of η and comparing expectations from simulations and data. In Figure 4.9, the ratio of the relative response in data and in simulations is shown for L2L3-corrected calorimeter jets and with the additional residual correction applied. Simulated data and data agree, if the p_T-independent residual correction is applied.

4.3.6. Kalibri framework

The Kalibri framework [96] has been developed by the University of Hamburg CMS group to facilitate the derivation of parameters for jet-energy corrections and the validation of these corrections. Different correction levels can be derived simultaneously in order to account for correlations between them. This allows for the comparison of the factorised approach applied by CMS with a global calibration approach. For the minimisation, the LVMINI program as described in [97] is used. This program for large scale minimisation uses the limited memory Broyden-Fletcher-Goldfarb-Shanno algorithm, a quasi-Newtonian optimisation method, that allows for an efficient use of memory [98]. It can therefore handle of the order of 10^4 parameters and forms the base of the simultaneous derivation of jet-energy corrections with Kalibri.
In the context of the following analysis, the Kalibri framework has been used for the derivation of parameters within the "Jet Truth Event" class and for studies on data using dijet balance. The "Jet Truth Event" class in Kalibri is specifically designed to avoid the biases mentioned in Section 4.3.1 and facilitates the derivation of correction functions that depend on the measured transverse momentum. For this, the "inversion technique" [84], summarised in the following, has been implemented:
For the known truth t and the measurement m, the expected measurement $\bar{m}$ is related to the response R by:

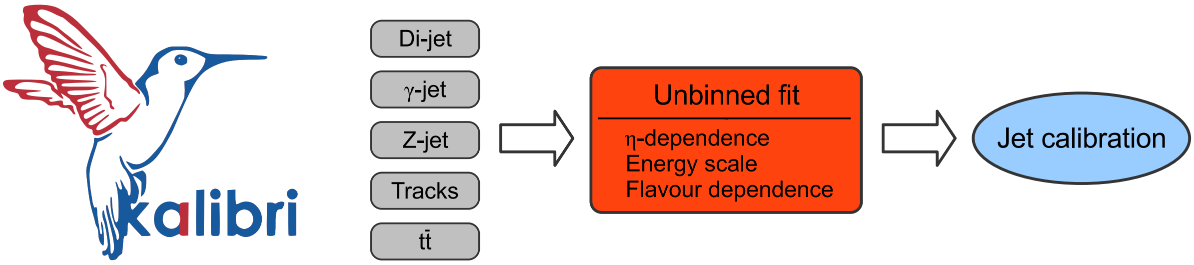

Figure 4.10.: The Kalibri framework can use several different event classes as starting point for the derivation of jet calibrations. [96]

$$\bar{m}(t) = R(t) \cdot t \tag{4.8}$$

The measurement m should be corrected in such a way that the expected value of the corrected measurement $\bar{m}'$ equals the known truth t.

$$\text{Correction } m \rightarrow m' = C_b(m)m \text{ such that } \bar{m}' = t \tag{4.9}$$

where $C_b(m)$ is the correction function with parameters b, depending on the measurement m. For the unbinned fit of the correction function, the expected measurement $\bar{m}$ is unknown. The expected measurement of the event $\bar{m}_i$ is numerically found in each event by solving

$$C_b(\bar{m}_i)\bar{m}_i - t_i = 0 \tag{4.10}$$

Taking these individual expected measurements $\bar{m}_i$, a negative log likelihood using the variation of the expected measurement as estimator can be defined and minimised in order to find optimal values for the parameters b of the correction function:

$$\mathcal{L} = \sum_{i}^{N_{evt}} \left(\ln(\sigma^2(\bar{m}_i)) + \left(\frac{\bar{m}_i - m_i}{\sigma(\bar{m}_i)} \right)^2 \right) \tag{4.11}$$

The Kalibri framework is used in Chapters 6-8 for the determination of correction parameters and their validation.

Chapter 5.

Studies of suitable correction variables

In Chapter 4, the current status of jet-energy corrections at CMS has been discussed. After the application of the required L2L3-corrections to calorimeter jets, a strong dependence of the mean jet response on the jet-flavour is observed as depicted in Figure 5.1(a). The dependence of the jet response on the flavour contributes to the systematic uncertainties of analyses for which the flavour composition is either not well known or different to that given by the simulated QCD data, that is used for the derivation of the jet-energy corrections.

The required (and default) corrections do not exploit any jet properties other than the total transverse momentum and pseudorapidity.

However, the jet-energy response is a complex convolution of many effects such as

- particle distribution, p_T-spectrum, and particle multiplicity in the jets
- magnetic field in the detector
- detector granularity and intrinsic detector response
- noise thresholds applied at the calorimeter cell and the calorimeter tower level

In order to improve the jet-energy calibration, different jet-shape variables and their correlation with the mean jet response are examined in the following using simulated data. This correlation can be corrected for and thereby exploited in order to improve the jet-energy resolution and possibly decrease the flavour dependence observed for calorimeter jets.

The jet-energy resolution of L2L3-corrected simulated calorimeter jets, i.e. before any additional corrections, is shown in Figure 5.1(b). A fit for $30 < p_T^{gen} < 1000$ GeV with the stochastic, noise, and constant terms yields:

$$\left(\frac{\sigma}{\mu}\right)^2 = \left(\frac{N}{p_T^{gen}}\right)^2 + \left(\frac{S}{\sqrt{p_T^{gen}}}\right)^2 + C^2 \tag{5.1}$$

$$\left(\frac{\sigma}{\mu}\right)^2 = \left(\frac{0.8 \pm 0.6\ \mathrm{GeV}}{p_T^{gen}}\right)^2 + \left(\frac{1.214 \pm 0.008}{\sqrt{p_T^{gen}/\,\mathrm{GeV}}}\right)^2 + (0.0328 \pm 0.0008)^2 \tag{5.2}$$

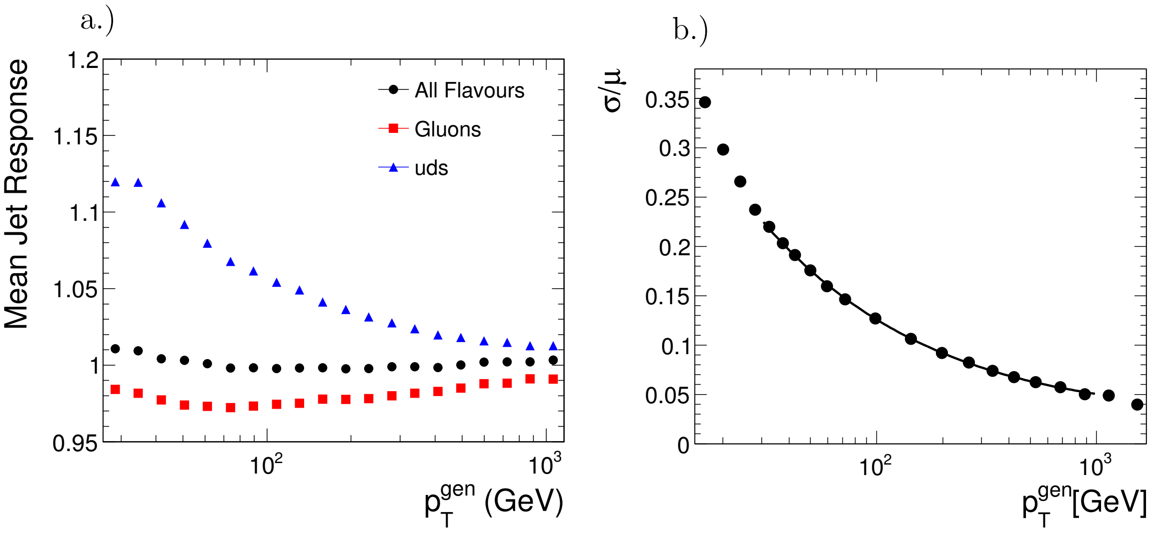

Figure 5.1.: a.) Mean jet response (p_T^{L2L3}/p_T^{gen}) as a function of $p_T^{gen}$for jets with the average QCD flavour composition, gluon jets, and light quark jets after L2L3-correction for calorimeter jets on simulated data generated with PYTHIA.
b.) Relative resolution of L2L3-corrected calorimeter jets as a function of p_T^{gen}.

In this chapter, the candidate variables are introduced and compared with respect to their performance in improving the calibration. For this purpose, about 1 million simulated QCD events[1] used for the derivation of all jet-energy corrections have been analysed with a current CMS software release[2] including a full GEANT 4-based detector simulation. From these events, the two calorimeter jets with the highest $p_T^{gen}$are considered for further analysis. The jet-finding algorithm anti-k_t with a cone size parameter of R=0.5 is used and the flavour of a generator jet is determined as discussed in Section 4.3.4. For the two leading jets, the generator jet is matched to the closest calorimeter jet within a cone of $\Delta R(J_{calo}, J_{gen}) = \sqrt{\Delta\eta^2 + \Delta\varphi^2} < 0.25$. Only the jets that fulfil this criterion are selected and the L2L3-corrections are applied to them. These L2L3-AK5-Calo jets are used for the following analyses. All results are shown for the barrel region ($|\eta| < 1.3$) and binned in p_T^{gen}as discussed in Section 4.3.1 in order to avoid biases, e.g. caused by the energy resolution of the jets and the steeply falling p_{T}-spectrum of the simulated jets.
In sections 5.1-5.3, the variables are introduced and their correlation with the jet response is shown. In Section 5.4, the various variables are compared with respect to the resolution improvement and the flavour dependence of the response using "bin-by-bin" corrections. In Section 5.5, a combination of two of the examined variables is discussed and shown to have an even stronger impact with respect to the resolution improvement and flavour dependence.

---

[1] QCDFlat_Pt15to3000/Spring10-START3X_V26_S09-v1/GEN-SIM-RECO, PYTHIA
[2] CMSSW_3_6_0

5.1. Electromagnetic fraction (EMF)

The electromagnetic fraction, EMF, is defined as

$$\mathrm{EMF}_{jet} = \frac{E_{ECAL}}{E_{ECAL} + E_{HCAL}}, \tag{5.3}$$

i.e. the fraction of energy measured in the electromagnetic calorimeter and the total energy, measured in both calorimeters. Until recently, a correction based on the EMF was considered to be the first "optional" correction within the factorised jet-energy corrections approach of CMS.

In Figure 5.2(a), the distribution of the EMF is shown in two p_T^{gen}-ranges. The distribution approaches a Gaussian for high p_T^{gen}. For low p_T^{gen}, a significant fraction of the jets have energy measured exclusively in the ECAL, leading to EMF = 1.

In Figure 5.3(a), the energy measured in the HCAL is plotted against the energy measured in the ECAL. It is observed that the core of the distribution is biased towards small values of E_{HCAL}. For very low p_{T}, this leads to many jets with EMF = 1.

This is linked to the fact that a large fraction of the constituents of the jets, low-p_{T} charged particles, are bent drastically by the strong magnetic field of 3.8 T of the solenoid magnet. Together with the offline reconstruction thresholds for the HCAL of 0.7 GeV in the barrel region (current readout thresholds available in [75], established in [99]) this often leads to a small fraction of energy deposited in the HCAL and a large EMF.

In Figure 5.3(b), the measured energies in ECAL and HCAL are shown for individual towers. The threshold of 0.2 GeV for ECAL-towers in the barrel and of 0.7 GeV for HCAL-towers can clearly be seen.

As the calorimeters of CMS are non-compensating ($e/h \neq 1$ and different for ECAL and HCAL, see Section 2.3 and [100]) and the electromagnetic fraction is strongly correlated with the e/h-ratio and the fraction of energy carried by electrons and photons [86], the electromagnetic fraction is expected to show a correlation with the mean response of jets. Indeed it is observed in Figure 5.2(b) that the response is overestimated for jets with a very high or a very low electromagnetic fraction. For jets with a high EMF, this behaviour is linked directly to the non-compensating calorimeters: If the energy deposits are mainly due to electrons and photons, the average L2L3-correction still corrects for the low response of the expected hadronic fraction, resulting in the afore mentioned overestimation. For low values of EMF it can be deduced that the energy available from hadrons for deposition in the HCAL is higher and therefore also the response of the HCAL is increased (see [101] for results concerning the single particle response on data).

In Figure 5.2(c), the relative flavour composition is shown in bins of EMF. It is observed that the fraction of light quark jets is higher in the tails of the EMF distribution, leading to a higher response. A possible explanation is that the particle multiplicity of light quark induced jets is lower than that of gluon jets, leading to a higher fluctuation in the determination of the measured EMF. Whether this correlation both with the response and the flavour can be exploited to decrease the flavour dependence of the jet response is evaluated in Section 5.4.

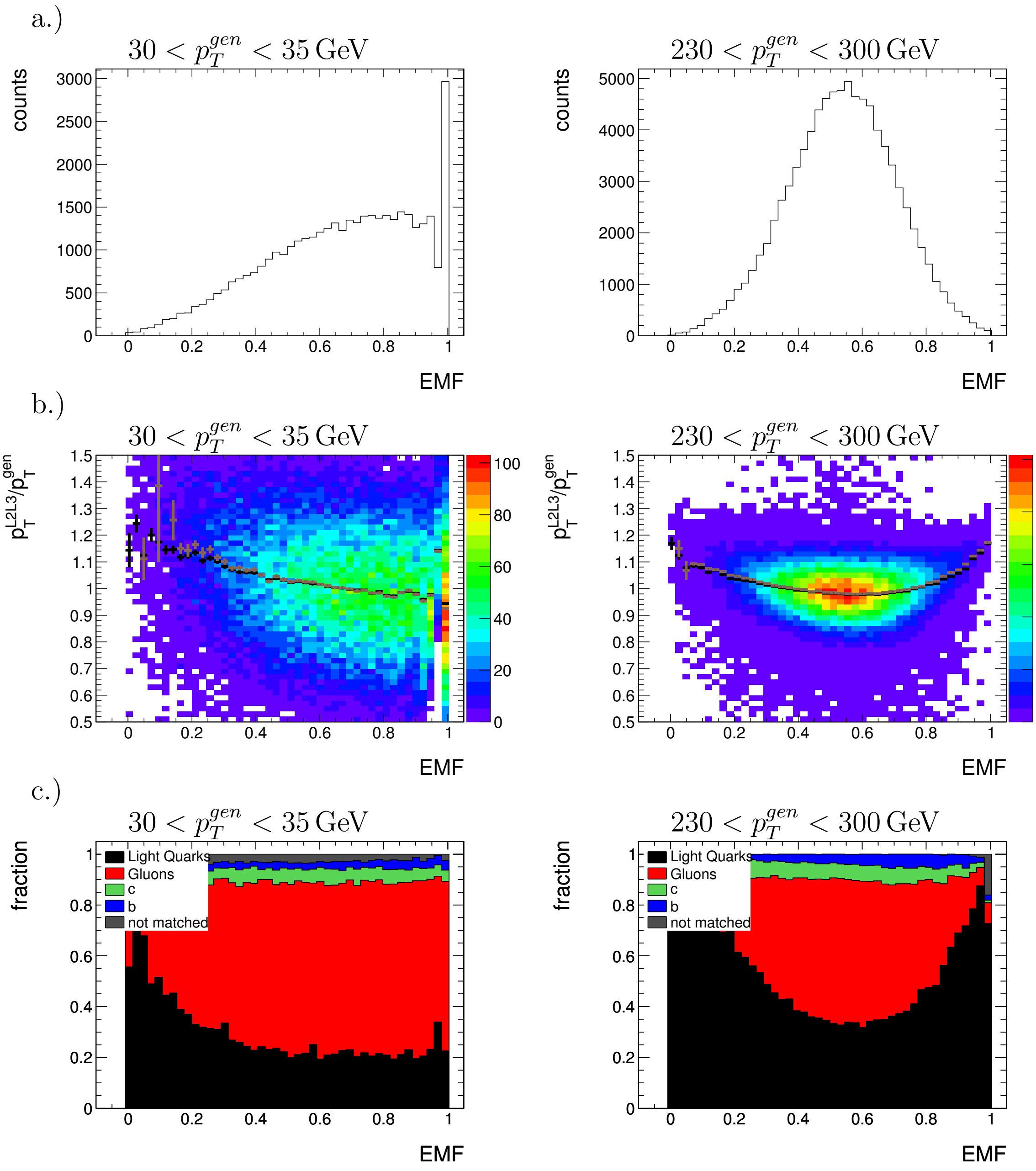

Figure 5.2.: a.) Distribution of the electromagnetic fraction EMF in two p_T^{gen}-ranges. For low p_{T}, a significant amount of jets has an EMF of 1.
b.) Correlation of the response R_{L2L3} and the electromagnetic fraction EMF; coloured z-scale: counts; black: mean response in bins of EMF; brown: mean of a Gaussian fit of the response in bins of EMF.
c.) Relative flavour composition in bins of EMF in two p_T^{gen}-ranges.

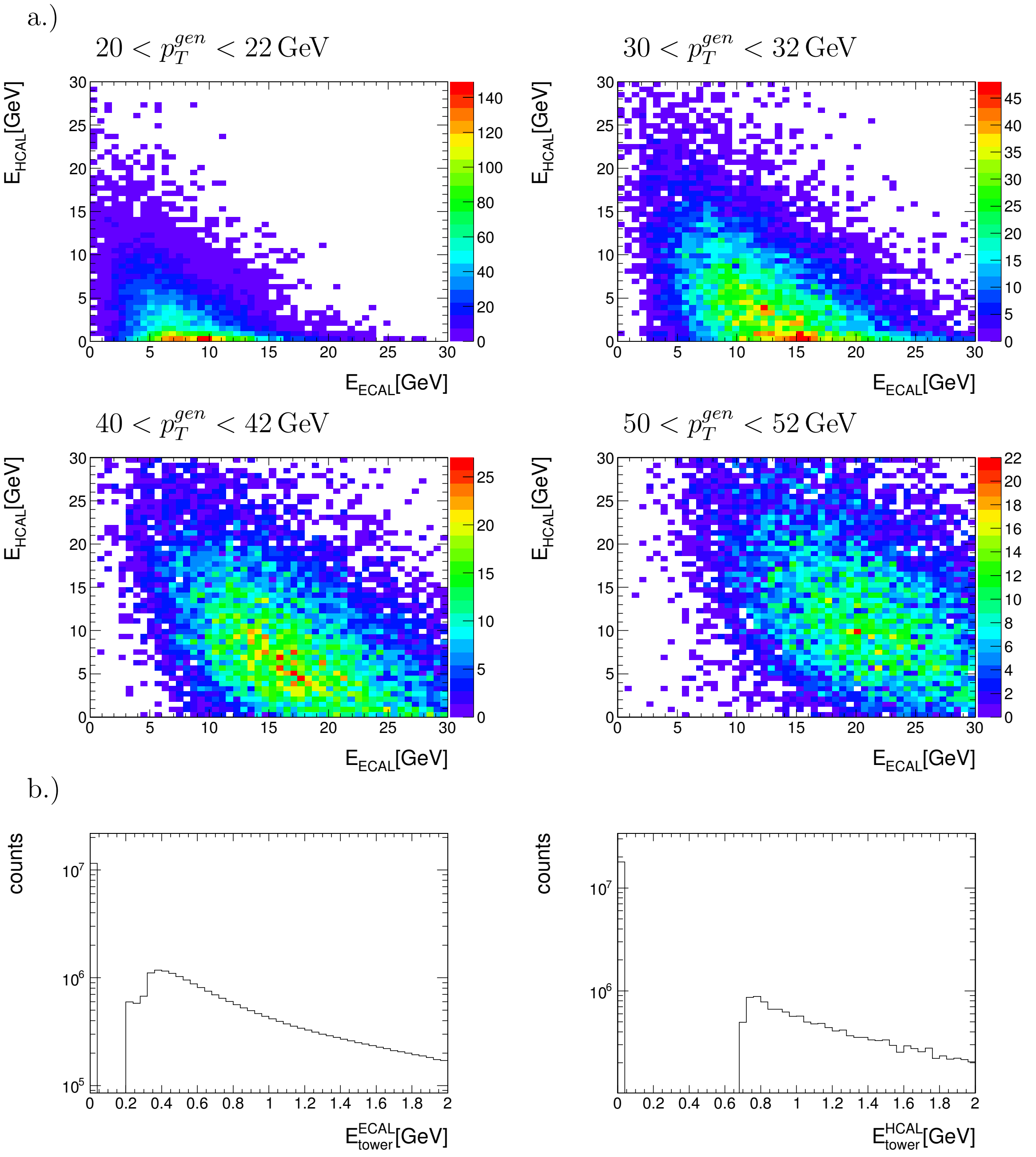

Figure 5.3.: a.) Correlation of energy depositions in the electromagnetic calorimeter and in the hadronic calorimeter for the two jets with the highest p_T^{gen} in the barrel region in ranges of p_T^{gen}.
b.) Energy deposits in individual ECAL-towers and HCAL-towers in the barrel region, readout thresholds are visible.

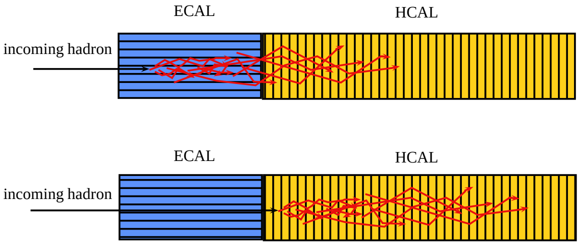

Figure 5.4.: Sketch of early and late showering hadrons. Due to the non-compensating calorimeters of CMS, a different response is observed for early and late showering hadrons (for pions see [102]).

5.2. Tower-based EMF

The electromagnetic fraction is calculated from the sum of all energies in ECAL and HCAL calorimeter towers in a jet. It will be studied in the following, whether it is beneficial to consider more sophisticated variables that take into account differing energy distributions on ECAL and HCAL cells on the calorimeter tower level.

Previous studies have shown that for early and late showering hadrons, a dependence of the particle response is observed (see Figure 5.4). The $\mathrm{EMF}_{\mathrm{tower}}$ can be regarded as an indicator for early and late showering hadrons.

In Figure 5.5, the correlation of the $\mathrm{EMF}_{\mathrm{tower}}$ and $\frac{E_{tower}}{E_{jet}}$ is depicted. Distinct populations are observed and the energy measured on the tower level can be divided into three classes: towers with energy measured in the ECAL only (1), in the HCAL only (2), and energy measured in both calorimeters (3).

Three global variables from calorimeter tower information can be defined following this approach:

$$(1)\quad E_{rel}^{\mathrm{EMF}_{tow}=0} = \frac{\sum_i^{\mathrm{EMF}=0} E_{tower}^i}{E_{jet,raw}}$$

$$(2)\quad E_{rel}^{\mathrm{EMF}_{tow}=1} = \frac{\sum_i^{\mathrm{EMF}=1} E_{tower}^i}{E_{jet,raw}}$$

$$(3)\quad E_{rel}^{\mathrm{EMF}_{tow}=0\cdots 1} = \frac{\sum_i^{\mathrm{EMF}=0\cdots 1} E_{tower}^i}{E_{jet,raw}}$$

These variables encode the information on how the energy is distributed on the three different tower classes for each jet as a whole. The value of each variable stands for the fraction of jet energy deposited in towers of each class. For example, $E_{rel}^{\mathrm{EMF}_{tow}=0}$ denotes the fraction of the total jet energy deposited in towers with $\mathrm{EMF} = 0$. In the following, the correlation of the L2L3-corrected response and these variables is discussed.

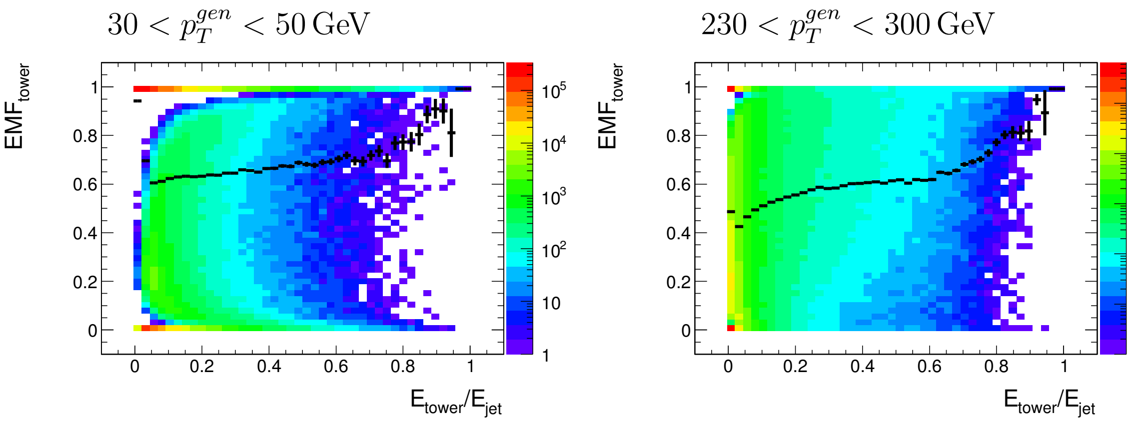

Figure 5.5.: The Tower-EMF $\mathrm{EMF}_{\mathrm{tower}}$ as a function of the ratio of the tower energy and the total jet energy $\frac{E_{tower}}{E_{jet}}$ in the barrel region in bins of p_T^{gen}, logarithmic z-scale; black: mean response in bins of E_{tower}/E_{jet}

5.2.1. $E_{rel}^{\mathrm{EMF}_{tow}=0}$

An electromagnetic fraction equal to zero means that an energy deposition has only been measured in the hadronic calorimeter. Owing to the high density of the ECAL-crystals, photons and electrons are expected to shower in the ECAL completely. Hadronic showers are primarily expected in the HCAL and only start to a certain extent (order of 1/3) in the ECAL already. These hadronic particles, leakage of energy from neighbouring calorimeter towers, and HCAL-noise as discussed in [103], can contribute to energy depositions measured only in the hadronic calorimeter. In the crowded environment of high-energetic jets, it is expected to be unlikely that such towers carry a big fraction of the total jet energy. For low energies, the energy deposition in single towers becomes more important and the noise of the HCAL hybrid photo diodes can become very relevant for the measurement. In Figure 5.6(a), the distribution of $E_{rel}^{\mathrm{EMF}_{tow}=0}$ is illustrated. For low-energy jets, it is observed that a lot of jets do not contain towers with $E_{rel}^{\mathrm{EMF}_{tow}=0}$ deposition at all. However, jets with such towers can contain a significant fraction of their energy in such towers due to the small number of hit towers. For higher p_{T}, the distribution becomes much narrower and peaks at low relative contributions to the jet energy. Looking at the correlation with the response (see Figure 5.6(b)) only a very weak dependence is observed. For high-energetic jets, that do not contain towers with EMF=0, the p_{T} is slightly overestimated after the L2L3-corrections.

5.2.2. $E_{rel}^{\mathrm{EMF}_{tow}=0\cdots1}$

For simultaneous energy depositions in both calorimeters, the variable $E_{rel}^{\mathrm{EMF}_{tow}=0\cdots1}$ has been defined. As shown in Figure 5.7(a), the energy deposits of high-energy jets are almost exclusively in towers in which both, the measured energies in the ECAL and HCAL, were above readout thresholds. For low energies, a large fraction of energy is

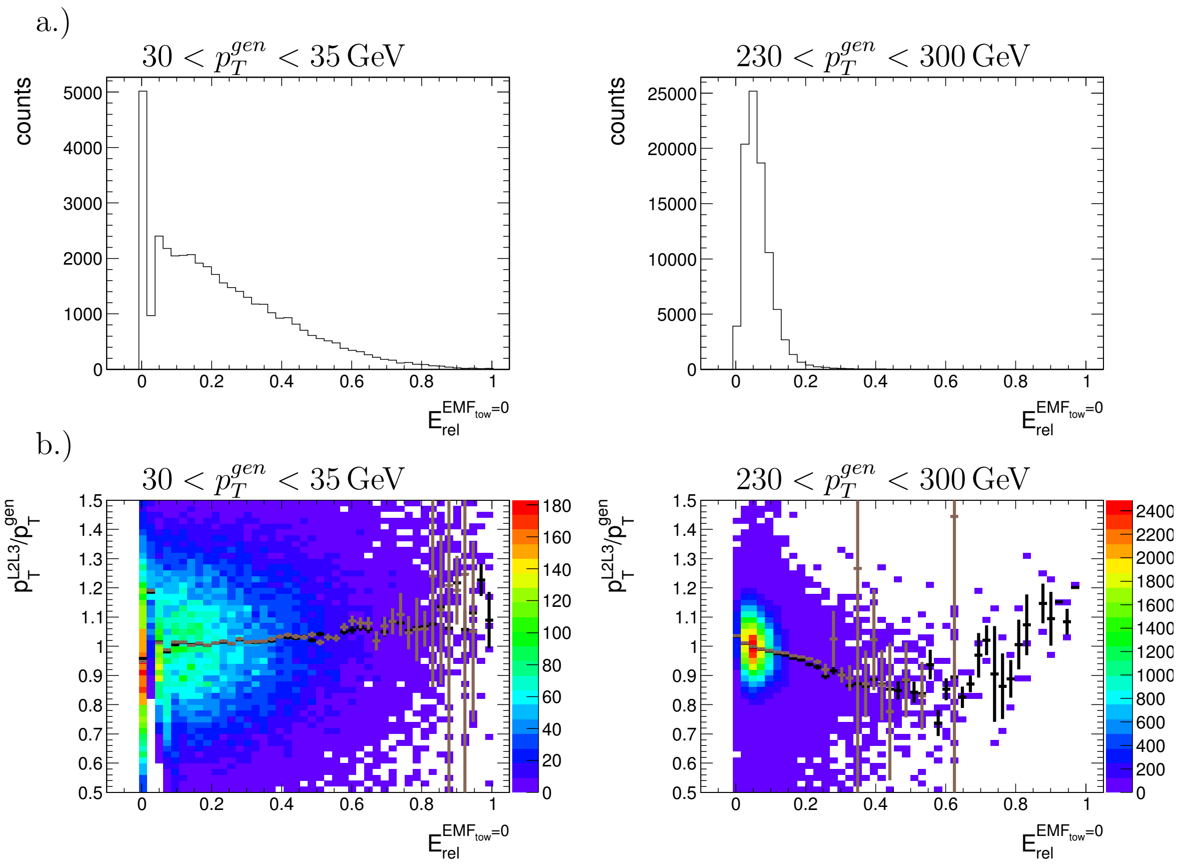

Figure 5.6.: a.) Distribution of $E_{rel}^{\mathrm{EMF}_{tow}=0}$ in two p_T^{gen}-ranges.
b.) Correlation of the response R_{L2L3} and $E_{rel}^{\mathrm{EMF}_{tow}=0}$; coloured z-scale: counts; black: mean response in bins of $E_{rel}^{\mathrm{EMF}_{tow}=0}$; brown: mean of a Gaussian fit of the response in bins of $E_{rel}^{\mathrm{EMF}_{tow}=0}$.

measured in pure ECAL or HCAL towers. Considering the correlation with the response in Figure 5.7(b), it is observed that a slight dependence on $E_{rel}^{\mathrm{EMF}_{tow}=0\cdots1}$ exists for high p_T and high values of $E_{rel}^{\mathrm{EMF}_{tow}=0\cdots1}$.

5.2.3. $E_{rel}^{\mathrm{EMF}_{tow}=1}$

The electromagnetic calorimeter of CMS has a very good energy resolution as has been discussed in Section 3.4. In the case that a large amount of energy of the jet is deposited in ECAL-only towers, the measurement of the jet energy should profit from this resolution. The variable $E_{rel}^{\mathrm{EMF}_{tow}=1}$ is used to describe the jet energy fraction measured in such towers. For low energies, the distribution of the variable (see Figure 5.8(a)) is very broad as statistical fluctuations are high due to the low number of hit towers. For high transverse momenta, the distribution becomes narrow and peaks at low values as only very few towers are hit by single particles in the highly collimated jet. In Figure 5.8(b), the correlation of the response and $E_{rel}^{\mathrm{EMF}_{tow}=1}$ is depicted. For low and high values of

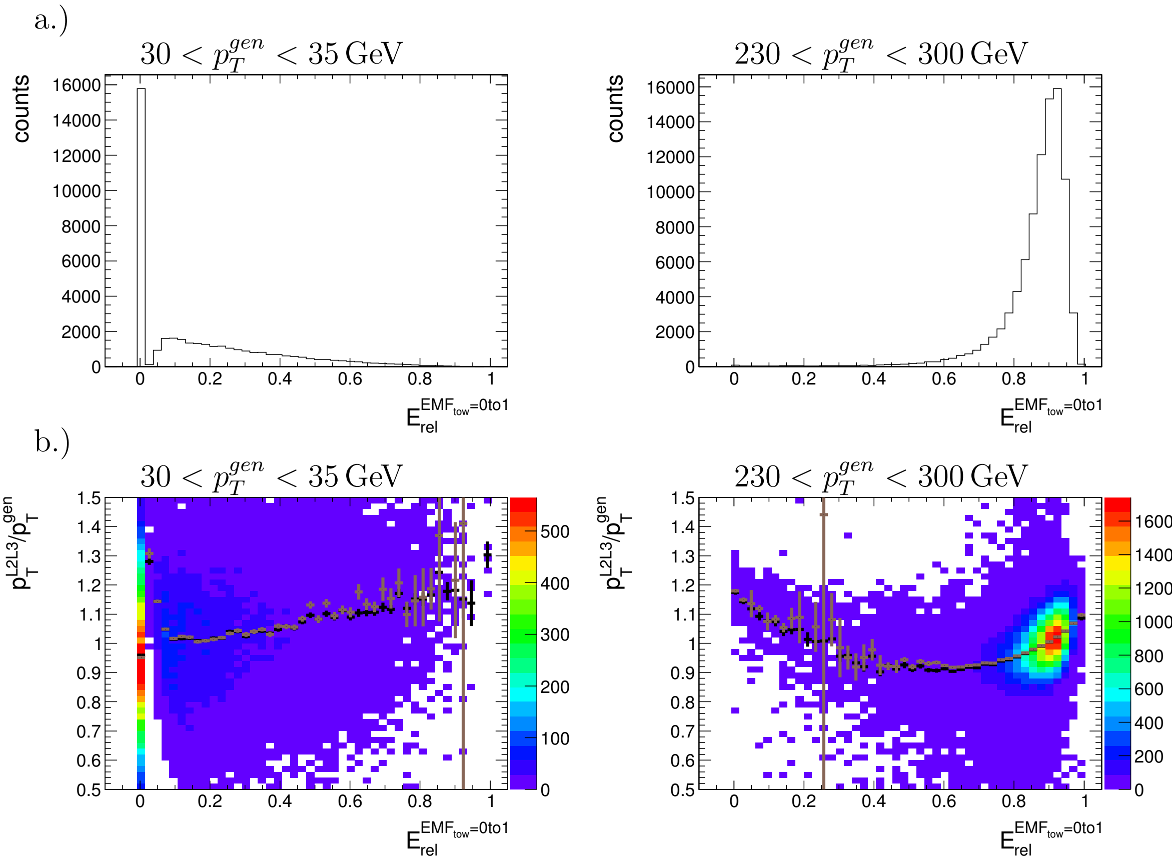

Figure 5.7.: a.) Distribution of $E_{rel}^{\mathrm{EMF}_{tow}=0\cdots1}$ in two p_T^{gen}-ranges.
b.) Correlation of the response R_{L2L3} and $E_{rel}^{\mathrm{EMF}_{tow}=0\cdots1}$; coloured z-scale: counts; black: mean response in bins of $E_{rel}^{\mathrm{EMF}_{tow}=0\cdots1}$; brown: mean of a Gaussian fit of the response in bins of $E_{rel}^{\mathrm{EMF}_{tow}=0\cdots1}$.

the $E_{rel}^{\mathrm{EMF}_{tow}=1}$ distribution, the response is slightly overestimated, which is very similar to the behaviour of the global jet EMF.

5.2.4. Radial distribution of energy and EMF$_{\mathrm{tower}}$

The correlation of the three previously defined variables with the response has been discussed above. No strong correlation has been observed. In order to extend these studies, it could be useful to additionally examine the radial distribution of the energy deposition and the radial dependence of the distribution on the different tower classes, because only charged particles are bent by the magnetic field. This is shown in Figure 5.9. In Figure 5.9(a) the radial distribution of the energy deposition in jets is depicted. The jet area has been split up into annuli of width 0.1 in ΔR between the towers and the jet

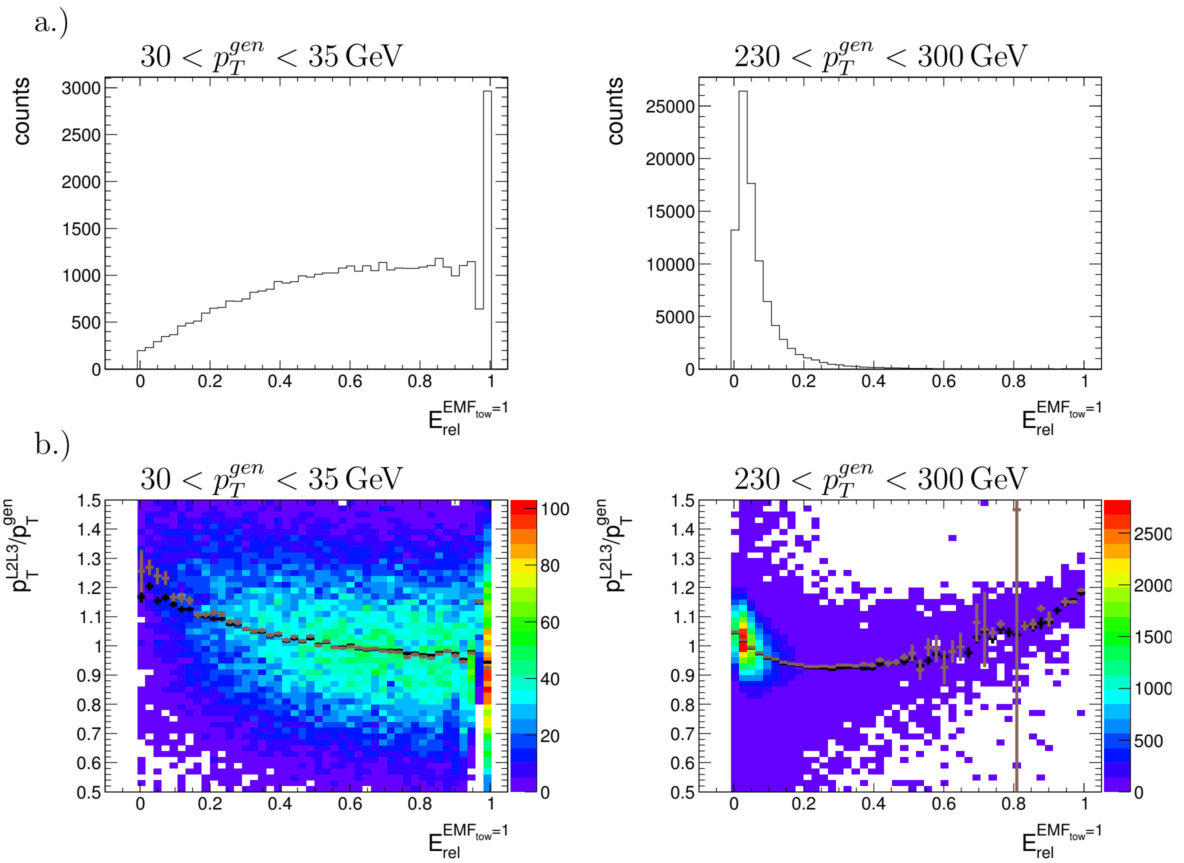

Figure 5.8.: a.) Distribution of $E_{rel}^{\mathrm{EMF}_{tow}=1}$ in two p_T^{gen}-ranges.
b.) Correlation of the response R_{L2L3} and $E_{rel}^{\mathrm{EMF}_{tow}=1}$; coloured z-scale: counts; black: mean response in bins of $E_{rel}^{\mathrm{EMF}_{tow}=1}$; brown: mean of a Gaussian fit of the response in bins of $E_{rel}^{\mathrm{EMF}_{tow}=1}$.

axis. The energy distribution in these annuli is shown as

$$E_{rel,\Delta R} = \frac{E_{\mathrm{annulus}}}{E_{jet}} \tag{5.4}$$

It can be seen clearly that the biggest fraction of the total jet energy is highly collimated for high p_{T}-jets and only a fraction of approximately 5-10% is deposited in the 0.2 to 0.3 annulus. For low p_{T}-jets the energy deposition is, on average, much broader, resulting in an average energy fraction of 15-20% in the 0.2 to 0.3 annulus. This is linked to the jet constituents' p_{T}-spectrum, which is much harder for high p_{T}-jets, resulting in a weaker deflection by the magnetic field. Soft gluons are radiated under very small angles with respect to the initial parton's direction of flight and all produced particles are strongly boosted.

Figures 5.9(b)-(d) show the energy distribution in each of the annuli in towers of the appropriate class. These values are normalised to the total energy deposition in the

a.)

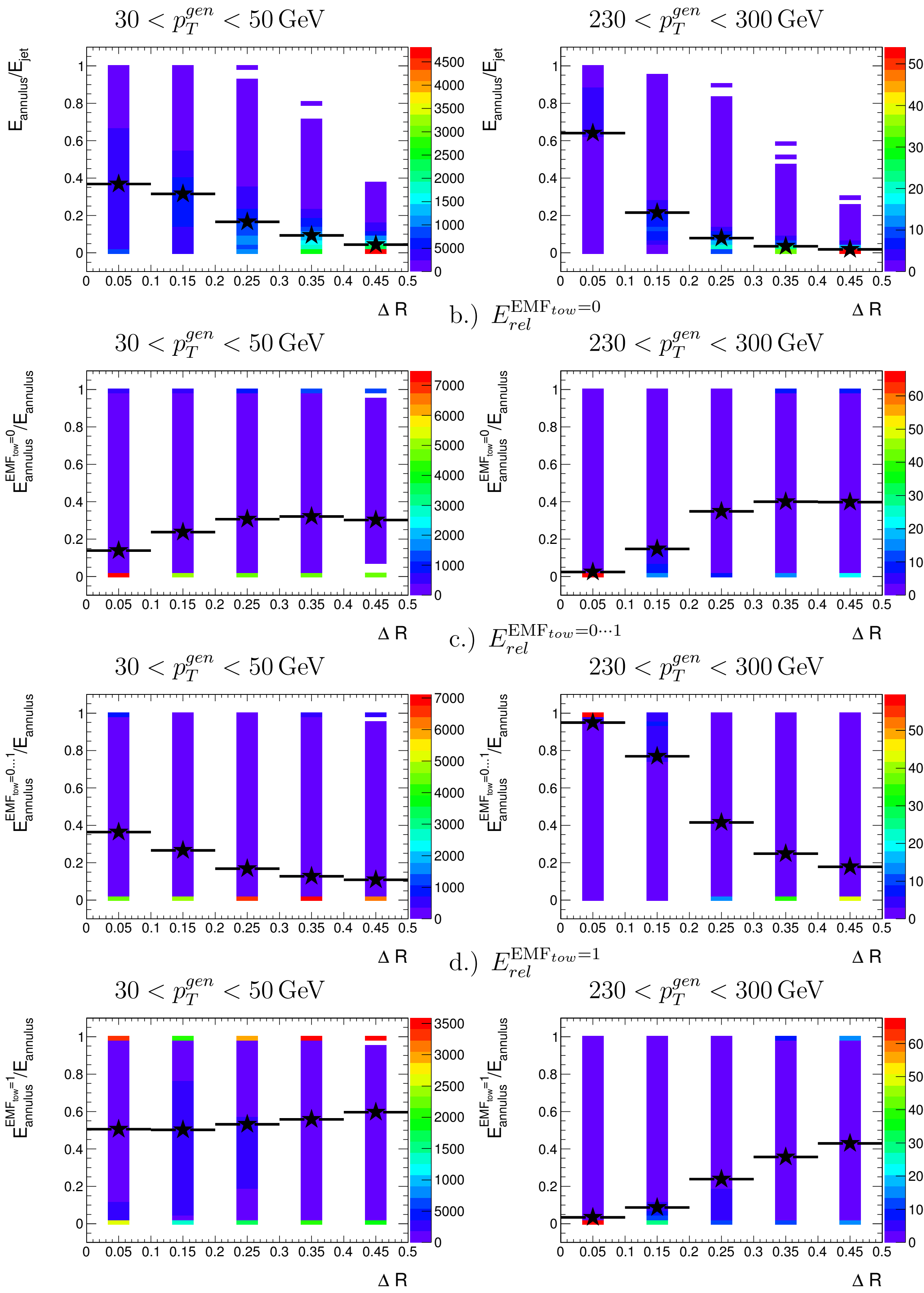

b.) $E_{rel}^{\mathrm{EMF}_{tow}=0}$

c.) $E_{rel}^{\mathrm{EMF}_{tow}=0\cdots1}$

d.) $E_{rel}^{\mathrm{EMF}_{tow}=1}$

Figure 5.9.: a.) Relative energy deposition in annuli of width 0.1 in ΔR ($E_{rel,\Delta R}$) as a function of ΔR; black: mean value
b, c, d.): $E_{rel,\Delta R}^{\mathrm{EMF}=0,1,\,\mathrm{or}\,0\cdots1}$ for the three different kinds of towers (EMF $=0$, EMF $=1$, or $0<$ EMF <1) for the annuli mentioned before, i.e. the distribution of the energy deposition on the three classes in each annulus. (black: mean value)

corresponding annulus according to

$$E_{rel,\Delta R}^{\text{EMF}=0,1,\,\text{or}0\cdots 1} = \frac{E_{\text{annulus}}^{\text{EMF}=0,1,\,\text{or}0\cdots 1}}{E_{\text{annulus}}} \tag{5.5}$$

It is observed that while $\approx 50\%$ of the energy is deposited in towers with $\text{EMF}_{\text{tower}} = 1$ for low p_{T}-jets in all annuli, the other two classes carry a lower fraction of the energy. However, as the central region of a jet carries the largest fraction of the energy, even for low p_{T} jets, the towers with $0 < \text{EMF}_{\text{tower}} < 1$ carry a significant fraction of the energy. For high p_{T}-jets, the energy deposition is concentrated in the mixed ($0 < \text{EMF}_{\text{tower}} < 1$) towers in the central region of the jet. In the peripheral regions of the jets, a significant fraction of the towers has an EMF equal to 0 or 1, but this corresponds only to a very low fraction of the total jet energy according to Figure 5.9(a).
Due to the steeply falling relative energy deposition as a function of ΔR it is difficult to extract more information from the EMF in inner and outer regions. Instead, it will be studied in the following, whether it is useful to examine jet-shape variables that define a jet width directly.

5.3. Jet-width variables

Jet-width variables are very interesting with respect to a further jet-energy correction in addition to the L2L3-corrections. The previous study of Björn Kolodzey [104] on the flavour dependence of jet-energy corrections at CMS has shown that the $\sigma_{\varphi\varphi}$-moment (see below for definition) is sensitive to the flavour of a jet and that a dependence of the mean jet response on the $\sigma_{\varphi\varphi}$-moment is observed. These effects are linked to the charged particle multiplicity and p_{T}-spectrum of the constituents, which is different for gluon and light quark induced jets (see Section 2.2.2). Due to the non-linear response of the CMS calorimeters, a different particle multiplicity and p_{T}-spectrum of the constituents contribute to the different jet response observed for calorimeter jets of different flavour (see Figure 5.1).
The second central moments of the energy-weighted tower distributions $\sigma_{\eta\eta}$ and $\sigma_{\varphi\varphi}$ are calculated as the variance of the energy-weighted calorimeter tower positions with respect to the jet axis:

- $\sigma_{\varphi\varphi} = \sqrt{\frac{\sum p^i_{T,\text{Calo}} \cdot (\varphi_i - \varphi_{\text{Calo-Jet}})^2}{\sum p^i_{T,\text{Calo}}}}$, where $\varphi_{\text{Calo-Jet}} = \frac{\sum p^i_{T,\text{Calo}} \cdot \varphi^i}{\sum p^i_{T,\text{Calo}}}$
- $\sigma_{\eta\eta} = \sqrt{\frac{\sum p^i_{T,\text{Calo}} \cdot (\eta_i - \eta_{\text{Calo-Jet}})^2}{\sum p^i_{T,\text{Calo}}}}$, where $\eta_{\text{Calo-Jet}} = \frac{\sum p^i_{T,\text{Calo}} \cdot \eta^i}{\sum p^i_{T,\text{Calo}}}$

It is expected (and observed) that the mean value of the width in φ is higher than in η. This is due to the magnetic field, which is parallel to the beam line (see Section 3.3), such that the Lorentz Force acts in the transverse plane.

5.3.1. $\sigma_{\varphi\varphi}$-moment

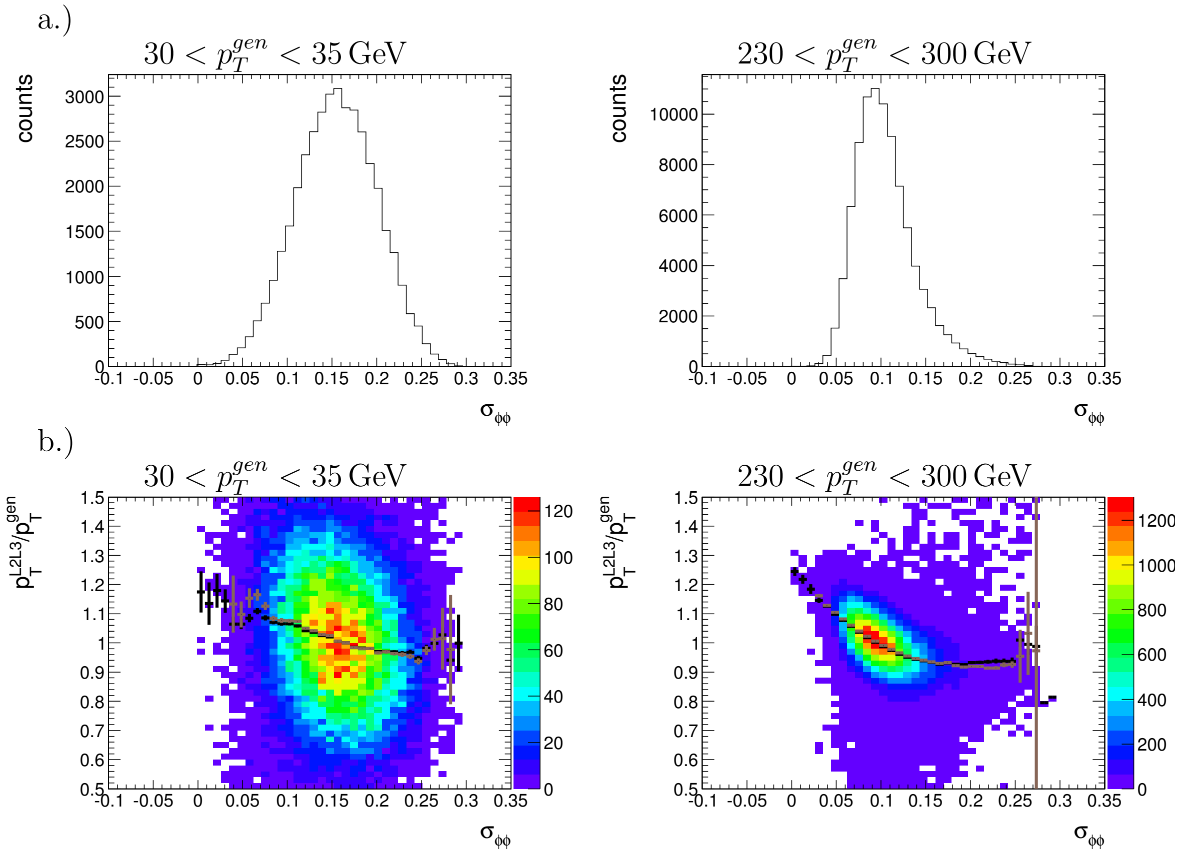

Figure 5.10.: a.) Distribution of the $\sigma_{\varphi\varphi}$-moment in two p_T^{gen}-ranges.
b.) Correlation of the response R_{L2L3} and the $\sigma_{\varphi\varphi}$-moment; coloured z-scale: counts; black: mean response in bins of $\sigma_{\varphi\varphi}$-moment; brown: mean of a Gaussian fit of the response in bins of $\sigma_{\varphi\varphi}$-moment.

In Figure 5.10(a), the distribution of the $\sigma_{\varphi\varphi}$-moment is shown for two p_T^{gen}-bins. The jets become narrower in φ for higher p_T. The distribution is continuous without any peaks in the tails. Looking at the correlation of $\sigma_{\varphi\varphi}$ with the response, a clear dependence is observed in Figure 5.10(b). The slope is very prominent in the highly populated regions around the mean value of the $\sigma_{\varphi\varphi}$-moment as well.

5.3.2. $\sigma_{\eta\eta}$-moment

The distribution of the $\sigma_{\eta\eta}$-moment is very similar to the distribution of the $\sigma_{\varphi\varphi}$-moment discussed above, but as can be seen in Figure 5.11(a), the most probable value and the mean of the distribution are shifted towards slightly lower values and for high p_T, the peak is slightly narrower in comparison. In Figure 5.11(b), the correlation of the width in η with the response is very similar to the dependence observed for the $\sigma_{\varphi\varphi}$-moment. For both variables, $\sigma_{\varphi\varphi}$ and $\sigma_{\eta\eta}$, a strong correlation with the jet-energy response is observed.

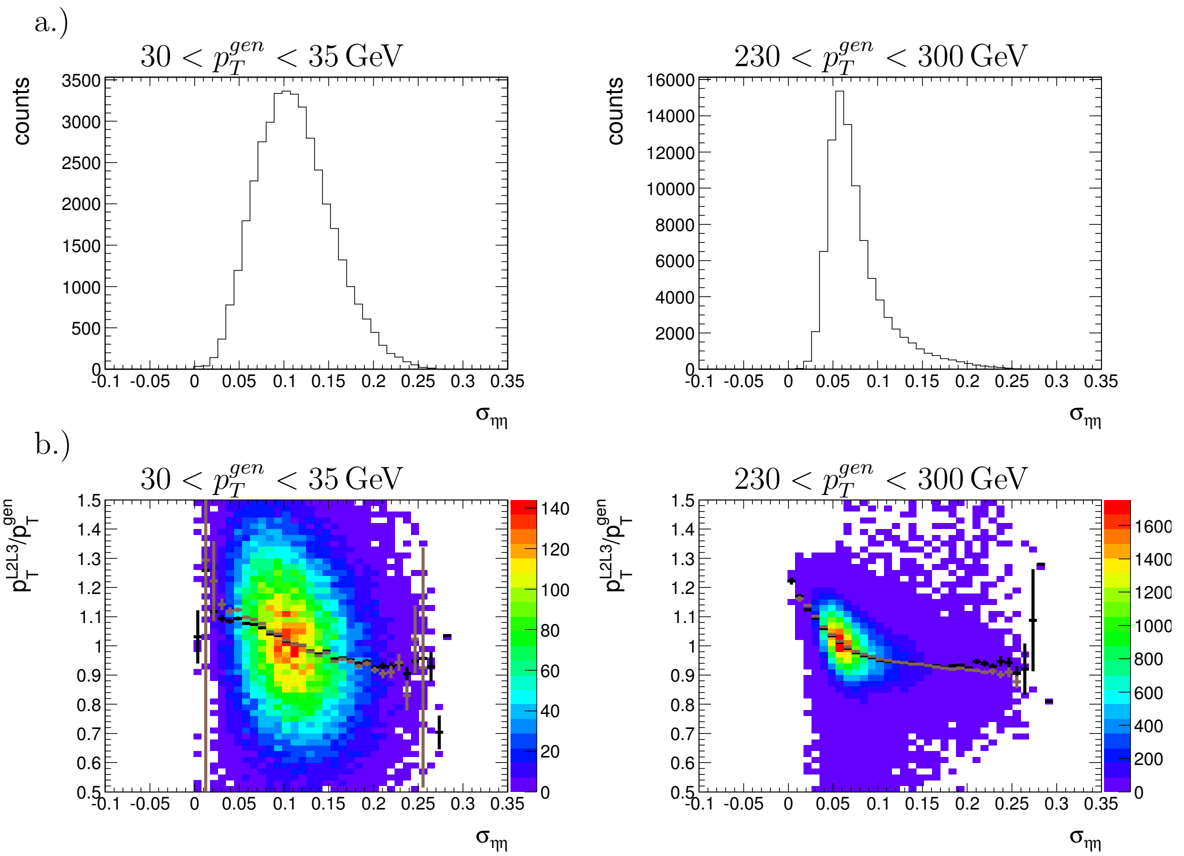

Figure 5.11.: a.) Distribution of the $\sigma_{\eta\eta}$-moment in two p_T^{gen}-ranges.
b.) Correlation of the response R_{L2L3} and the $\sigma_{\eta\eta}$-moment; coloured z-scale: counts; black: mean response in bins of $\sigma_{\eta\eta}$-moment; brown: mean of a Gaussian fit of the response in bins of $\sigma_{\eta\eta}$-moment.

5.4. Performance comparison of observables

To identify the best observables, a performance comparison of the different potential correction variables is done using simplistic “bin-by-bin corrections”. A more sophisticated method will be derived in Chapter 6 for the best observable. The “bin-by-bin-corrections“ can be described in the following steps:

- The correlation of the response after L2L3 correction (R_{L2L3}) and a variable $x_{correction}$ is obtained by looping over all available events and determining the mean value of R_{L2L3} vs. $x_{correction}$ in ranges of p_T^{gen}(see Figure 5.12)
- The inverse of $\langle R_{L2L3} \rangle$ is applied as a correction factor

$$\mathrm{CF} = \frac{1}{\langle R_{L2L3} \rangle (p_T^{gen}, x_{correction})} \tag{5.6}$$

- The corrected response is plotted and evaluated.

The core of the corrected response is fitted via an iterative Gaussian fit (see Figure 5.21 for an example): The first fit is performed over the full range, the second fit has the range set to $[\mu - 1.5\sigma, \mu + 1.5\sigma]$ with the Gaussian mean value μ and the Gaussian width σ. The mean value, μ, and width, σ, of the fitted Gaussian are taken as a measure for the jet-p_{T} response and resolution after the correction, respectively. In Figure 5.12(b), the relative p_{T}-resolution as a function of $p_T^{gen}$is shown. For future comparisons, a presentation is used in which the relative resolution is scaled to the relative resolution of L2L3-corrected calorimeter jets.

In order to determine the effect on the flavour dependence, that was shown in Figure 5.1(a), the Gaussian mean of the response is determined separately for a pure light quark sample and a pure gluon sample. The difference of these mean responses, $\mathrm{R_{uds}} - \mathrm{R_{gluon}}$, is taken as a measure for the flavour dependence.

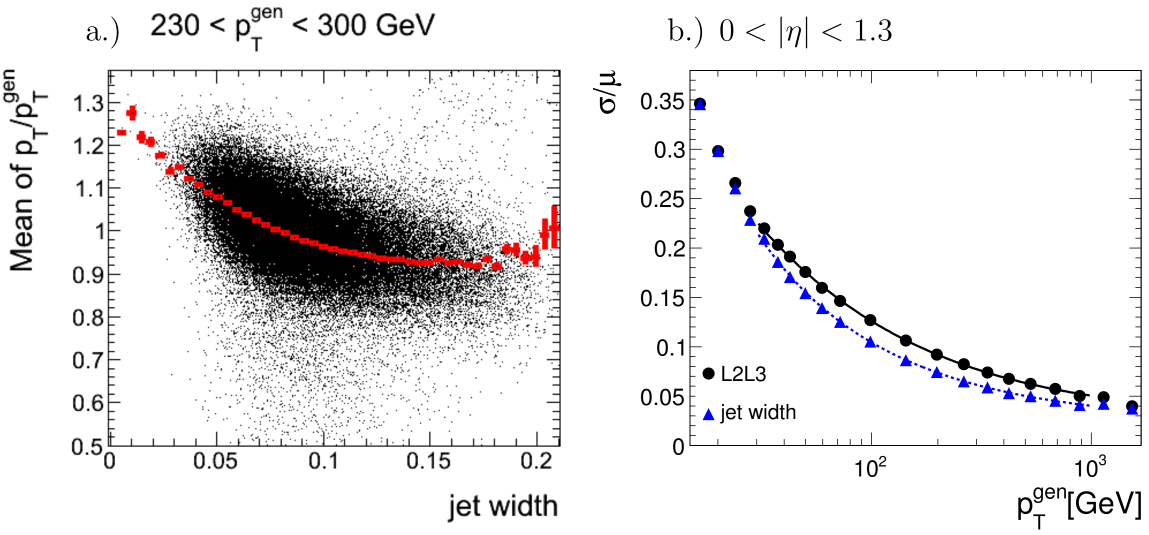

Figure 5.12.: a.) Scatter plot of $JW = \frac{\sigma_{\varphi\varphi} + \sigma_{\eta\eta}}{2}$ and response R_{L2L3} for $230 < p_T^{gen} < 300$ GeV in the barrel region with the mean of R_{L2L3} in bins of the jet width (JW) as an overlay (profile).
b.) Relative p_{T}-resolution of jets in the barrel region as a function of p_T^{gen}.

5.4.1. EMF and tower-based EMF

In Figure 5.13, the EMF variable and the tower-based EMF-variables are shown in comparison. In the upper plot on the left-hand side, the resolution improvement is shown as a function of p_T^{gen}in the previously described manner, in that the relative resolution is scaled to the L2L3-corrected relative resolution. On the right hand side, the difference of the mean jet response for light quark jets and gluon jets is shown.

In contrast to the comparisons for all other variables shown in the following, the qualitative results depend in this case on the choice of the binning-variable for the bin-by-bin corrections. The performance of the tower variables is artificially enhanced, when the

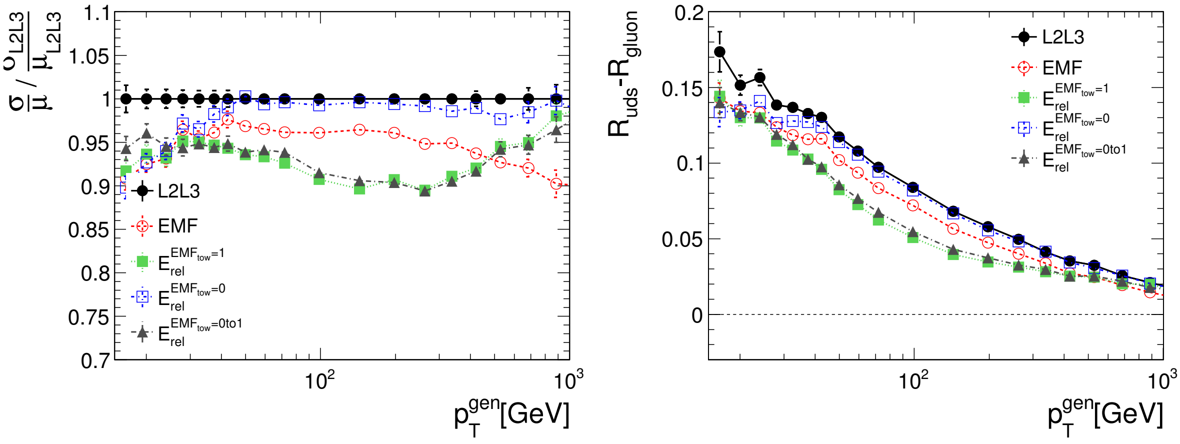
a.) resolution improvement, p_T^{gen}

b.) flavour difference, p_T^{gen}

c.) resolution improvement, p_T^{L2L3}

d.) flavour difference, p_T^{L2L3}

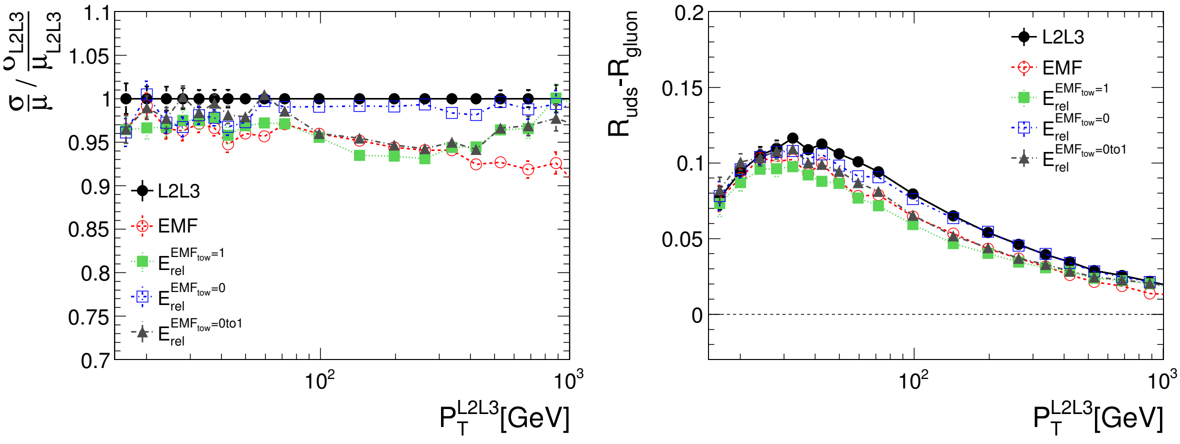

Figure 5.13.: EMF-based corrections:
a.) Relative resolution after subsequent "bin-by-bin corrections" scaled to the relative resolution after L2L3-correction as a function of p_T^{gen}.
b.) Difference of the mean responses determined separately from a Gaussian fit for a pure light quark and a pure gluon sample.
c.) and d.) same as a.) and b.), but all procedures carried out with a binning in p_T^{L2L3}:
$CF = 1/(\langle R_{L2L3}\rangle(p_T^{L2L3}, x_{correction}))$
red open circle: EMF; green solid square: $E_{rel}^{\mathrm{EMF}_{tow}=1}$; blue open square: $E_{rel}^{\mathrm{EMF}_{tow}=0}$; grey solid triangle: $E_{rel}^{\mathrm{EMF}_{tow}=0\cdots1}$

procedure is carried out with a binning in p_T^{gen}. In the lower two plots, the results for a bin-by-bin correction in p_T^{L2L3} are shown. This binning does not prevent biases as mentioned in Section 4.3.1, but is more comparable to the situation in the experiment (where no "truth information" from simulations is available). In this case, most variables using the electromagnetic fraction show a similar performance in improving the jet-energy resolution by about 5 % and reducing the flavour dependence by ≈ 25 % at $p_T^{L2L3} = 100$ GeV. Only the $E_{rel}^{\mathrm{EMF}_{tow}=0}$-variable does not show any significant improvement. $E_{rel}^{\mathrm{EMF}_{tow}=1}$ and

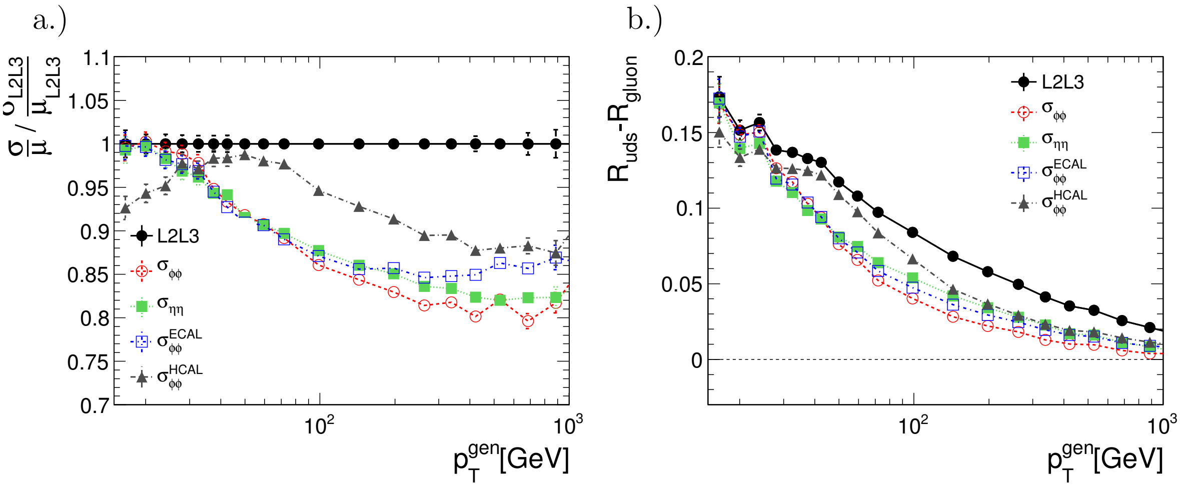

Figure 5.14.: Jet-width corrections:
a.) Relative resolution after subsequent “bin-by-bin corrections” scaled to the relative resolution after L2L3-correction.
b.) Difference of the mean responses determined separately from a Gaussian fit for a pure light quark and a pure gluon sample.
red open circle: $\sigma_{\varphi\varphi}$-moment; green solid square: $\sigma_{\eta\eta}$-moment; blue open square: $\sigma_{\varphi\varphi}$-moment- only ECAL; grey solid triangle: $\sigma_{\varphi\varphi}$-moment- only HCAL

$E_{rel}^{\mathrm{EMF}_{tow}=0\cdots1}$ show a better performance in the medium p_{T}-regime ($\approx 50-300\,\mathrm{GeV}$), but the difference to the global jet EMF is small and for high p_{T}, the variables loose their strength.

5.4.2. Jet-width variables

The jet-width variables discussed above are compared using bin-by-bin corrections (see Figure 5.14). Comparing the $\sigma_{\eta\eta}$-moment and the $\sigma_{\varphi\varphi}$-moment, the impact on the resolution is very similar, the resolution is improved by $\approx 15\,\%$ at high p_{T}. Evaluating the flavour dependence, the $\sigma_{\varphi\varphi}$-moment performs slightly better than the $\sigma_{\eta\eta}$-moment in decreasing the difference of the mean jet responses. The response difference is decreased by about $50\,\%$ in both cases at $p_T^{gen} = 100$ GeV. The width in φ is calculated by combining the energy depositions in the ECAL and HCAL. In order to disentangle the importance of the individual sub detectors, $\sigma_{\varphi\varphi}$-moments have been defined for the ECAL and HCAL separately. It is found that the $\sigma_{\varphi\varphi}$-moment based only on the ECAL-information performs almost as well as the combined $\sigma_{\varphi\varphi}$-moment over a wide p_{T}-range. The good performance of the HCAL-$\sigma_{\varphi\varphi}$-moment at low p_{T} is an artifact of the binning in $p_T^{gen}$and is not observed for a binning in p_T^{L2L3} (not shown here).

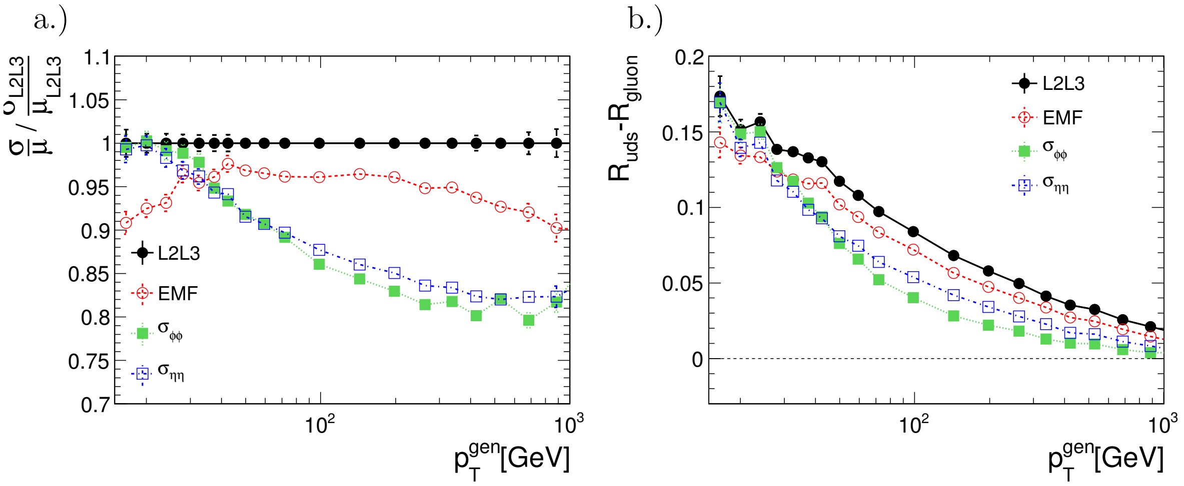

Figure 5.15.: Overall comparison:
a.) Relative resolution after subsequent “bin-by-bin corrections” scaled to the relative resolution after L2L3-correction.
b.) Difference of the mean responses determined separately from a Gaussian fit for a pure light quark and a pure gluon sample.
red open circle: EMF; green solid square: $\sigma_{\varphi\varphi}$-moment; blue open square: $\sigma_{\eta\eta}$-moment

5.4.3. Overall

Comparing the EMF and jet-width variables, the $\sigma_{\varphi\varphi}$-moment, the $\sigma_{\eta\eta}$-moment, and the traditional EMF perform best. In Figure 5.15, the performance of these variables is compared. It is observed that – while the differences are small at low p_{T}– the improvement by using jet-width variables instead of the electromagnetic fraction EMF is quite significant for a medium-to-high transverse momentum of the jet. As discussed before, the flavour dependence can be reduced most significantly by using the $\sigma_{\varphi\varphi}$-moment. At $p_T^{gen} = 100$ GeV, the resolution is improved by $\approx 15\,\%$ and the flavour difference is decreased from $\approx 7.5\,\%$ to $\approx 4\,\%$ by using the $\sigma_{\varphi\varphi}$-moment for a bin-by-bin correction.

5.5. Best combination of jet-width variables

As has been shown in the above, a jet-width variable is most promising in achieving the previously defined aims. There exist a lot of possibilities to define jet-width variables similar to the $\sigma_{\varphi\varphi}$-moment, i.e. one could define a jet width in ΔR. Several similar variables have been tested (see Appendix A for all variables), but linear combinations of the $\sigma_{\eta\eta}$-moment and $\sigma_{\varphi\varphi}$-moment performed best of all examined approaches.

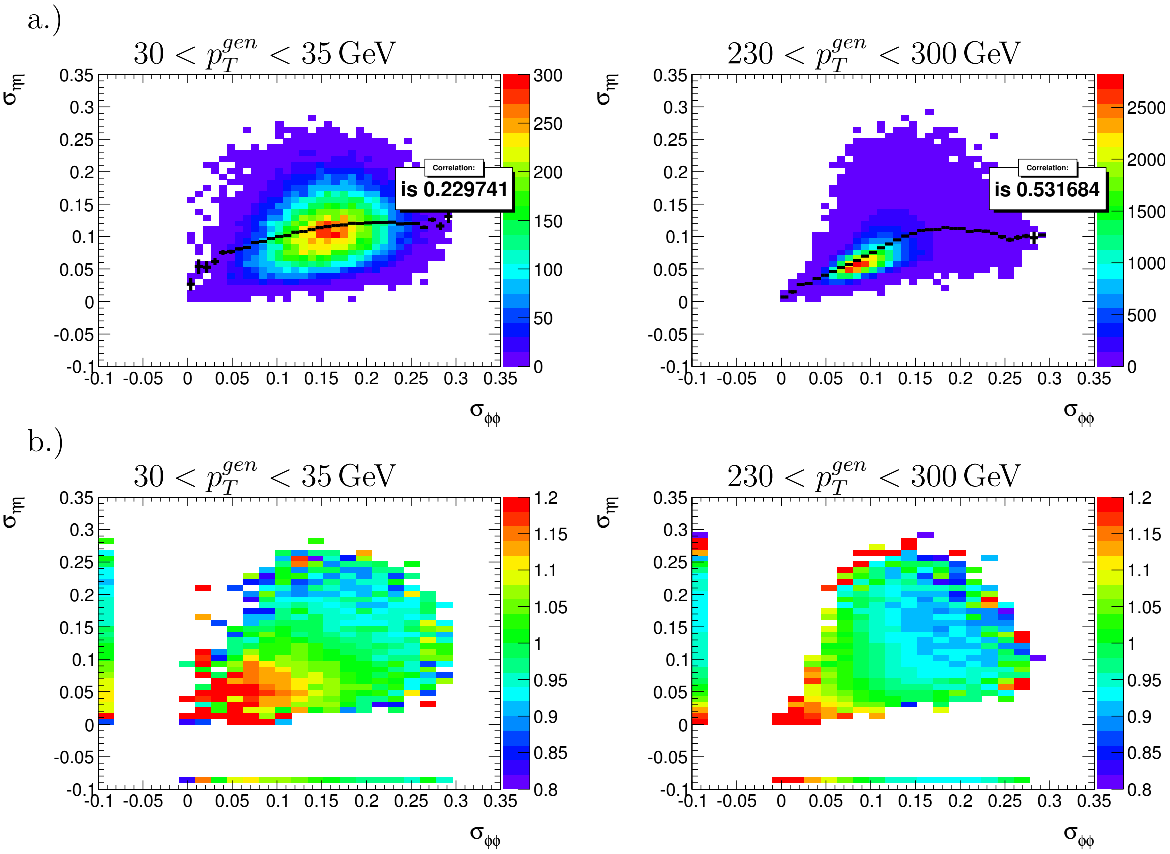

Figure 5.16.: a.) Correlation of $\sigma_{\varphi\varphi}$ and $\sigma_{\eta\eta}$ for two p_T^{gen}-ranges.
b.) Correlation of $\sigma_{\varphi\varphi}$ and $\sigma_{\eta\eta}$ with the mean L2L3-response in each bin (indicated with the coloured z-scale).

5.5.1. Linear decorrelation

In order to find the best possible combination, a linear decorrelation of the moment-variables has been performed. In Figure 5.16(a), the correlation of the two variables is shown. The correlation coefficient increases for higher p_{T}. However, the correlation of the two variables with the response, as shown in Figure 5.16(b), is even more important. It can clearly be seen that a rotation of the variables in the $\sigma_{\varphi\varphi}$-$\sigma_{\eta\eta}$ plane would allow for a better use of the response dependence in the central region of $\sigma_{\varphi\varphi}$ and $\sigma_{\eta\eta}$. This can be achieved by formally doing a linear decorrelation:
The covariance matrix can be defined as

$$\mathrm{Cov}(X_1, X_2) = \langle X_1 - \langle X_1 \rangle\rangle \cdot \langle X_2 - \langle X_2 \rangle\rangle \tag{5.7}$$

where the diagonal elements denote the variance of the variables and the off-diagonal elements denote the correlation coefficients, when normalised to the variance:

$$\mathrm{Corr}(X_1, X_2) = \frac{\mathrm{Cov}(X_1, X_2)}{\sqrt{\mathrm{Var}(X_1)} \cdot \sqrt{\mathrm{Var}(X_2)}} \tag{5.8}$$

The covariance matrix can now be diagonalised in order to remove the linear correlations. There always exists an orthogonal matrix M that diagonalises the covariance matrix C. Following from this, the diagonal matrix D can be obtained as

$$D = M \cdot C \cdot M^T \tag{5.9}$$

The matrix M can be applied to the underlying variables X_1 and X_2 and acts as a rotation matrix. The new variables

$$\begin{pmatrix} Y_1 \\ Y_2 \end{pmatrix} = M \cdot \begin{pmatrix} X_1 \\ X_2 \end{pmatrix} \tag{5.10}$$

are then uncorrelated. Such a matrix can be calculated from the covariance matrices of $\sigma_{\eta\eta}$ and $\sigma_{\varphi\varphi}$ in all p_{T}-regions and is stable over a wide p_{T}-range (i.e. the coefficients have very similar values). This defines the two new variables A and B (matrix M from 80-120 GeV region) as

$$\begin{pmatrix} A \\ B \end{pmatrix} = \begin{pmatrix} -0.7485 & -0.6631 \\ -0.6631 & 0.7485 \end{pmatrix} \cdot \begin{pmatrix} \sigma_{\varphi\varphi} \\ \sigma_{\eta\eta} \end{pmatrix} \tag{5.11}$$

It is observed that the correlation of the two new variables is much smaller in all p_{T}-regions and that the correlation with the response is concentrated in the variable A. This is shown in Figure 5.17(a) and (b). A bin-by-bin correction using the variable A leads to a resolution improvement of more than 20 % for p_T^{gen}above 200 GeV and reduces the flavour dependence by ≈ 50 % at $p_T^{gen} = 100$ GeV.

5.5.2. Jet-width variable

The variable A determined by linear decorrelation is very similar to just adding the two moments as seen from the values of the matrix elements in equation (5.11). Indeed, it is sufficient to calculate the arithmetic mean of $\sigma_{\varphi\varphi}$ and $\sigma_{\eta\eta}$. This measure is defined as

$$\text{jet width } JW = \frac{\sigma_{\varphi\varphi} + \sigma_{\eta\eta}}{2} \tag{5.12}$$

The distribution of JW is depicted in Figure 5.18(a). The distribution appears slightly widened in comparison to the individual variables. In Figure 5.18(b), the strong dependence of the response on the jet-width variable JW is depicted. In Figure 5.18(c) the correlation of the JW with the flavour composition is shown. The strong correlation of the JW with the response is linked to the strong correlation with the flavour composition. The connection between the jet-width variable JW and the flavour is depicted in more detail in Figure 5.19. In the upper plot, the mean values of the jet-width variable JW are shown as a function of $p_T^{gen}$for jet samples with different flavours. It is observed that the gluon jets are much broader than uds jets allowing for the observed reduction of the flavour dependence of the response. In the lower two plots the distribution of the

a.)

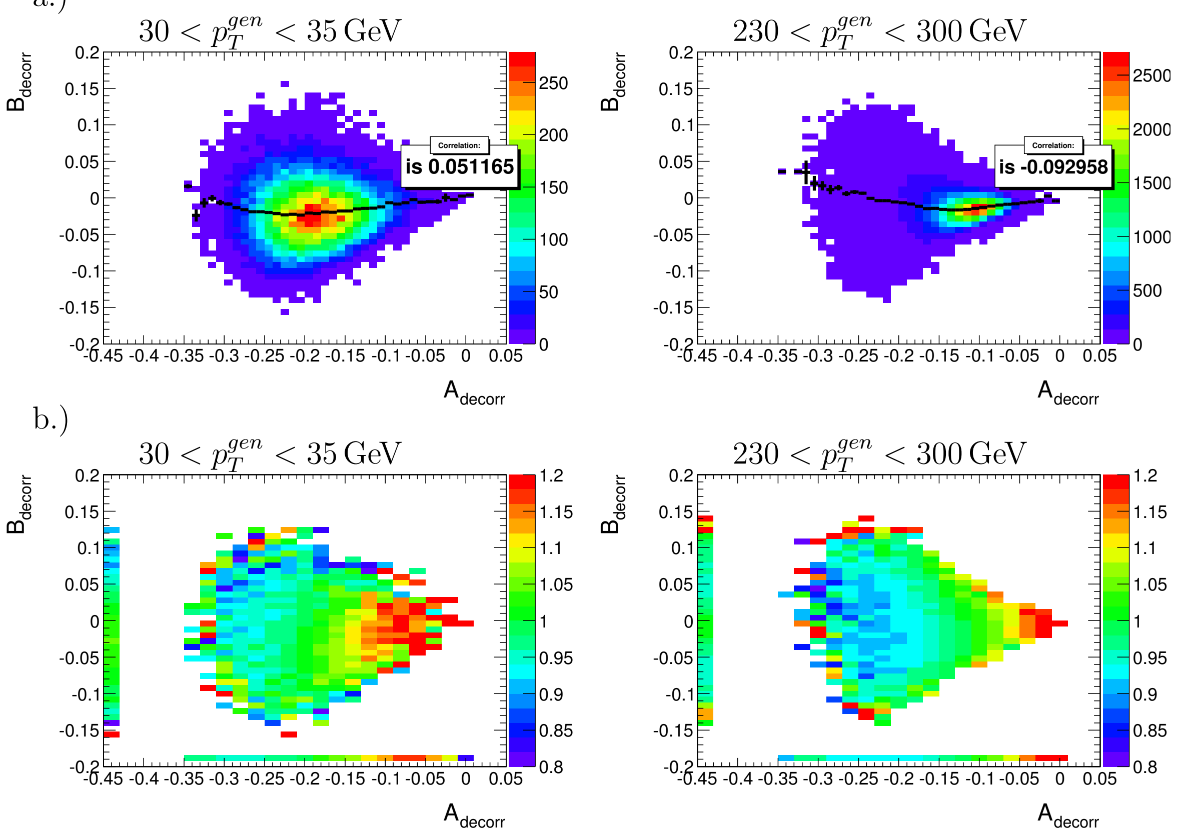

b.)

c.) resolution improvement

d.) flavour difference

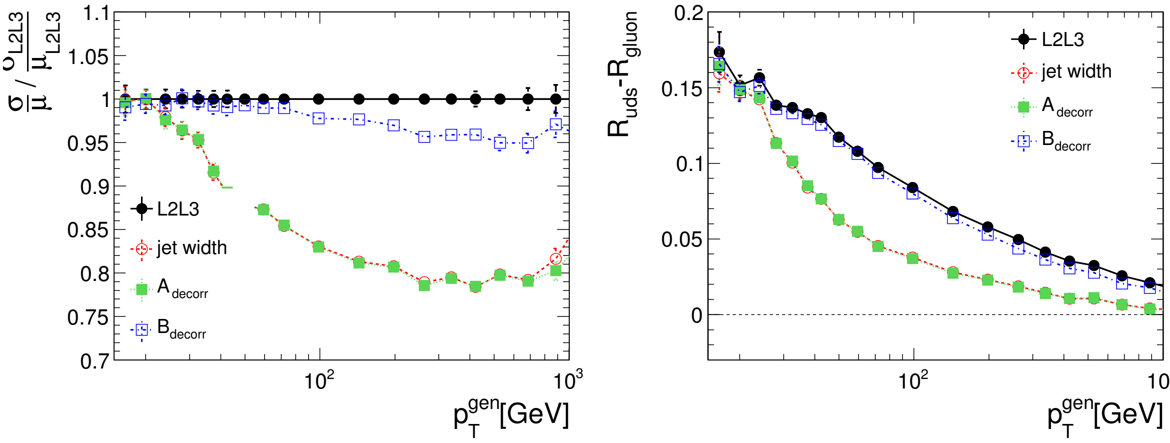

Figure 5.17.: a.) Correlation of A and B for two p_T^{gen}-ranges.
b.) Correlation of A and B with the mean L2L3-response in each bin (indicated with the coloured z-scale).
c.) Relative resolution after subsequent "bin-by-bin corrections" scaled to the relative resolution after L2L3-correction.
d.) Difference of the mean responses determined separately from a Gaussian fit for a pure light quark and a pure gluon sample.
red open circle: jet EMF; green solid square: A; blue open square: B

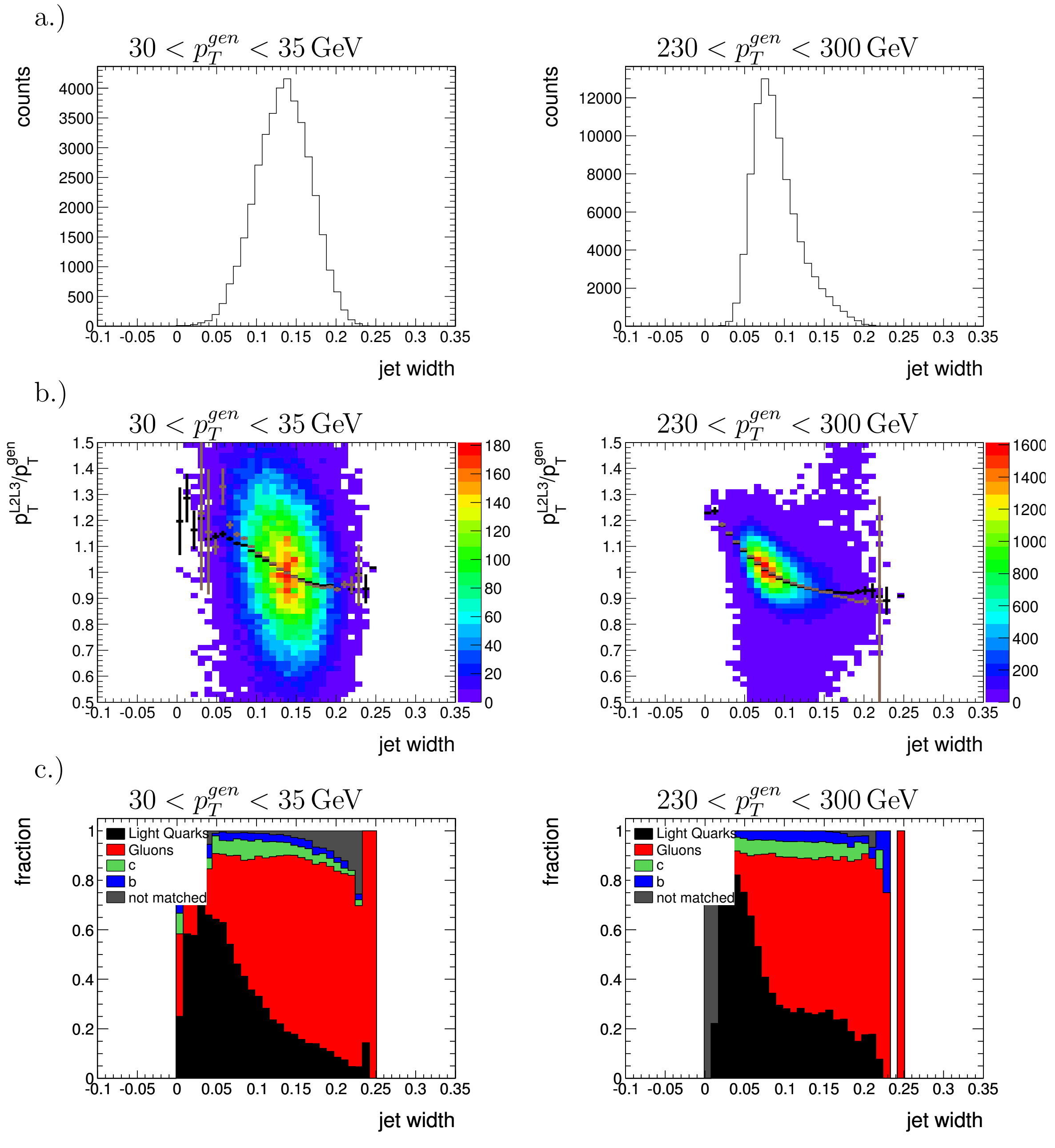

Figure 5.18.: a.) Distribution of the jet width in two p_T^{gen}-ranges.
b.) Correlation of the response R_{L2L3} and the jet width; coloured z-scale: counts; black: mean response in bins of JW; brown: mean of a Gaussian fit of the response in bins of jet width.
c.) Relative flavour composition in bins of the jet width in two p_T^{gen}-ranges.

jet-width variable JW is shown in two p_T^{gen}-ranges. The jets in the examined simulated data have been split according to their flavour. The overlap in the distributions of JW for gluon and light quark jets is significant so that the jet-width variable JW alone does not discriminate the flavour of single jets.[3] Still, this behaviour is directly linked to the potential of the jet-width variable in improving the energy calibration.

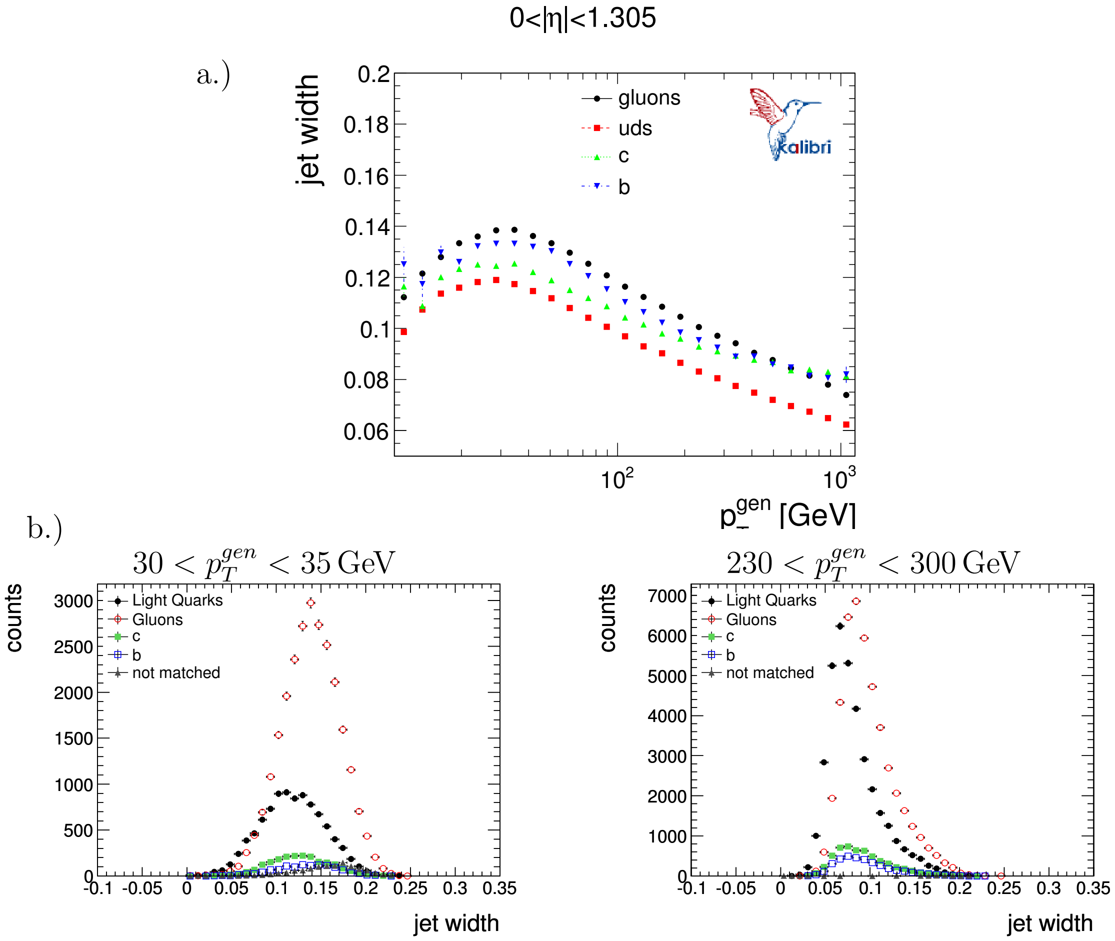

Figure 5.19.: a.) Mean values of the jet-width variable JW are determined for pure jet samples of each flavour and shown as a function of p_T^{gen}.
b.) Distribution of the jet-width variable JW in the MC sample under study, split up corresponding to the different flavours in two p_T-regions.

The jet-width variable JW has a performance equivalent to the decorrelated variable A presented in Section 5.5.1 as is shown in Figure 5.17(c). The comparison to the more traditional jet-width variables $\sigma_{\eta\eta}$ and $\sigma_{\varphi\varphi}$ is shown in Figure 5.20. The jet-width variable performs better in reducing the flavour dependence of the jet response and improving the jet-energy resolution in all p_T-regions. The jet-width variable JW leads to a resolution improvement of more than 20 % for p_T^{gen}above 200 GeV and reduces the flavour dependence of the response by more than 50 % at $p_T^{gen} = 100$ GeV.

---

[3] Some preliminary studies have been performed on discriminating gluon and light quark jets using the jet width and other jet-shape variables in the course of this thesis using TMVA. They showed that the combination of various jet-shape variables allows for a relatively good discrimination of gluon and light quark jets. This could be elaborated in further studies, but is not in the scope of this analysis. In the following, the discussion will concentrate on the use of the jet-width variable JW for the development of an additional jet-energy correction.

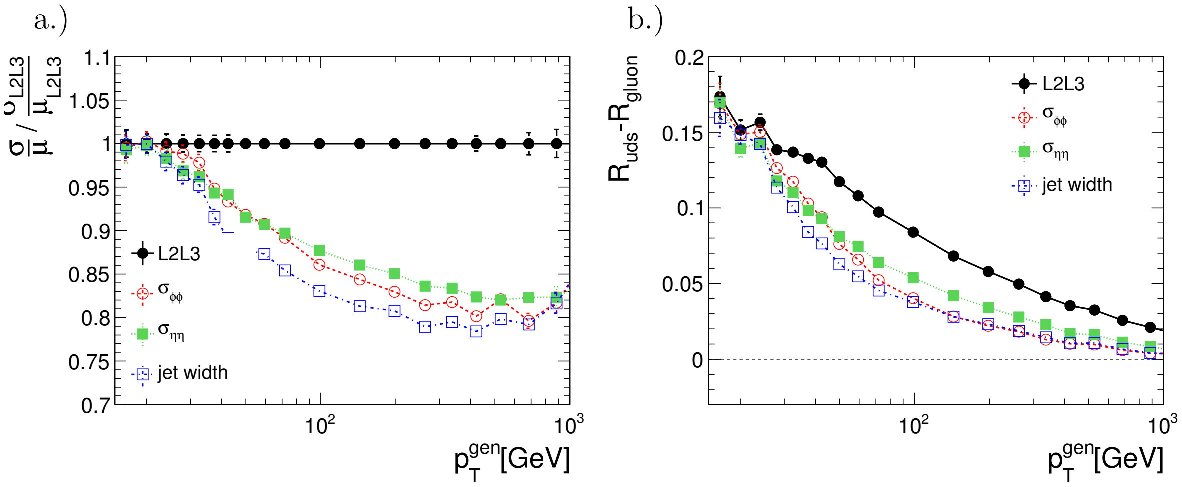

Figure 5.20.: a.) Relative resolution after subsequent "bin-by-bin corrections" scaled to the relative resolution after L2L3-correction.
b.) Difference of the mean responses determined separately from a Gaussian fit for a pure light quark and a pure gluon sample.
red open circle: $\sigma_{\varphi\varphi}$-moment; green solid square: $\sigma_{\eta\eta}$-moment; blue open square: JW

Shape of the corrected response for JW: The response of L2L3-corrected jets has been compared to the response of jets after a subsequent bin-by-bin correction using the jet-width variable. The results are shown in Figure 5.21 for $40 < p_T^{gen} < 45\,\mathrm{GeV}$ and $380 < p_T^{gen} < 470\,\mathrm{GeV}$. In the upper plots one can see that the Gaussian shape is preserved and the peak becomes narrower. In the lower plots with a logarithmic y-scale, only very few additional outliers are visible (similar observations can be made for the other variables as well). This can be regarded as a validation for the bin-by-bin correction: The bin-by-bin jet-width correction improves the jet-energy resolution without compromising the shape of the corrected response as could be the case by correcting only a certain subpopulation of the jets. The jet-width variable JW is chosen for the development of an elaborated correction as described in the next chapter. From now on, the term "jet width" refers to the jet-width variable JW.

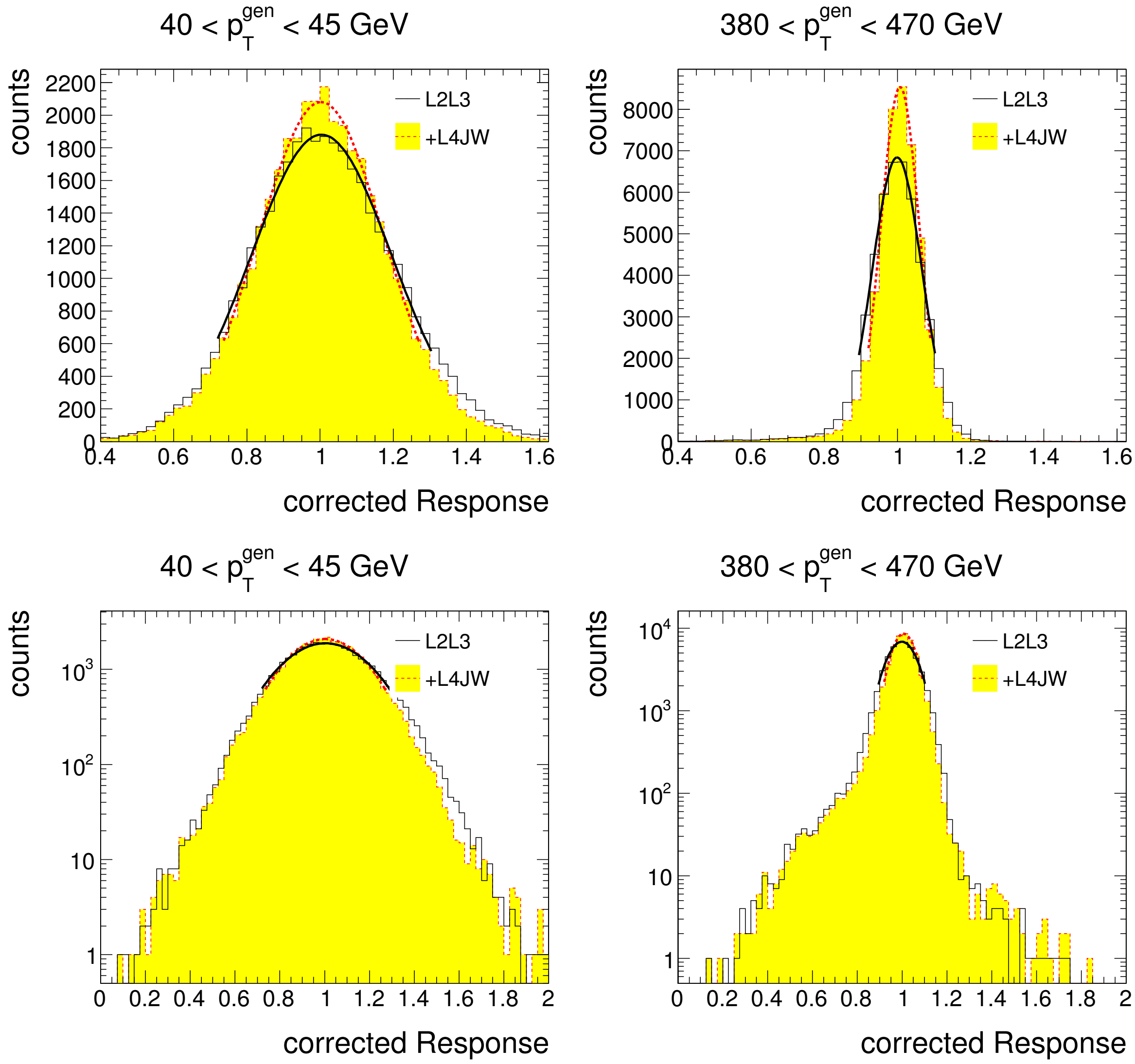

Figure 5.21.: Comparison of the initial response R_{L2L3} and the JW-corrected response with iterative Gaussian fit of the core $[\mu - 1.5\sigma, \mu + 1.5\sigma]$. Left: $40 < p_T^{gen} < 45$ GeV; right: $380 < p_T^{gen} < 470$ GeV (black, L2L3-correction; red, additional JW-correction). Upper plots: linear y-scale; lower plots: logarithmic y-scale.

Chapter 6.

Jet-width correction

In the previous chapter, a set of candidate variables for a jet-energy correction in addition to the L2L3-corrections have been examined. The jet-width variable JW was seen to perform best in reducing the flavour dependence of the mean jet response and improving the jet-energy resolution. In order to ensure a fully functional jet-energy correction, the dependence of the mean jet response has to be determined and modelled as a function of the jet transverse momentum and the jet width. This leads to the following three requirements:

- The correction should be a smooth function in order to avoid any discontinuity in the resulting correction factors. This is achieved by the following: A polynomial of second order is used to approximate the needed correction factors as a function of the jet width in each p_{T}-range (see Figure 6.1). The parameters of this polynomial themselves are parametrised as a function of p_T^{L2L3} in order to be applicable in terms of the factorised jet-energy-correction approach to data.
- The jet-energy scale as prescribed by the L2L3-corrections should be preserved. This additional constraint on the fit parameters will be described in Section 6.2.
- The correction should be applicable to jets in all detector regions. This is achieved by deriving the correction parameters separately in four pseudorapidity regions corresponding to substantial changes in the granularity and type of the calorimeters.

6.1. Modelling of the response

The jet-width correction, as it is parametrised here, aims at removing the dependence on the jet width for the jet response. In the above (see Chapter 5), where a suitable correction variable was selected, the mean response as a function of the jet width was determined and shown in ranges of p_T^{gen} in order to extract correction factors. This is the starting point for a more detailed parametrisation.

However, the mean response as used in Chapter 5 is sensitive to outliers in the distribution. To avoid this sensitivity, the Gaussian mean $\langle R_{L2L3}\rangle_{\mathrm{Gauss}}$ of R_{L2L3}, the L2L3-corrected jet response, is used in the following. It is determined from an iterative Gaussian fit (see Section 5.4). $\langle R_{L2L3}\rangle_{\mathrm{Gauss}}$ is a good estimator for the mean response of the core of the

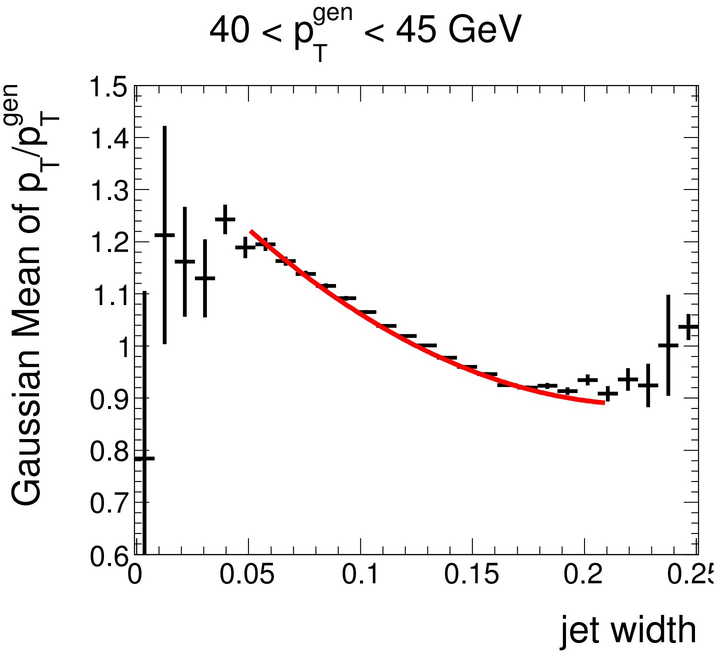

Figure 6.1.: Gaussian mean of R_{L2L3} in bins of the jet width for $40 < p_T^{gen} < 45$ GeV in the barrel region. Here, the inverse of the function for the correction factor as given in equation (6.2) is fitted to the Gaussian mean within the [0.005,0.095] quantiles of the JW-distribution.

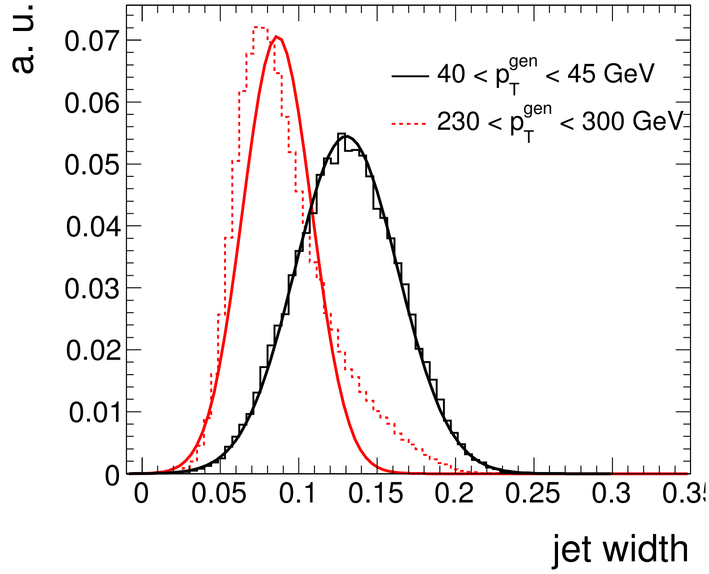

Figure 6.2.: Normalised distribution of the jet width in the barrel region (arbitrary units) for two different p_T^{gen}-regions. A Gaussian is fitted to the distribution.

response distribution.
In analogy to Section 5.4, the correction factor is determined as the inverse of the Gaussian mean of the response

$$\mathrm{CF}(x_{JW}) = \frac{1}{\langle R_{L2L3} \rangle_{\mathrm{Gauss}}} \tag{6.1}$$

When plotted in bins of the jet width for different p_{T}-ranges (see Figure 6.1), the Gaussian mean of the response can be approximated with the inverse of the correction factor CF. For this, CF is defined as a second-order polynomial:

$$\mathrm{CF}(x_{JW}) = a + b(x_{JW} - \mu_{JW}) + c(x_{JW} - \mu_{JW})^2 \tag{6.2}$$

where x_{JW} denotes the jet width of an individual jet, μ_{JW} denotes the Gaussian mean of the distribution of the jet-width variable in the examined p_{T}-region (see Figure 6.2), and a, b, and c are free parameters. The fit with this polynomial can be performed with satisfactory convergence in all p_{T}-regions from very low to very high transverse momenta.

6.2. Constraint to preserve energy scale

The energy scale after L2L3-corrections is regarded as the correct energy scale and therefore should, on average, not change. Therefore, the average correction is required to be unity:

$$\langle correction \rangle \overset{!}{=} 1 \tag{6.3}$$

Taking this as a premise, the parametrisation can be constrained such that the mean jet-energy scale is preserved after a subsequent jet-width correction. The "mean correction factor" can be calculated by a convolution of the distribution of the correction variable and the correction function:

$$\int_{-\infty}^{+\infty} f(x_{JW}) \cdot \mathrm{CF}(x_{JW}) \; dx_{JW} = \langle correction \rangle \tag{6.4}$$

Here, $f(x_{JW})$ denotes the normalised distribution of the jet-width variable as shown in Figure 6.2. A Gaussian

$$f(x_{JW}) = \frac{1}{\sqrt{2\pi}\sigma_{JW}} \cdot exp\left(- \frac{(x_{JW} - \mu_{JW})}{2\sigma_{JW}^2} \right)^2 \tag{6.5}$$

is used to describe the basic features of the distribution despite some disagreement, which is observed for high transverse momenta. This is done in order to extract a simple analytic solution. A test of the absolute energy scale after the correction in Section 7.2 will determine whether this assumption is valid. Computing the mean correction factor from equation (6.4) (using equation (6.2) and 6.5) then results in

$$\langle correction\rangle = a + c\sigma_{JW}^2 \tag{6.6}$$

which can be used as a constraint for the parameter a of the constant term in the parametrisation. The result is $a = 1 - c\,\sigma_{JW}^2$.
The final parametrisation then becomes:

$$\mathrm{CF}(x_{JW}) = (1 - c\sigma_{JW}^2) + b(x_{JW} - \mu_{JW}) + c(x_{JW} - \mu_{JW})^2 \tag{6.7}$$

where σ_{JW} and μ_{JW} are obtained from a Gaussian fit to the JW-distribution and b and c remain free parameters in the fit of the correction function. It is designed to preserve the jet-energy scale by construction.

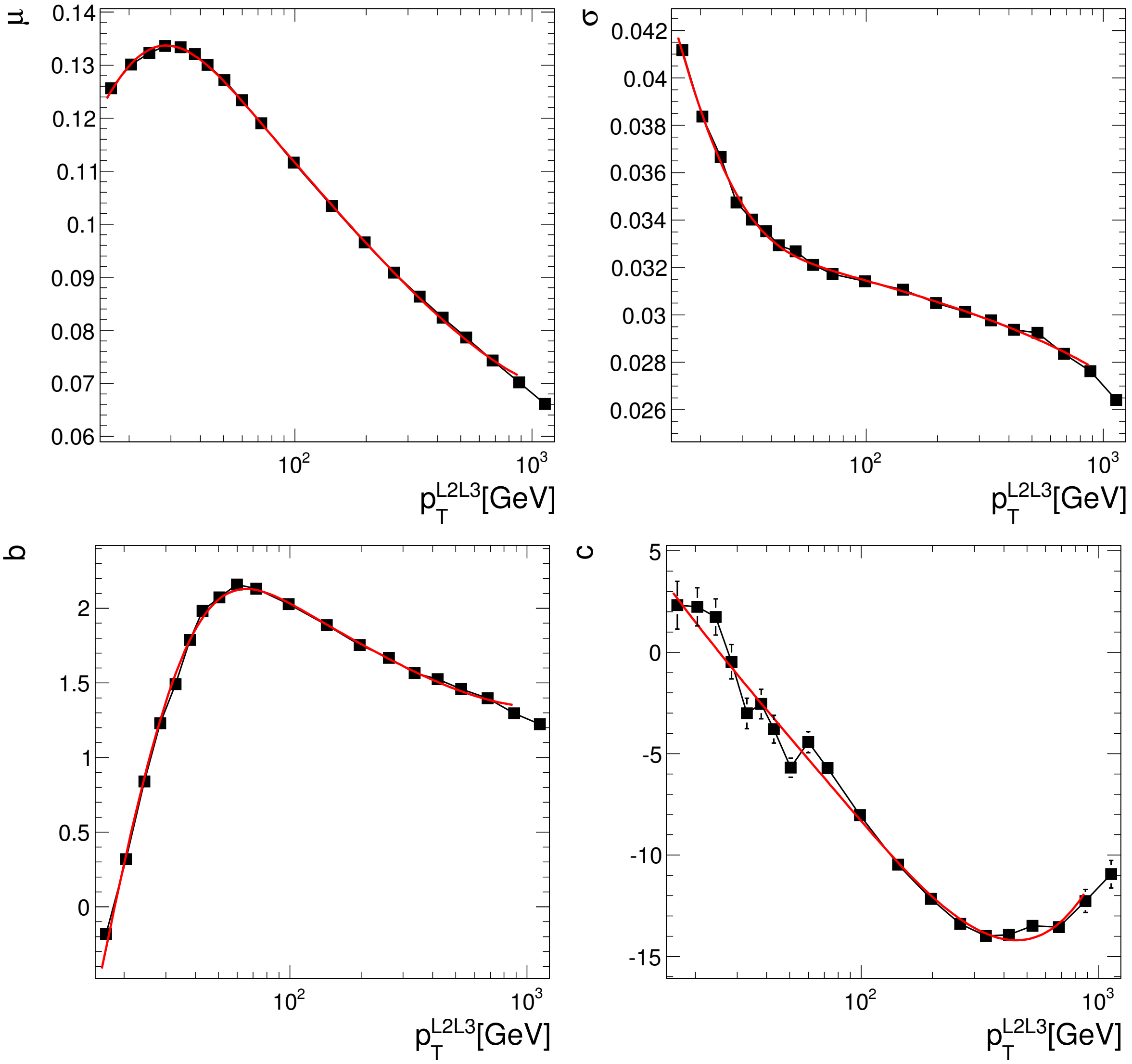

Figure 6.3.: The p_T^{L2L3}-dependence of the four parameters $b, c, \sigma_{JW}, \mu_{JW}$ of the correction function in the barrel region ($0 < |\eta| < 1.305$) as given by a bin-by-bin correction with binning in p_T^{gen}, fitted with function from equation (6.8).

6.3. p_T-dependence of parameters

The correction function should be a smooth function of p_T^{L2L3} and the jet width. The two parameters σ_{JW} and μ_{JW} are the characteristic parameters of the assumed Gaussian distribution of the jet-width variable discussed in Section 6.2.

The p_T^{L2L3}-dependence of the four parameters b, c, σ_{JW}, and μ_{JW} of the correction function as given by the results of the bin-by-bin correction for a binning in $p_T^{gen}$is depicted in Figure 6.3 for the barrel region and has been determined for jet-momenta above 15 GeV. The characteristics of all parameters can be described well with a function with 5 parameters:

$$g(p_T^{L2L3}) = \alpha + \beta \cdot log(p_T^{L2L3}) + \gamma \cdot p_T^{L2L3} + \delta \cdot exp(\varepsilon \cdot p_T^{L2L3}) \tag{6.8}$$

The first three parameters model the high-p_T dependence while the parameters δ and ε can approximate the behaviour at low p_T.

In all discussions starting from Chapter 5, the barrel region ($|\eta| < 1.305$) of the CMS-detector was considered. This central region of the detector is best-understood in terms of jet-energy calibration as discussed in Section 4.3. However, the considerations for a jet-width correction also hold in the other detector regions. The design of the detector naturally defines four pseudorapidity regions differing in the type of calorimeters and the granularity (see Appendix C):

- **$0 < |\eta| < 1.305$:** The barrel region with same segmentation in η and φ for all towers of 0.087×0.087.
- **$1.305 < |\eta| < 2.6$:** The endcap region has the same type of calorimeters as the barrel region, but the segmentation in η and φ varies and becomes coarser.
- **$2.6 < |\eta| < 2.964$:** The transition region between the endcap calorimeters and the HF calorimeter, where both types of calorimeters overlap.
- **$2.964 < |\eta| < 5.192$:** In the most forward region, the segmentation is relatively coarse and the calorimeter is of a different type (Hadron Forward, see Section 3.5).

The description in equation (6.8) works in all four pseudorapidity regions reasonably well (see Appendix B).

6.4. Full parametrisation

The full parametrisation comprises 20 parameters for each pseudorapidity region. 2×5 parameters are needed to describe μ_{JW} and σ_{JW} and are determined from the JW-distribution. Another 2×5 parameters are fitted in order to describe the dependence of the response on the jet width (parameters b and c). The full parametrisation of the correction in the four η-regions needs 80 parameters $\alpha_{ij}, \beta_{ij}, \gamma_{ij}, \delta_{ij}, \varepsilon_{ij}$ ($i = b, c, \mu_{JW}, \sigma_{JW}$; $j = 1 \cdots 4$ for the four η-regions defined in Section 6.3).

μ_{JW}, σ_{JW}, b, and c can be determined by calculating their values according to equa-

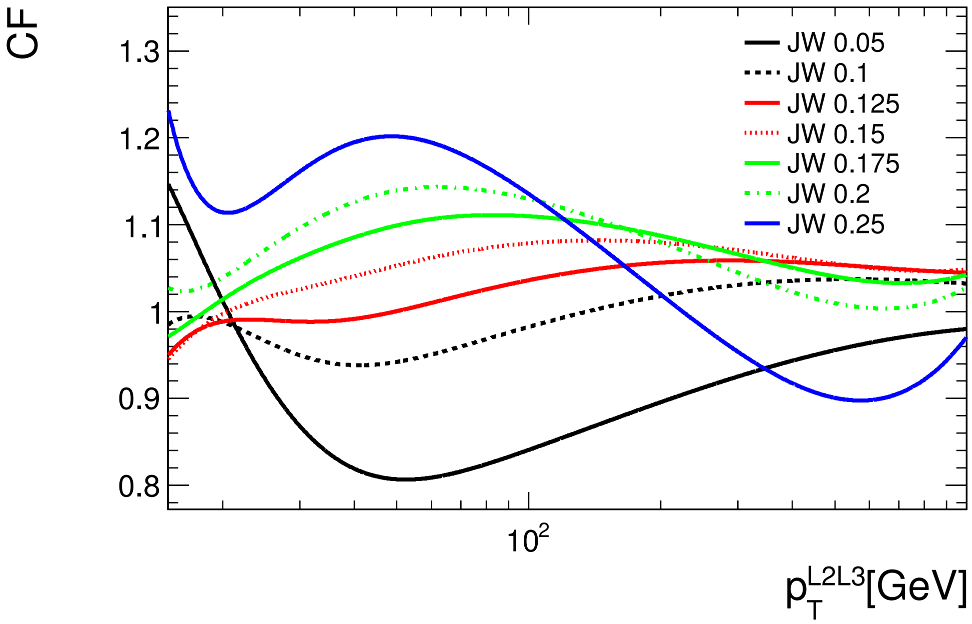

Figure 6.4.: Resulting correction factors derived using Kalibri as a function of p_T^{L2L3} for different values of the jet width ranging from 0.05 to 0.25 in the barrel region. The correction factor varies between 0.8 and 1.2 for most values of JW.

tion (6.8). The correction factor is then calculated from the polynomial derived in section 6.2:

$$\mathrm{CF}(x_{JW}, p_T) = (1 - c\sigma_{JW}^2) + b(x_{JW} - \mu_{JW}) + c(x_{JW} - \mu_{JW})^2 \tag{6.9}$$

6.5. Parameter determination using Kalibri

The parameters b and c for the full parametrisation, as described in section 6.4, have been derived using the Kalibri framework. Here, Kalibri is used to determine the jet-width-correction parameters for L2L3-corrected jets using the MCTruthEvent-class (see Section 4.3.6). All parameters have been determined as a function of the L2L3-corrected transverse momentum p_T^{L2L3} in order to be applicable as an optional step in addition to the L2L3-corrections within the factorised jet-energy correction approach of CMS.

The results for b and c and the values of the fixed parameters σ_{JW} and μ_{JW} are listed in the Appendix D. The resulting correction factors as a function of p_T^{L2L3} are depicted for the barrel region in Figure 6.4 for different jet widths. The correction factors vary from 0.8 for very narrow jets with relatively low p_T^{L2L3} up to 1.2 for very broad jets with relatively low p_T^{L2L3}. The mean value μ_{JW} of the JW-distribution is ≈ 0.1. For such values the correction factor is relatively close to unity.

Chapter 7.

Evaluation on simulated data

The jet-width correction as derived in the previous chapter is expected to improve the jet-energy resolution and decrease the dependence of the mean jet response on the flavour of the jet. It has already been assured that the quality of the data is not diminished for a bin-by-bin jet-width correction (see Section 5.5.2), i.e. that there are no additional outliers produced and the Gaussian shape of the corrected response is preserved. Figure 7.1 repeats this cross check for the parametrised version of the correction. It shows that the statement also holds for the parametrised version, namely that no additional outliers are produced. Following up on this, it has to be checked that the dependence of the response on the jet width vanishes and that the energy scale as set by the L2L3-corrections is not changed by the jet-width correction. This validation is performed on the same simulated event sample that has been used for the derivation of the correction [1]. Furthermore, the effects of the correction considering the resolution improvement and flavour response difference are discussed. In order to do this, the mean response and the core resolution are determined from an iterative Gaussian fit of the corrected response (see Section 5.4 for a description of details).

7.1. Mean response vs. jet width

Figure 7.2 shows the Gaussian mean of the response as a function of the jet width. The response has been integrated over the full pseudorapidity region $|\eta| < 5.192$ and is shown in bins of p_T^{gen}. The black circles show the Gaussian mean determined from the L2L3-corrected response of calorimeter jets. A very strong dependence is observed in the medium p_T^{gen}-region. $\langle R_{L2L3}\rangle_{\mathrm{Gauss}}$ is > 1 for narrow jets and < 1 for broad jets. The value of the jet width where $\langle R_{L2L3}\rangle_{\mathrm{Gauss}} = 1$ decreases with p_T^{gen}. This corresponds to the decreasing mean of the distribution of the jet width (see e.g. Figure 6.2). The dependence is expected to vanish, once the jet-width correction is applied. Indeed, the dependence on the jet width almost vanishes over a wide p_T^{gen}-range for JW-corrected jets (shown with red squares). For very low values of p_T^{gen}, the parametrisation of the jet width becomes less valid as can be seen in the plot for the lowest p_T^{gen}-range. For high

---

[1] `/QCDFlat_Pt15to3000/Spring10-START3X_V26_S09-v1/GEN-SIM-RECO`

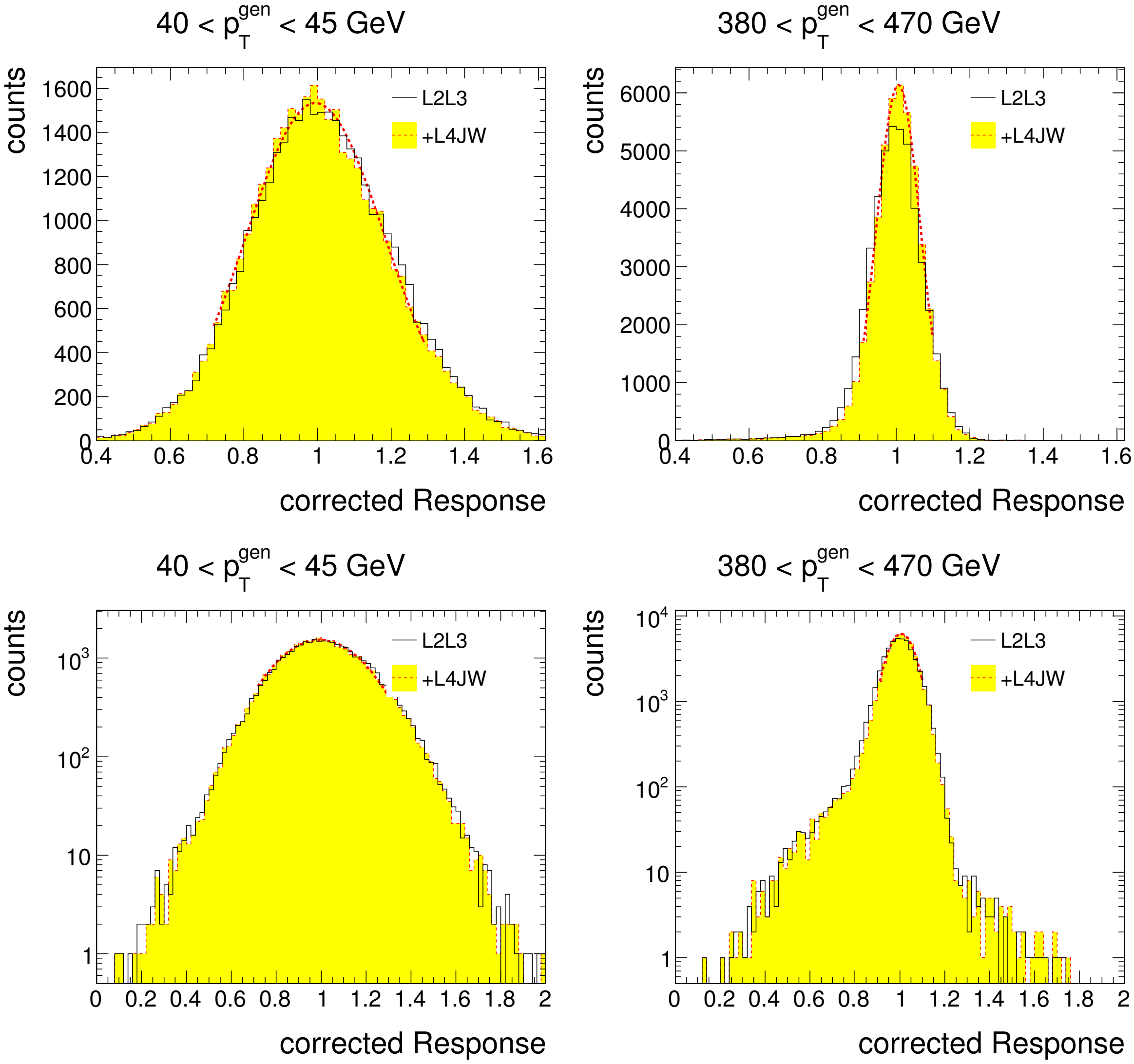

Figure 7.1.: Corrected response (applying the full parametrisation defined in the previous chapter) with iterative Gaussian fit of the core $[\mu - 1.5\sigma, \mu + 1.5\sigma]$. Left: $40 < p_T^{gen} < 45$ GeV; right: $380 < p_T^{gen} < 470$ GeV (black circles: L2L3-correction; red open squares: JW-correction). Upper plots: linear y-scale; lower plots: logarithmic y-scale.

p_T^{gen} and jet widths the dependence is not completely compensated, but this region of the jet width is only scarcely populated and is not expected to affect the overall performance.

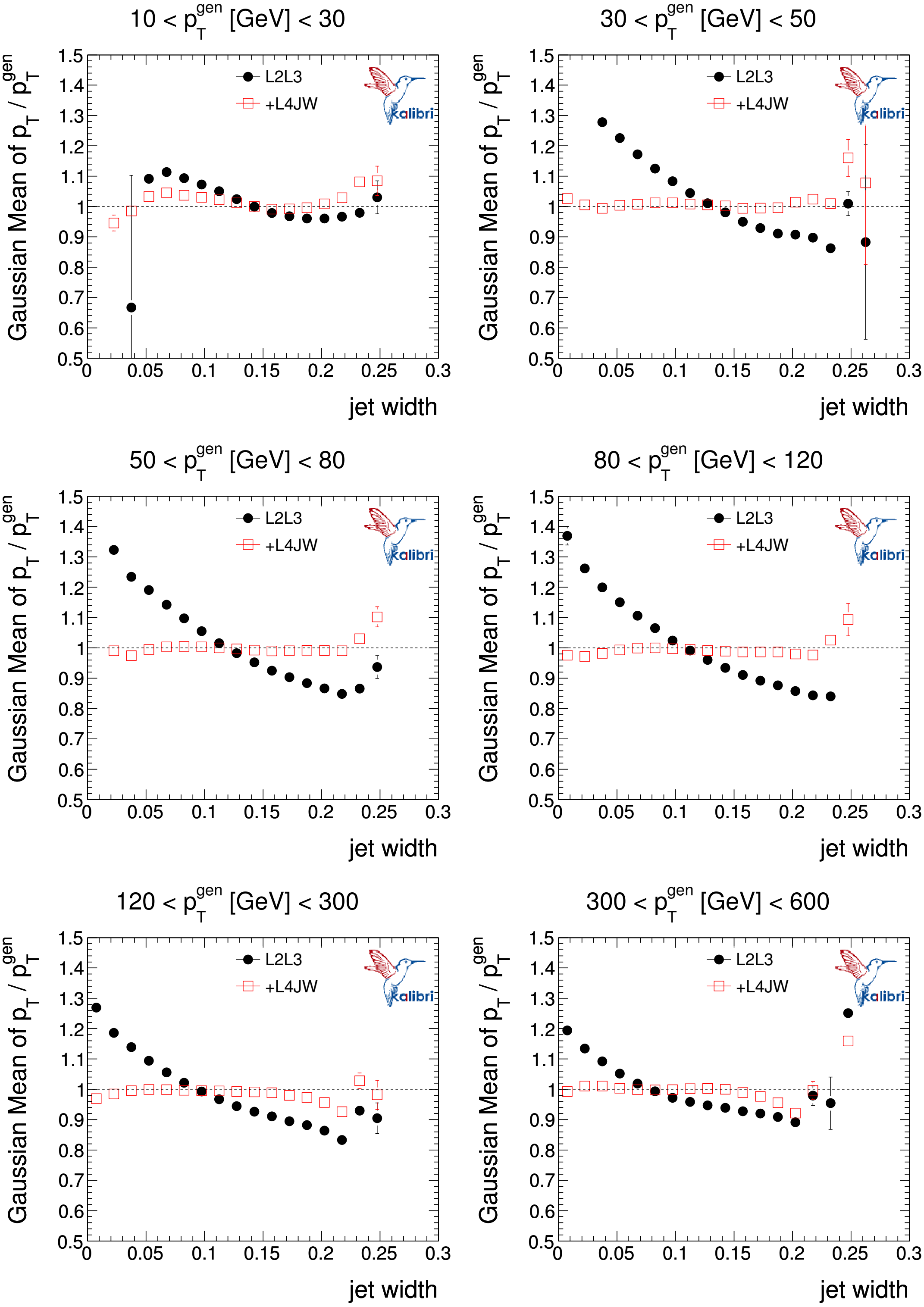

Figure 7.2.: Gaussian mean of the response as a function of the jet width before and after the jet-width correction in different p_T-regions (black circles: L2L3-correction; red open squares: JW-correction).

7.2. Mean response vs. p_T^{gen}

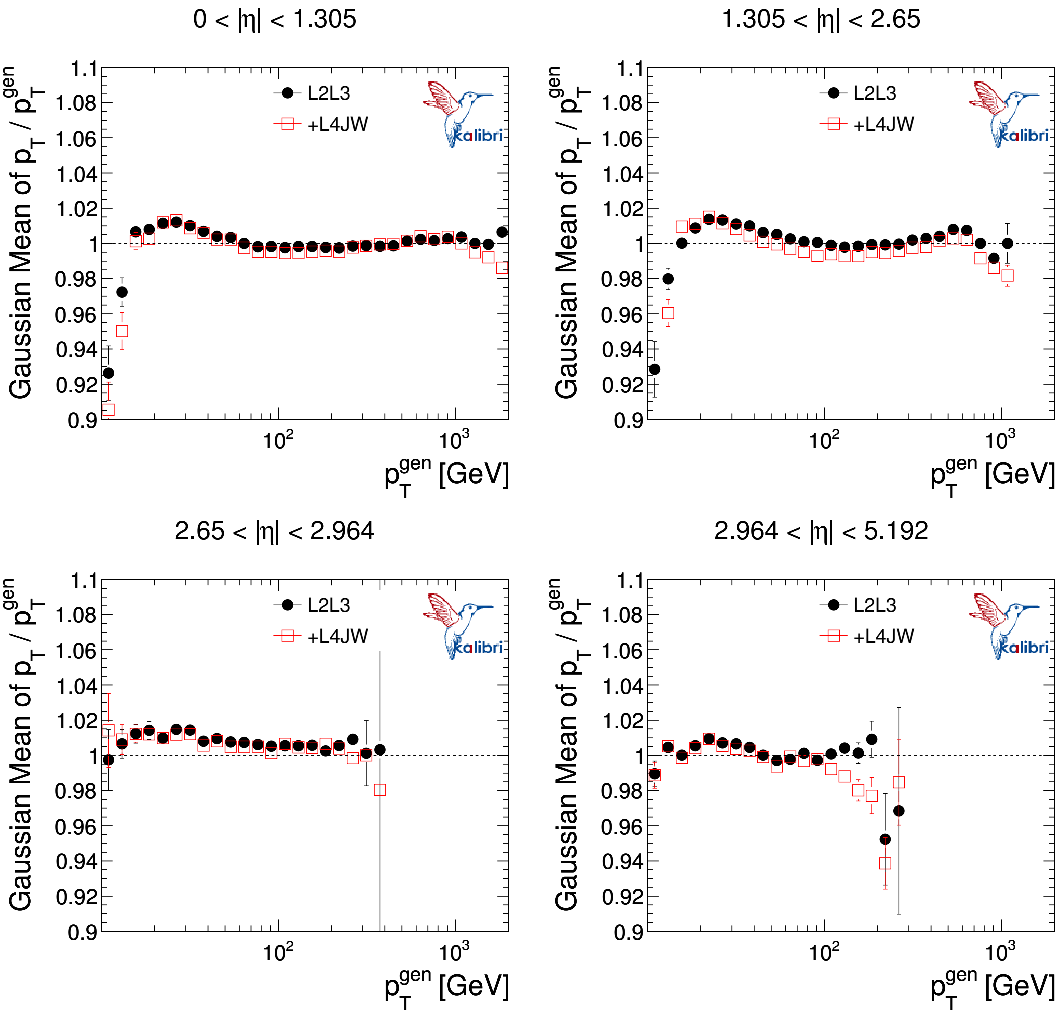

Figure 7.3.: Gaussian mean of the response as a function of p_T^{gen} before and after the jet-width correction in different η-bins (black circles: L2L3-correction; red open squares: JW-correction).

In Figure 7.3, the mean response is shown as a function of p_T^{gen}in all four η-regions. The JW-corrected response follows the L2L3-trend very closely. The energy scale as set by the L2L3-correction is preserved within $\approx 1\%$ after the subsequent application of the jet-width correction in almost all p_T^{gen}-regions in all four η-regions. The functionality of the additional constraint on the fit function as described in Section 6.2 is thus validated. The good agreement legitimates the Gaussian assumption for this purpose. Only in regions where the number of available MC events is small (e.g. very high p_T^{gen}) slight deviations are observed.

7.3. Resolution improvement

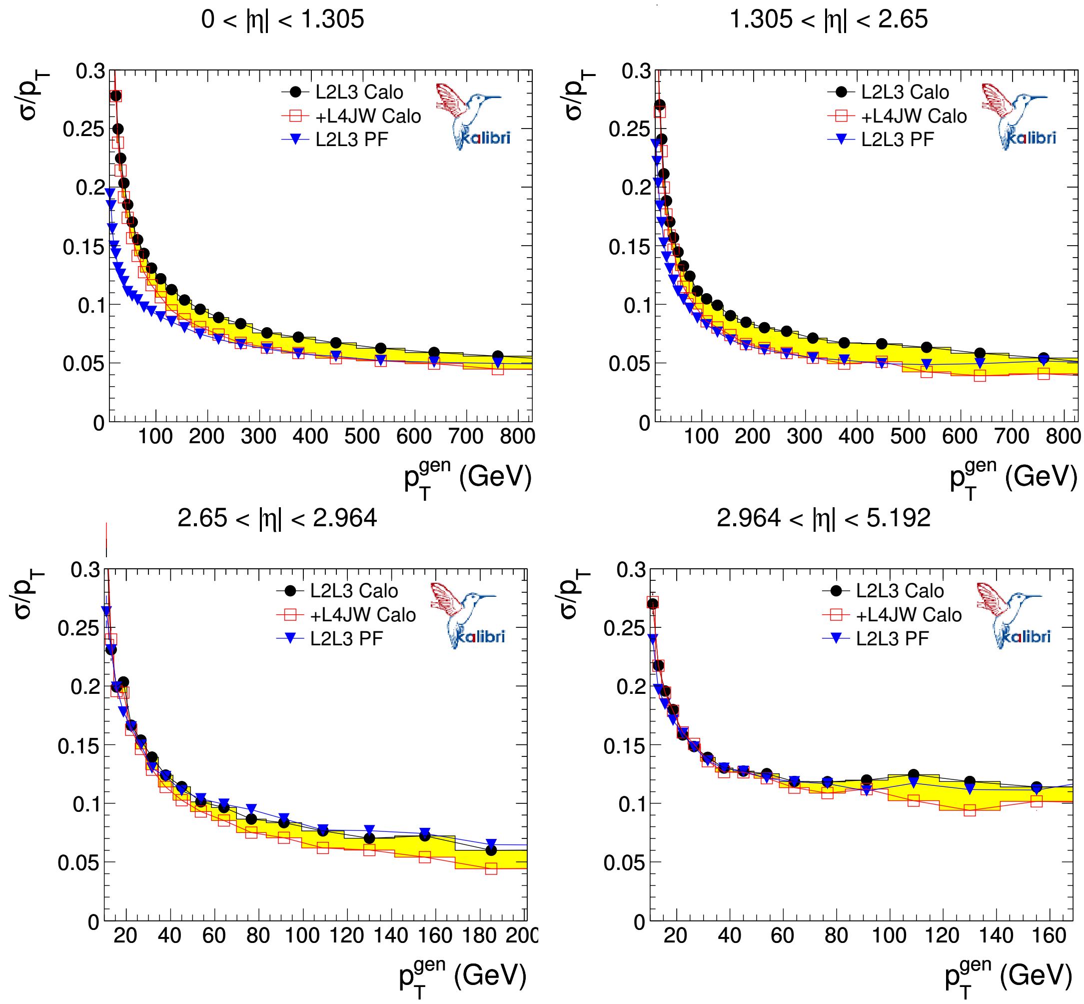

Figure 7.4.: Relative resolution as a function of p_T^{gen} for L2L3-corrected calorimeter jets, L2L3-corrected PF-jets and jet-width-corrected calorimeter jets in different η-bins (black circles: L2L3-correction; blue triangles: L2L3-corrected PF-jets; red open squares: JW-correction).

In order to judge the positive effects of the jet-width correction in the framework of factorised jet-energy corrections, the jet-energy resolution improvement is an important indicator. In Figure 7.4, the relative resolution is shown as a function of $p_T^{gen}$for L2L3-corrected jets and subsequently jet-width-corrected jets for all four η-regions. The difference is indicated with a filled area. Additionally, the relative resolution of L2L3-corrected PF-jets is shown. Even though the particle flow jet reconstruction has not been discussed in detail, it is very interesting to determine how much the resolution of calorimeter jets can be improved by a jet-width correction, and to compare this to what is achieved with the particle flow algorithm.

The previously used representation, where the relative resolution is scaled to the L2L3 relative resolution, is shown in Figure 7.5. This representation is only used for the purpose of comparison, the errors are thus simplifyingly approximated, neglecting the (existing) correlation of the relative resolutions. This defines an upper limit for the

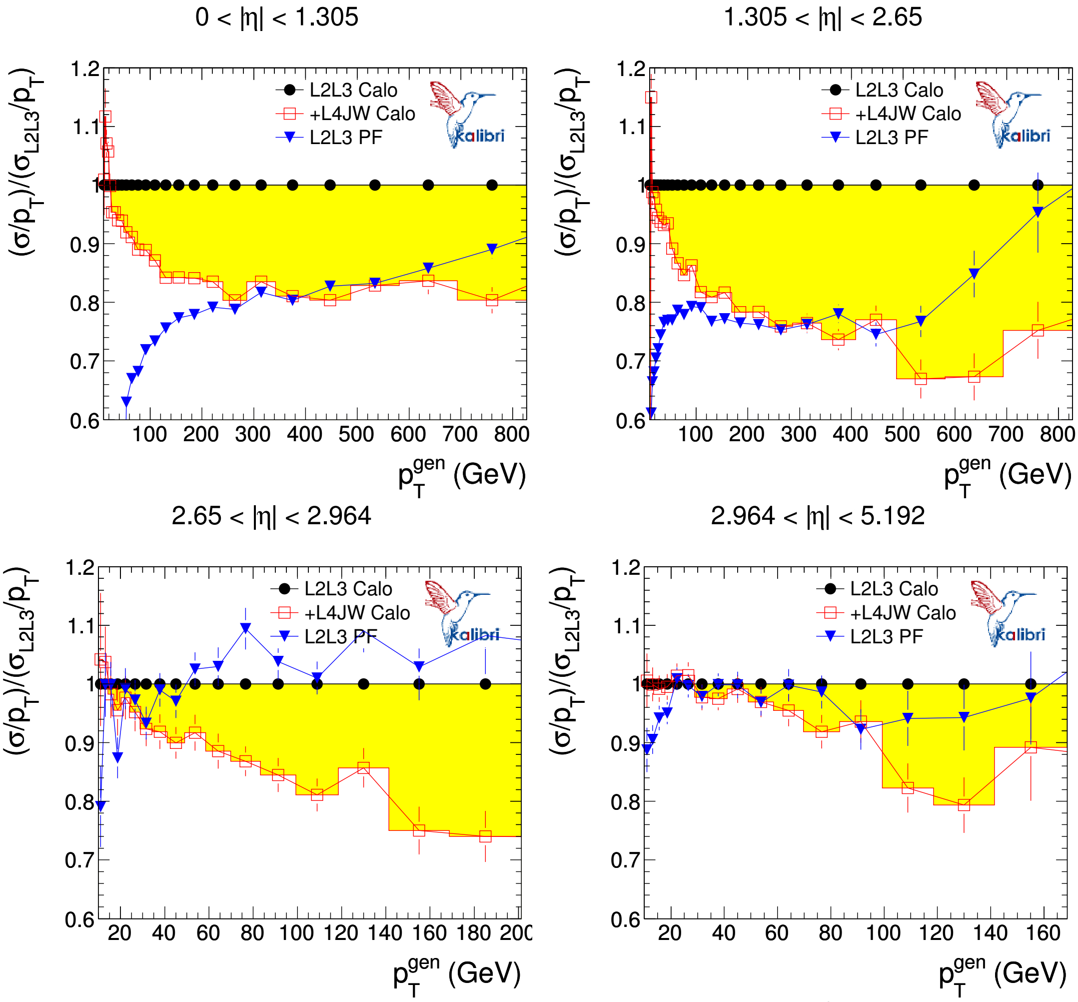

Figure 7.5.: Relative resolution scaled to the relative resolution after L2L3-correction (i.e. resolution improvement) as a function of p_T^{gen} in different η-bins (black circles: L2L3-correction; blue triangles: L2L3-corrected PF-jets; red open squares: JW-correction).

expected error and is calculated as:

$$\sigma_{\frac{N}{D}} = \sqrt{\frac{\sigma_N^2}{D^2} + \frac{N^2 \cdot \sigma_D^2}{D^4}} \tag{7.1}$$

For jets with a p_T^{gen} of more than ≈ 50 GeV a significant resolution improvement is observed for jet-width-corrected calorimeter jets in all detector regions, most prominent in the barrel and endcaps, where the resolution is improved by up to 20-30% as indicated by the filled area. This coincides with the results from the preliminary study in Section 5.5.2, where the jet-width correction significantly improved the jet-energy resolution. In comparison to the PF-jets, it is observed that the resolution of jet-width-corrected calorimeter jets is close to the energy resolution of PF-jets at $p_T^{gen} \approx 300$ GeV in the barrel region and p_T^{gen} as low as ≈ 100 GeV in the endcap region. Presently, there are considerations to take a jet-width correction into account for PF-jets as well. This is particularly interesting when the more forward detector regions are explored, where no tracking system is available for the particle flow approach. This is shown in the two lower plots where no significant resolution improvement can be achieved when using PF-jets, but the jet-width correction is still functional.

7.4. Flavour difference

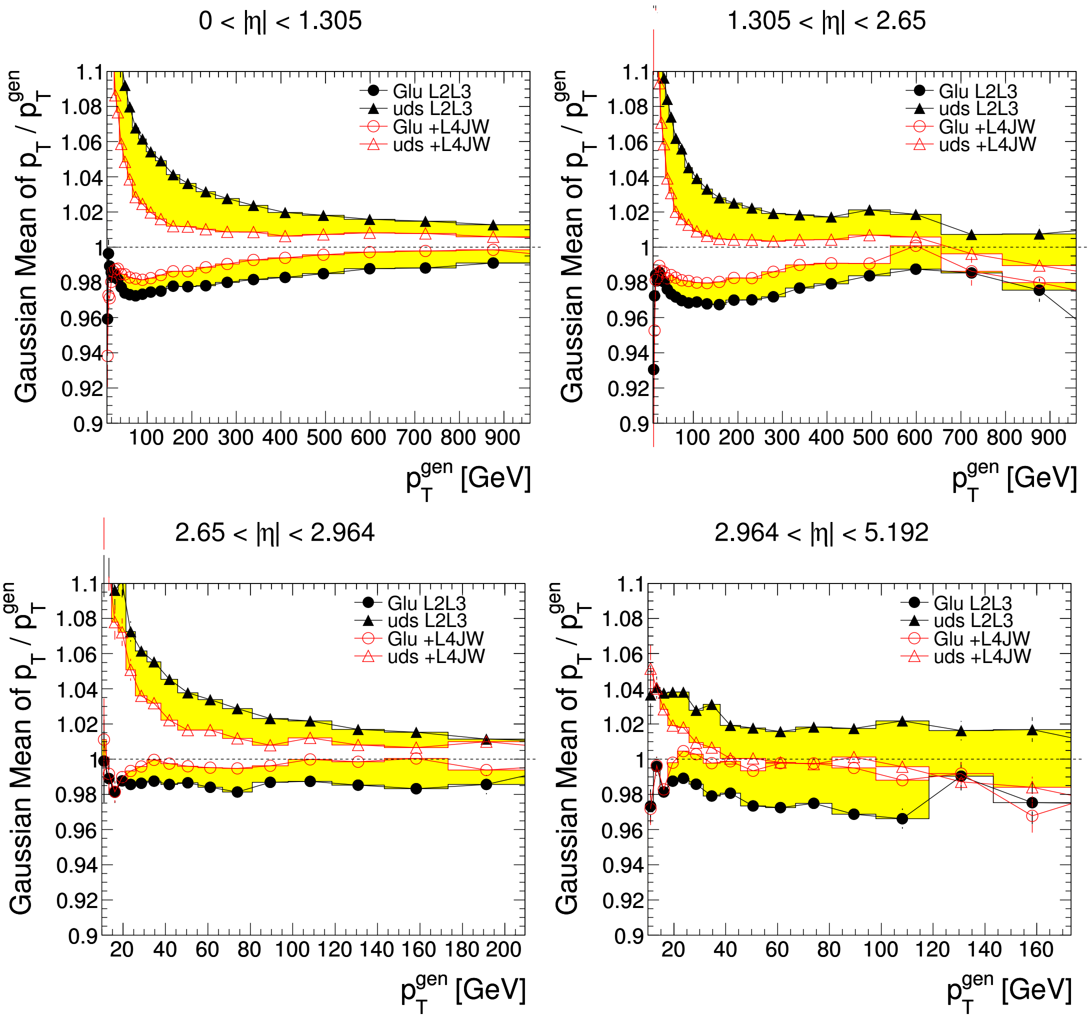

Figure 7.6.: The Gaussian mean response of gluon and light quark jets as a function of p_T^{gen} before and after jet-width correction in different η-bins (black circles: Gluons, L2L3; black triangles: uds, L2L3; red open circles: Gluons, L2L3+JW-correction; red open triangles: uds, L2L3+JW-corrected).

It is one of the goals of the jet-width correction to decrease the dependence of the mean jet response on the flavour, as this allows to reduce the correction factors of the flavour specific jet-energy corrections (L5). With smaller L5 correction factors, the systematic uncertainty on the jet-energy scale for analyses with a flavour composition other than that of the simulated QCD data sample can be lowered significantly (see Section 4.3.4).

In Figure 7.6, the mean jet response is shown for gluon and light quark jets. For jets to which the jet-width correction has been applied, the mean jet response is much closer to one over a wide p_{T}-range. The filled area indicates this improvement. The decrease of the response difference for gluon and light quark jets has been discussed in Chapter 5 and the corresponding plot is shown in Figure 7.7. As a consequence of Figure 7.6, the flavour difference is decreased significantly in all four η-regions for calorimeter jets. This effect is

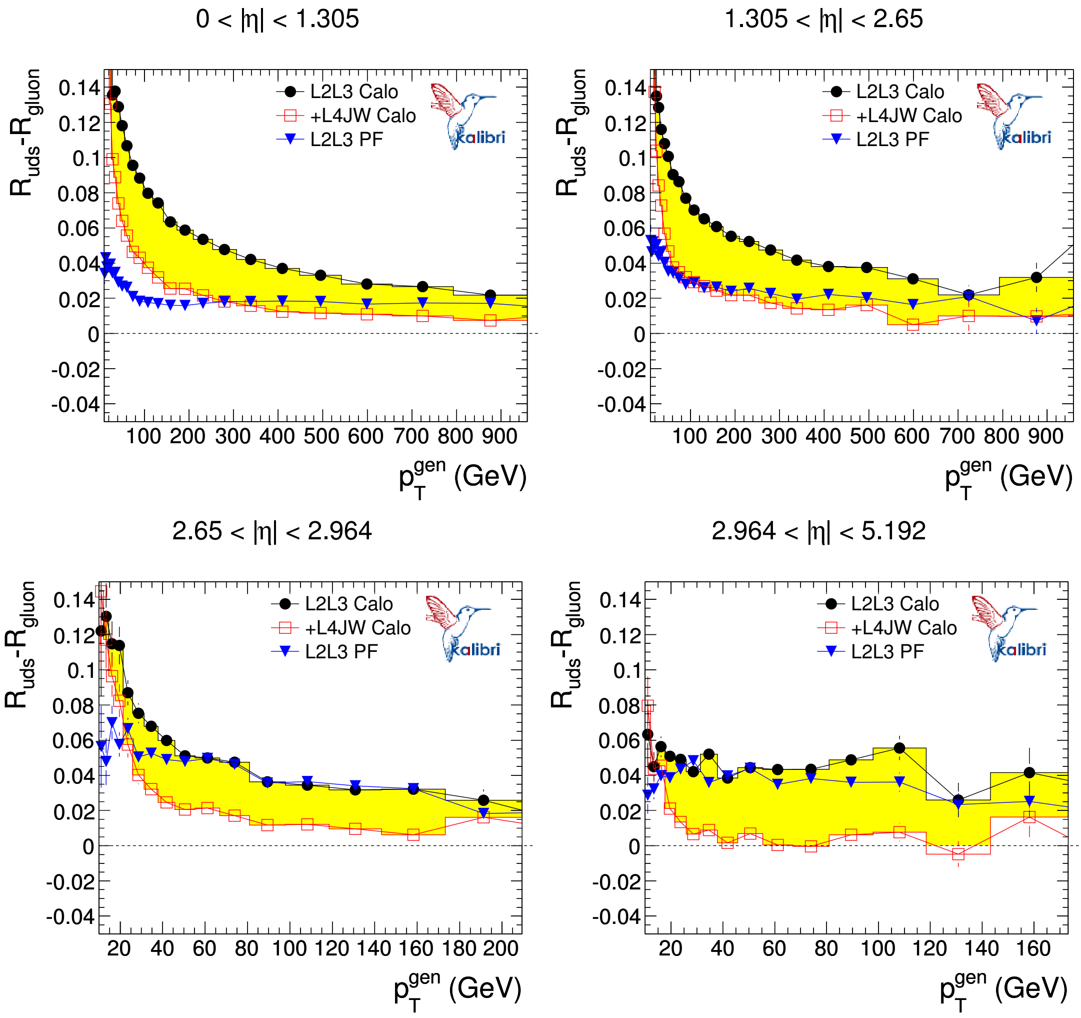

Figure 7.7.: The difference of the separately determined Gaussian mean response of gluon and light quark jets (see Figure 7.6) as a function of p_T^{gen} before and after jet-width correction in different η-bins (black circles: L2L3-correction; blue triangles: L2L3-corrected PF-jets; red open squares: JW-correction). After the jet-width correction, the flavour differences are largely reduced.

already observed for calorimeter jets with low transverse momenta and is indicated with the filled area between L2L3-corrected CaloJets and subsequently jet-width-corrected CaloJets. PF-jets intrinsically have a lower dependence on the flavour of the jet in the pseudorapidity region covered by the tracker as the different particle multiplicity and p_{T}-spectrum of light quark and gluon jets are already partially compensated for by identifying individual particles. However, applying the jet-width correction to calorimeter jets reduces the difference of the flavour responses to a level competitive or superior to the particle flow approach for p_T^{gen}above 250 GeV. In the forward regions, the flavour response difference is almost fully compensated by the jet-width correction.

Considering the large effects in terms of resolution improvement and decreasing the flavour dependence of the mean jet response – even in comparison to particle flow – the jet-width results on Monte Carlo are very promising and could – in the future – help to improve the good performance of PF-jets as well.

Chapter 8.

Evaluation on experimental data

In this section, the performance of the jet-width correction is evaluated on data using the dijet balance method. This method is extensively discussed in [105] and was originally developed to determine the relative correction L2 in the factorised jet-energy-correction approach in CMS from data. As no direct handle on the flavour of a single jet is available, the focus of this evaluation is on the comparison of data and predictions from simulated data and on the resolution improvement.

8.1. Technicalities

The following event samples were reconstructed using the CMS software and have been used for the validation of the proposed jet-width correction:

- Data sample
  - `JetMET_Run2010A-Nov4ReReco-v1 (141950-144114)`
  - `HLT DiJetAve50U`, 2.896 pb^{-1}
  - standard cleaning filters recommended for data analysis are applied [1]
  - Spring10 + residual corrections V2 applied
- MC sample
  - `/QCDDiJet_PtXXtoXX/Spring10-START3X_V26_S09-v1/GEN-SIM-RECO`
  - Spring10 corrections

The specific dijet trigger `HLT DiJetAve50U` is discussed in [105]. It triggers, when a certain threshold of

$$p_T^{ave} = \frac{p_T^{probe} + p_T^{barrel}}{2} \tag{8.1}$$

---

[1] Good-Vertex filter, Beam-Scraping-Event filter

is surpassed, where p_T^{barrel} stands for the transverse momentum of a jet in the barrel region ($|\eta| < 1.3$) and p_T^{probe} for the p_T of a second jet. Using this trigger, a large amount of data with unbiased dijets, tailored for the dijet balance method, can be recorded.

In all these events, the two calorimeter jets with the highest transverse momentum are considered for further analysis. The jet-finding algorithm is anti-k_t with a cone-size parameter of $R = 0.5$. The jets are required to pass quality criteria in order to reject jets clustered from calorimeter noise (see [103]). Dijets are selected by requiring the jets to be back-to-back in the transverse plane. This is done by cutting on the opening angle between the two leading jets $\Delta\varphi(j_1, j_2) > 2.7$. Additional jet activity is suppressed by a cut on the p_T of the third-leading jet of $p_{T,j_3} < 0.2 \cdot p_T^{ave}$.
In order to extract meaningful information from these event topologies, the asymmetry,

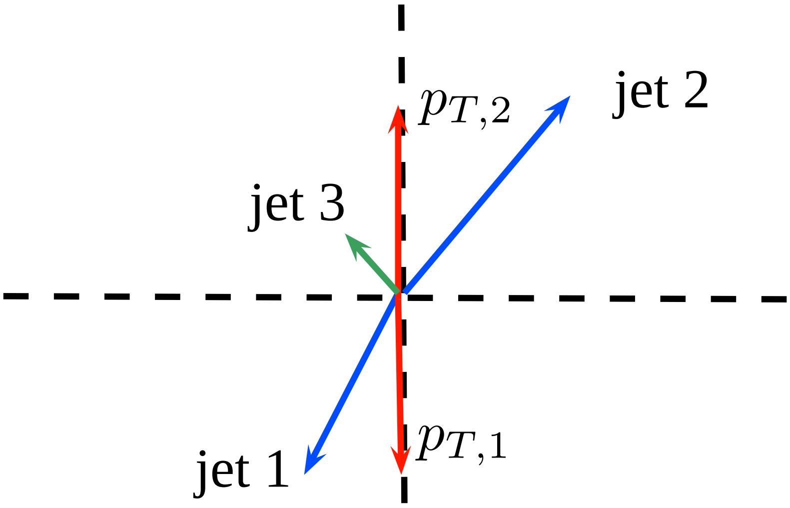

Figure 8.1.: Dijet topology: The momenta of the two back-to-back jets are projected to the transverse plane. Cuts on additional jet activity improve the balance.

A, and the relative response, R, are introduced:

- $A = \frac{p_T^{probe} - p_T^{barrel}}{p_T^{probe} + p_T^{barrel}}$,
- $R = \frac{1+\langle A\rangle}{1-\langle A\rangle}$

These measures are defined to relate the detector response in the barrel region, which can be best calibrated in-situ, to the detector response in other detector regions. Both leading jets are allowed to serve as barrel (tag) jets, if they fulfil $|\eta| < 1.3$.
In this analysis, the relative response and asymmetry are examined in bins of p_T^{ave}. The asymmetry is minimally biased due to the binning in p_T^{ave}. The same is valid for the relative response calculated from the asymmetry. It is claimed to be the least biased estimator in contrast to the ratio p_T^{probe}/p_T^{barrel} for evaluating the response in dijet events as discussed in [106], where the method is introduced for use within the CMS collaboration.

The variance of the asymmetry A is given by

$$\sigma_A^2 = \left|\frac{\partial A}{\partial p_T^{probe}}\right|^2 \cdot \sigma(p_T^{probe})^2 + \left|\frac{\partial A}{\partial p_T^{barrel}}\right|^2 \cdot \sigma(p_T^{barrel})^2 \tag{8.2}$$

For $p_T = p_T^{probe} = p_T^{barrel}$ and $\sigma(p_T) = \sigma(p_T^{probe}) = \sigma(p_T^{barrel})$, this simplifies to

$$\frac{\sigma(p_T)}{p_T} = \sqrt{2}\sigma_A, \tag{8.3}$$

i.e. σ_A is proportional to the jet-energy resolution. However, this is in fact only valid for the ideal situation without additional jet activity. In reality, the width of the asymmetry is always broader as additional jets and the underlying event distort the perfect dijet balance.

8.2. Jet width in data

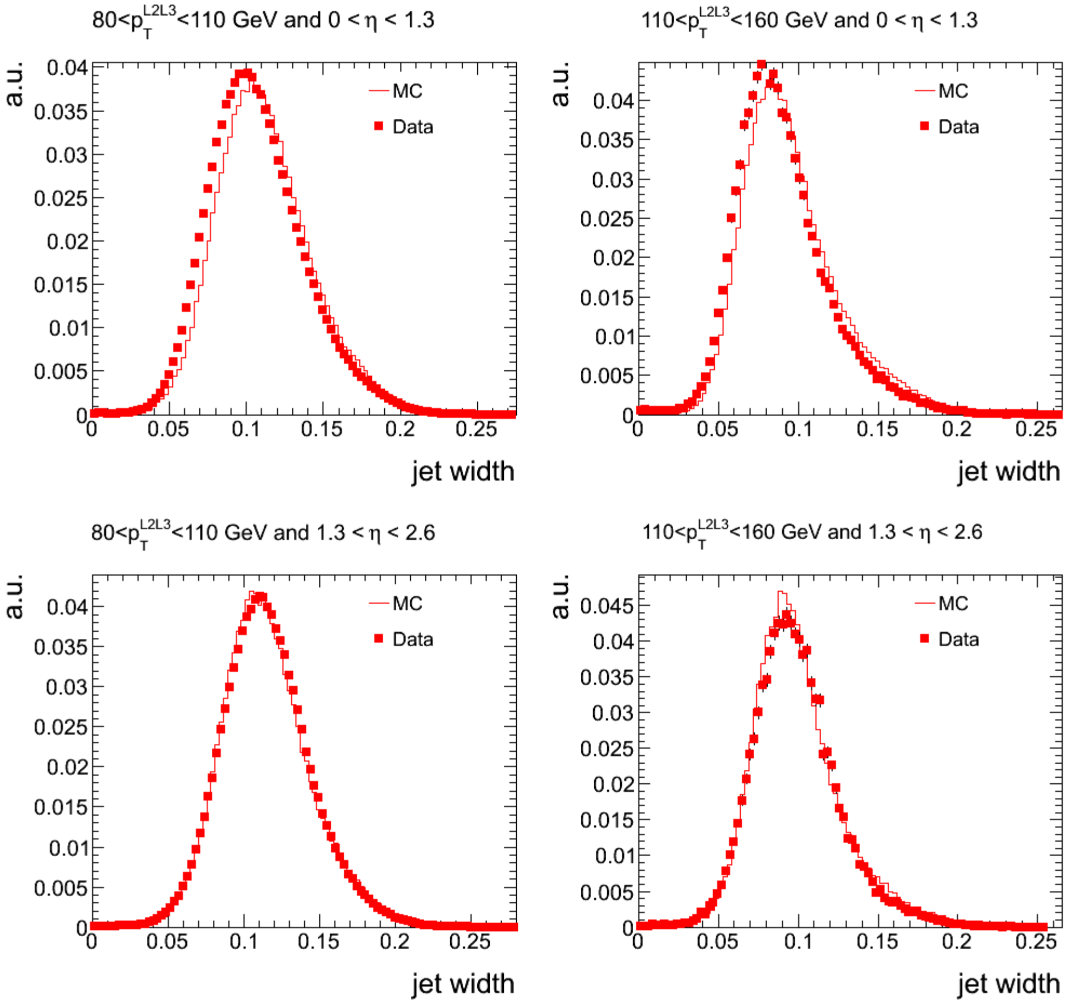

Figure 8.2.: Upper two plots: Jet width in bins of p_T^{L2L3} in the barrel region.
Lower two plots: Jet width in bins of p_T^{L2L3} in the endcap region.
red line: MC; red squares: Data.

The jet-width correction as described in Chapter 6 has been derived on simulated data. For the correction to be applicable to data, the description of the jet width has to be compatible in simulations and data. In the upper two plots of Figure 8.2, the distribution of the jet width is shown for the barrel in two different p_{T}-regions for simulations and data. The shape of the jet-width distribution is modelled relatively well, only a very slight shift of the peak can be observed. In the two lower plots, the distribution of the jet width is shown in the endcap region. A relatively good agreement can be observed here as well. In the following sections, it is investigated whether the MC-description of the the jet width and its correlations with other variables is sufficient for the jet-width correction in the current form to be applicable to data.

8.3. Relative response vs. η in p_{T}-ranges

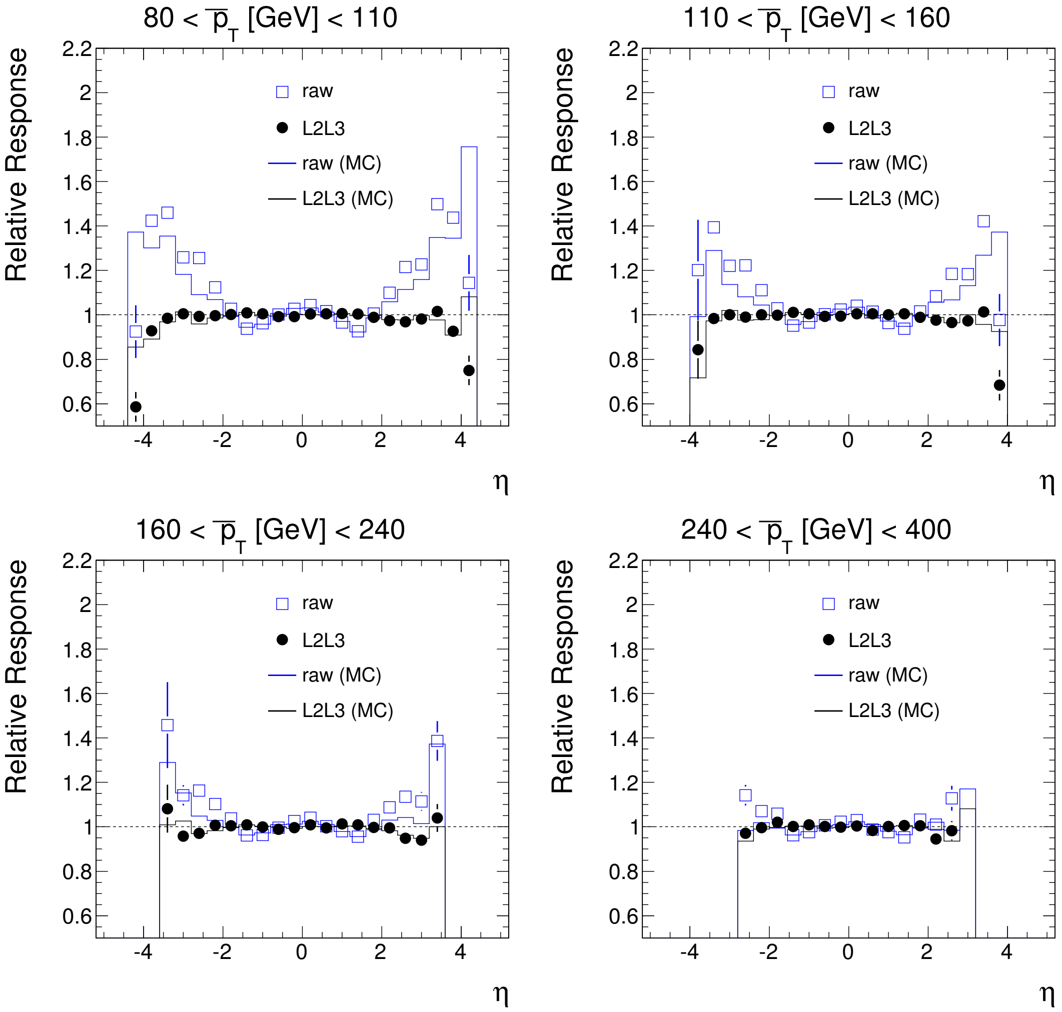

Figure 8.3.: Relative response as a function of the pseudorapidity η in different p_T^{ave}-regions (blue line: raw MC; black line: L2L3 MC, blue open squares: raw data, black circles: L2L3 data).

Raw vs. L2L3: In Figure 8.3, the relative response is shown as a function of η in different p_T^{ave}-bins. The uncorrected jets show a strong η-dependence as the L2-correction (see Section 4.3.2) has not yet been applied. The L2L3-corrected jets show a relative response very close to unity, i.e. there is no strong response difference for a tag-jet in the barrel region and a probe jet in an arbitrary η-region (even though the absolute response could in principle be quite different from unity). The simulation describes the response dependence of L2L3-corrected jets very well, but does not agree with the data for uncorrected jets in the forward regions. This has been established before and has lead to a residual correction on top of the L2L3-correction that has been applied to the L2L3-jets as shown here (see Section 4.3.5).

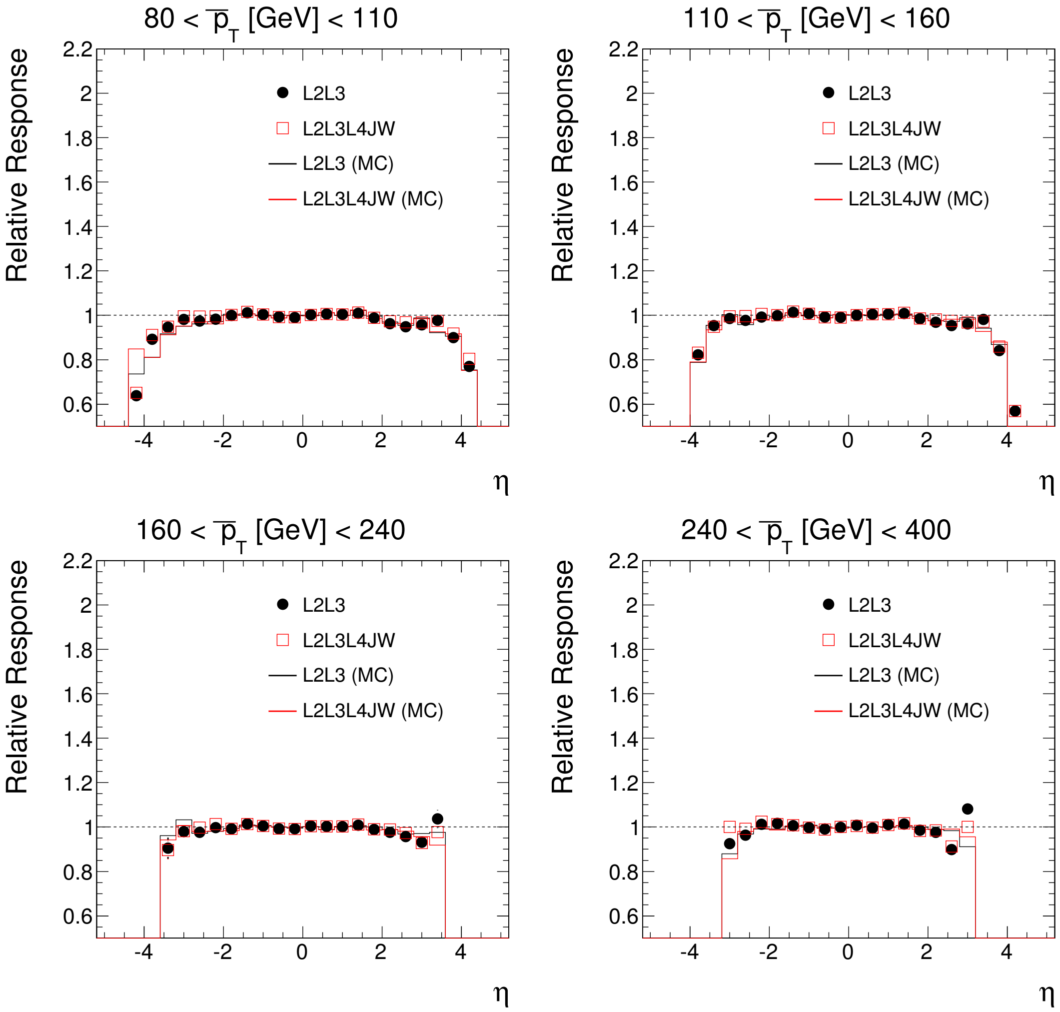

Figure 8.4.: Relative response as a function of the pseudorapidity η in different p_T^{ave}-regions (black line: L2L3 MC; red line: +L4JW MC, black circles: L2L3 data, red open circles +L4JW data).

L2L3 vs. jet-width correction: Figure 8.4 depicts the η-dependence of the relative response for calorimeter jets after the L2L3-corrections and for calorimeter jets to which the jet-width correction has been applied. For all p_{T}-regions, the value of the relative response remains approximately the same after a subsequent jet-width correction as a function of η. This is a good indicator that the construction of the jet-width correction (as given in Section 6.2) to preserve the energy scale worked well.

8.4. Relative response vs. jet width

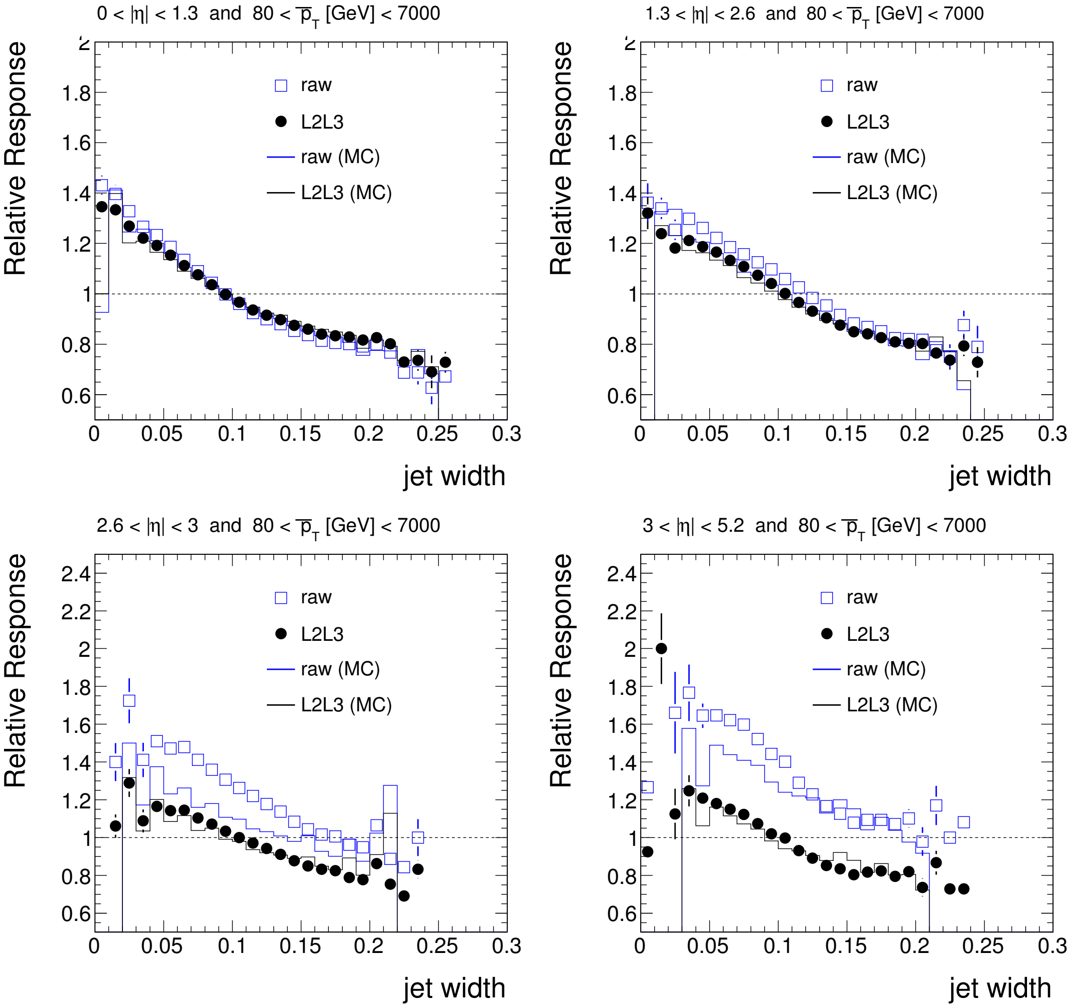

Figure 8.5.: Relative response as a function of the jet width in different η-bins (blue line: raw MC; black line: L2L3 MC, blue open squares: raw data, black circles: L2L3 data).

Raw vs. L2L3: In Figure 8.5, the relative response is shown as a function of the jet width in different η-bins. As expected, the L2L3-corrections do not correct for the response dependence on the jet width. The slope remains almost the same after the application of the L2L3-correction and supports the hypothesis that a jet-width correction is only very weakly correlated with the previous correction steps. For the barrel region, a very good agreement between simulation and data is observed. As expected (and observed in Section 8.3), the simulation underestimates the relative response for the forward regions, if no residual correction is applied. However, simulations and data agree for the L2L3-corrected jets, to which a residual correction was applied.

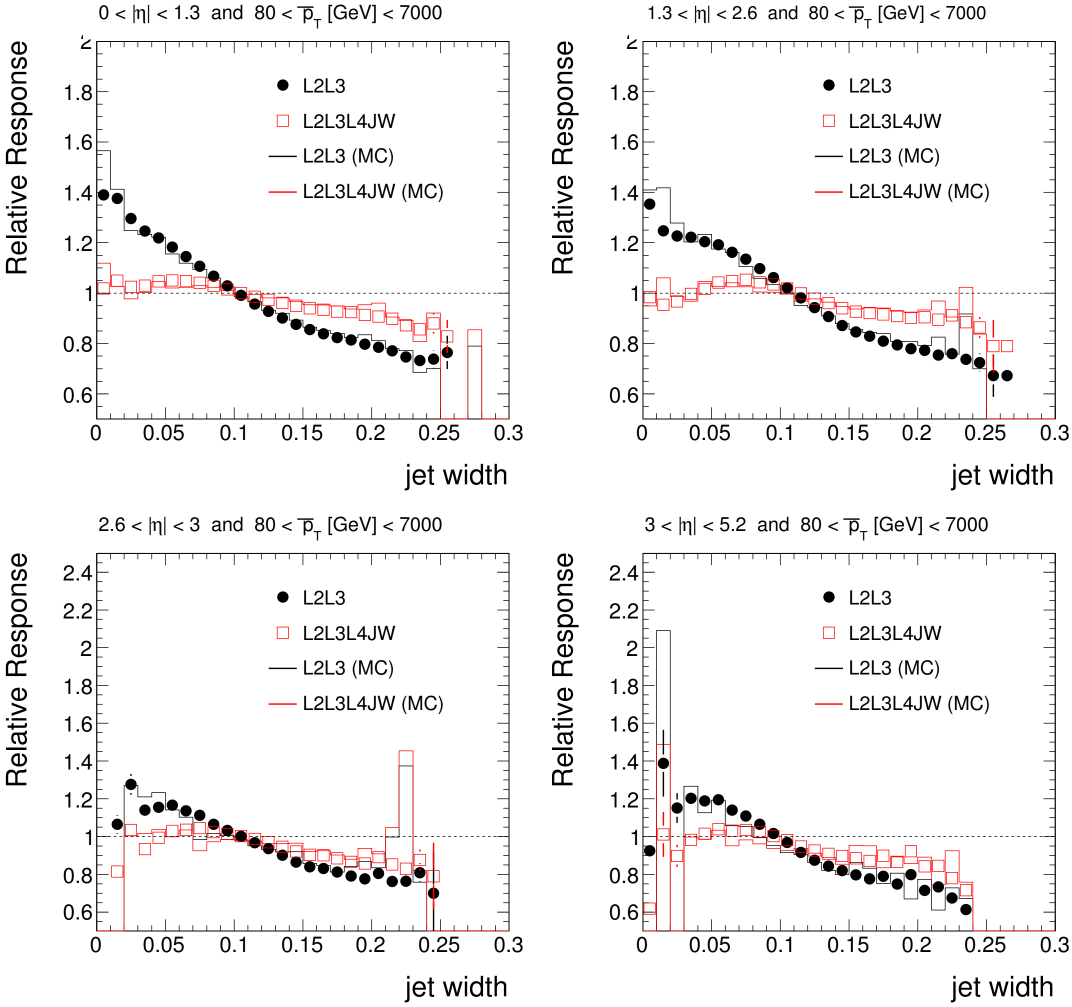

Figure 8.6.: Relative response as a function of the jet width in different η-bins (black line: L2L3 MC; red line: +L4JW MC, black circles: L2L3 data, red open circles: +L4JW data).

L2L3 vs. jet-width correction: Figure 8.6 illustrates the effect of the jet-width correction. The dependence of the relative response on the underlying variable, the jet width, should be mostly removed when the jet-width correction is subsequently applied to the L2L3-corrected jets. Indeed, the dependence is clearly decreased in all four η-regions which promises an improved energy resolution. In comparison to the results in Section 7, the relative response is not flat as a function of the jet width. Nevertheless, a very good agreement between simulation and data is seen and as the dependence of the response on the jet width vanished on simulations (see Section 7), the remaining dependence can be related to biases due to the resolution similar to those discussed in [105] and to the additional jet activity (dependence vanishes for very strict cut on p_{T,j_3}, not shown here).

8.5. Resolution improvement

Width of asymmetry: The width of the asymmetry is depicted in Figure 8.7. Here, it is used as an estimator for the jet-energy resolution (see Section 8.1). The width of the asymmetry is decreased significantly in all four η-regions. This suggests that the jet-energy resolution has been improved. The decrease of the width is of the same order of magnitude in data and in the simulation, but it is systematically underestimated by the simulation. This systematic effect has been observed in other studies as well and is under study within the CMS collaboration [108]. Considering the direct comparison with the jet-energy resolution obtained from simulations (see Chapter 7), it has to be stressed that this needs careful examination. There is a significant contribution to the width from additional jet activity (3rd and even softer jets) that adds in quadrature

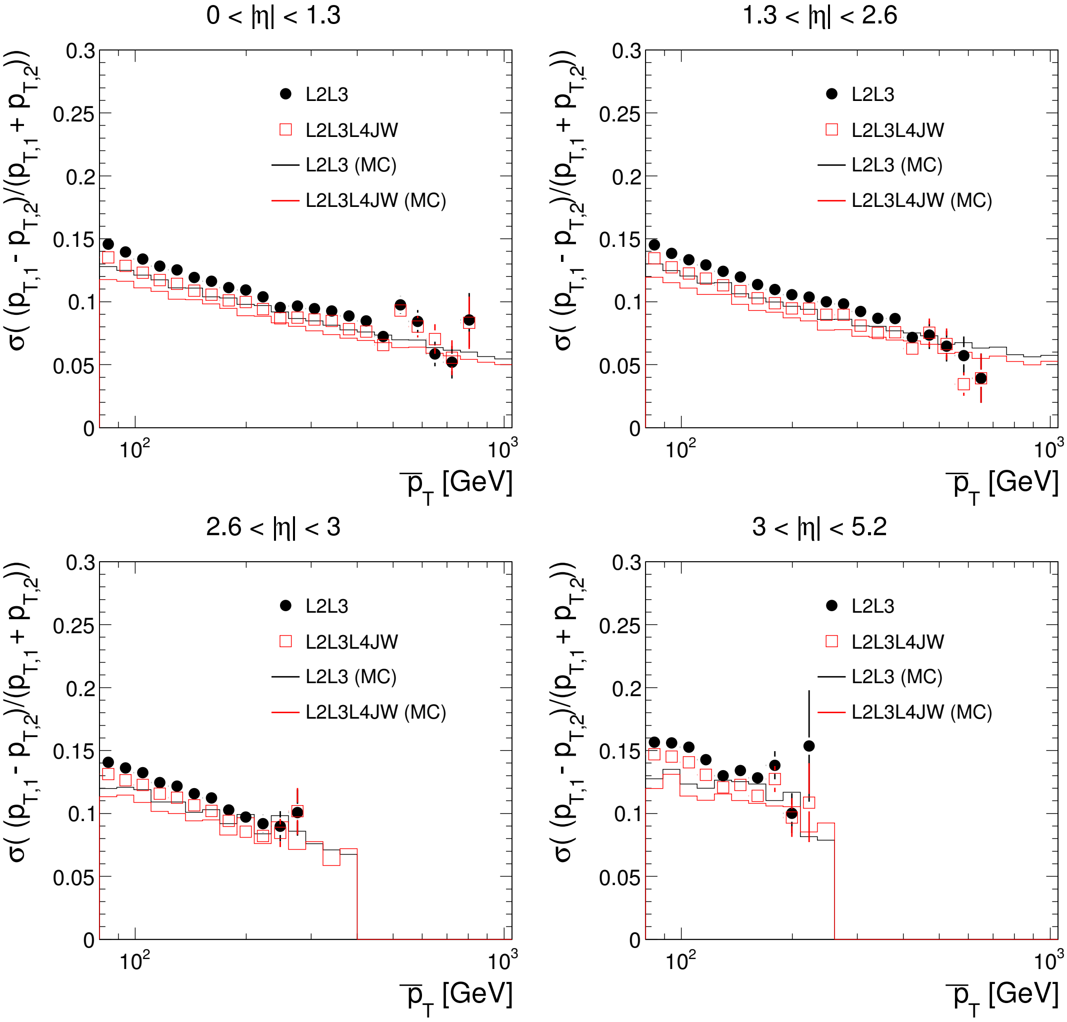

Figure 8.7.: Width of the asymmetry as a function of p_{T} in different η-bins (black line: L2L3 MC; red line: +L4JW MC, black circles: L2L3 data, red open circles +L4JW data).

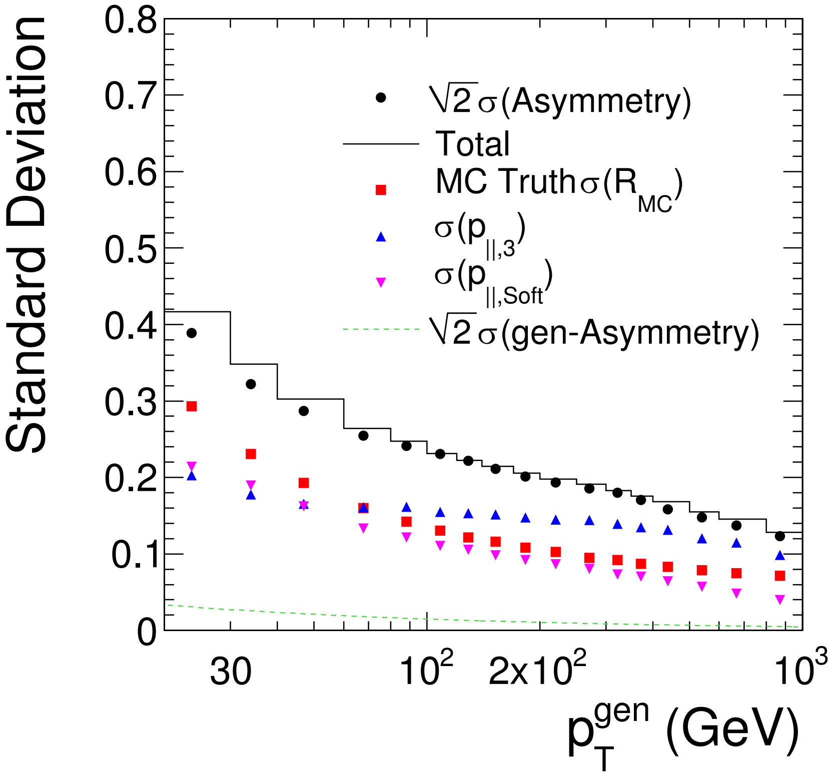

Figure 8.8.: Simulation of the expected contributions to the observed asymmetry in imperfect dijet events due to additional jet activity (see [107]). $\sqrt{2}\sigma$(Asymmetry): width of the asymmetry as determined from the reconstructed two leading jets in the dijet topology multiplied with the factor $\sqrt{2}$, compare Section 8.1; Total: the quadratic sum of the following contributions; MC Truth $\sigma(R_{MC})$: energy resolution determined from reconstructed simulated jets as in Chapter 7; $\sigma(p_{||,3})$: resolution of the projection of p_{T,j_3} along the dijet-axis; $\sigma(p_{||,soft})$: resolution of the projection of the p_{T} of all soft jets along the dijet-axis; $\sqrt{2}\sigma$(gen-Asymmetry): width of the asymmetry as determined from the generator particle level. Figure is taken from and discussed in detail in [107]

to the square root of widths. Here, the the transverse momentum of the third jet was required to be below 20% of p_T^{ave}. The intrinsic resolution (i.e. what is known from the study on simulated data in Figure 7.4) forms only a part of the full observed width of the asymmetry. A detailed consideration of the different contributions is shown in Figure 8.8 and is discussed in [107].

Width of asymmetry relative to the L2L3 width of the asymmetry: Figure 8.9 shows the width of the asymmetry relative to the value of L2L3-corrected jets, i.e. the relative improvement. The width is decreased by approximately 10% by the jet-width correction in all four η-regions. In comparison to Figure 8.7, a very good agreement of the simulation and the data can be stated.

Dependence on the p_{T,j_3}-cut: The resolution improvement of approximately 10% as shown in Figure 8.9 does not translate directly to the improvement of the energy resolution

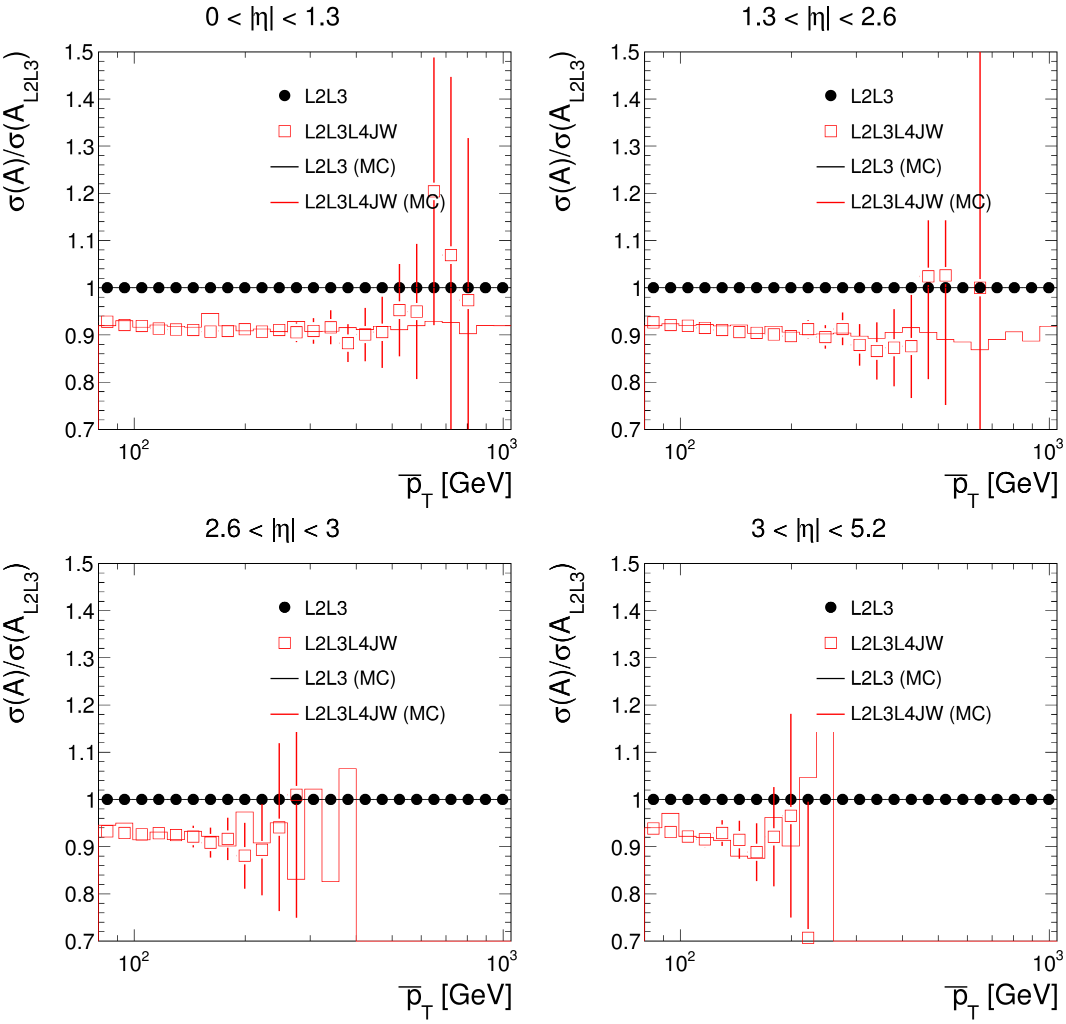

Figure 8.9.: Width of the asymmetry as a function of p_{T} in different η-bins, scaled to the width of the asymmetry after L2L3-corrections (black line: L2L3 MC; red line: +L4JW MC, black circles: L2L3 data, red open circles: +L4JW data).

determined in Section 7.3. Instead, it is a convolution of the different contributions to the width of the asymmetry as depicted in Figure 8.8. A proper extrapolation to zero jet activity, as carried out in [109], would be needed to compare the results here and in Section 7.3 quantitatively. However, the amount of data recorded during the 2010 run of LHC is still limited. In order to qualitatively compare the improvement with the results from the study on simulated data, the p_{T,j_3}-cut has been varied. In Figure 8.10, the width and the relative improvement are shown with a loosened requirement and a tightened requirement on the additional jet activity by varying the p_{T,j_3}-cut. The width of the observed asymmetry decreases for a tightened p_{T,j_3}-cut and the relative improvement, as shown in the plots on the right hand side, increases with decreasing additional jet activity. For means of comparison, a horizontal line is plotted on the right hand side at $\sigma(A)/\sigma(A_{L2L3}) = 0.92$. One can see that the relative improvement increases slightly for a tightened cut on additional jet activity, but that the limited amount of simulated data and data makes the phase space with even less additional jet activity inaccessible. Nevertheless, the very good overall agreement between simulation and data (except for the previously discussed absolute value of the width of the asymmetry) and the results of the study on simulated data in Chapter 7 suggest that the relative improvement of the jet-energy resolution seen in simulations applies to data as well.

8.6. Flavour response

No direct conclusions can be drawn with respect to the flavour dependence of the mean jet response. In simulated data, a strong correlation of the jet width with the response and with the jet-flavour was observed (see Figure 5.18(c) and Figure 5.19). In data, the correlation of the relative response and the jet width was significantly decreased as depicted in Figure 8.6. A good agreement between simulations and data for this dependence is observed. This can be regarded as an indicator for the reduction of differences in the mean jet response for the various flavours in data.
Studies on event topologies with a flavour composition other than that in the QCD simulation as well as gluon and uds-quark identification algorithms are needed to fully establish the results on the mean jet response for different jet-flavours observed in simulations and validate the positive effect of the jet-width correction on data.

a.) $p_{T,j_3} < 0.3$

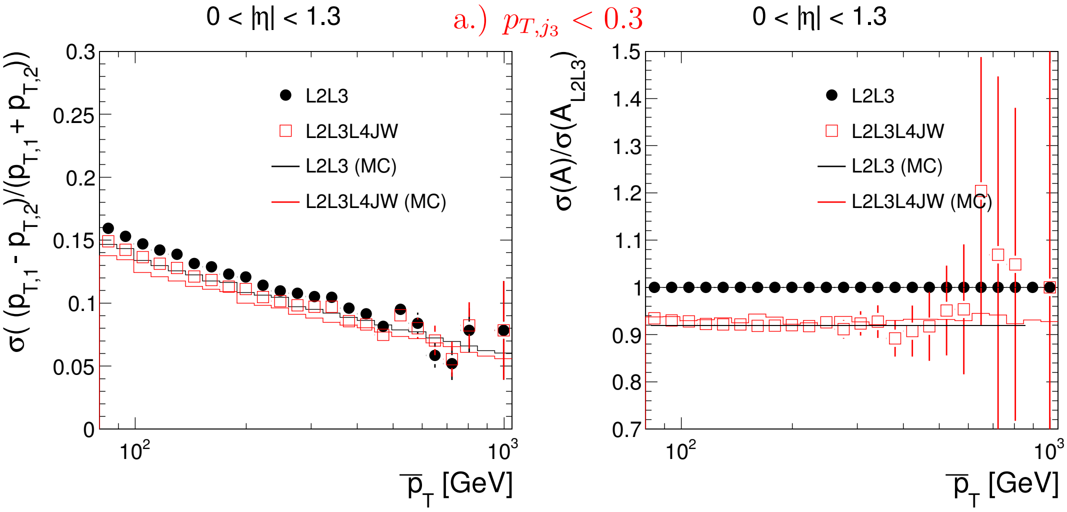

b.) $p_{T,j_3} < 0.2$

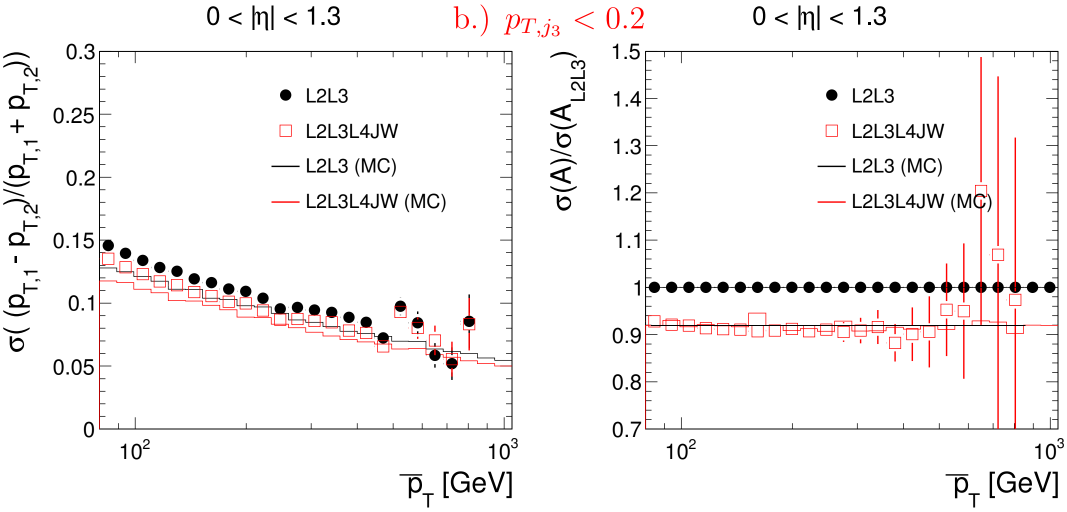

c.) $p_{T,j_3} < 0.1$

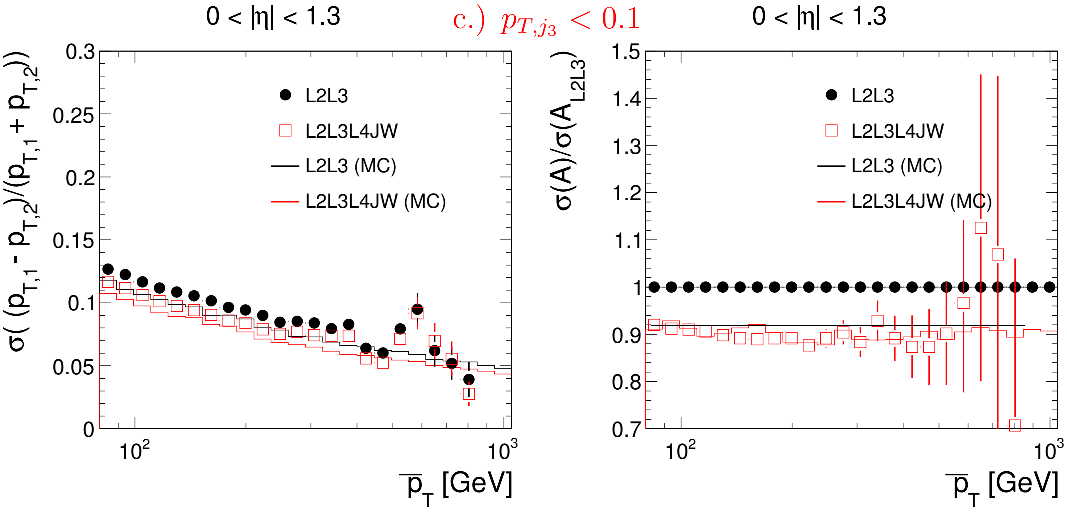

Figure 8.10.: Width of the asymmetry as a function of p_{T} in the barrel region for different p_{T,j_3}-cuts. Left: Width of the asymmetry; right: Width of the asymmetry scaled to the asymmetry after L2L3-correction. Horizontal line set to 0.92 for comparison (black line: L2L3 MC; red line: +L4JW MC, black circles: L2L3 data, red open squares +L4JW data).

Chapter 9.

Conclusions and outlook

A strong dependence of the mean jet-energy response on the jet-flavour is observed for calorimeter jets. Therefore, a study for a jet-energy correction in addition to the currently recommended jet-energy corrections of CMS has been performed. This additional correction is expected to decrease the flavour dependence and improve the jet-energy resolution.

Due to the non-linear response of the CMS calorimeters, there is a dependence of the jet response on the momentum spectrum of the jet constituents and their radial distribution. For these quantities differences between quark and gluon jets are expected and could explain the dependence of the response on the jet-flavour. In order to determine a well-defined and well-behaved correction procedure, various observables, defined from measured calorimeter energy depositions, and their correlation with the jet response have been studied using simulated data. If the correlation of the observables and the response is corrected for, an improvement of the jet-energy calibration is expected. In the barrel region, corrections using variables, that are based on the determination of the electromagnetic fraction of the jet as a whole or individually on the tower level, showed a slight improvement of the jet-energy resolution of approximately 5 % and a slight decrease of the flavour dependence of about 15-20 % at p_T^{L2L3} =100 GeV (see Section 5.4). In contrast to this, corrections using variables, that are based on the spatial distribution of energy depositions in the calorimeters within a jet, performed better, especially for higher p_{T}. A bin-by-bin correction using the $\sigma_{\eta\eta}$-moment or $\sigma_{\varphi\varphi}$-moment showed a considerable improvement with respect to the jet-energy resolution (15-20 % at p_T^{gen}above 100 GeV) and the flavour dependence of the jet response is reduced by 20 % at 30 GeV and up to 50 % at 300 GeV.

Several combinations of $\sigma_{\varphi\varphi}$ and $\sigma_{\eta\eta}$ have been tested in Section 5.5 in order to determine a variable with a maximum correlation with the jet response. The mean value of both,

$$\text{jet width } JW = \frac{\sigma_{\varphi\varphi} + \sigma_{\eta\eta}}{2} \tag{9.1}$$

showed the best performance using bin-by-bin corrections and was chosen for the development of an elaborated correction.

Based on simulated data, a parametrisation was developed in Chapter 6 and correction factors were derived using the Kalibri framework, which allows an unbinned fit of the correction factors (see Section 4.3.6). The validation of the parametrised correction on

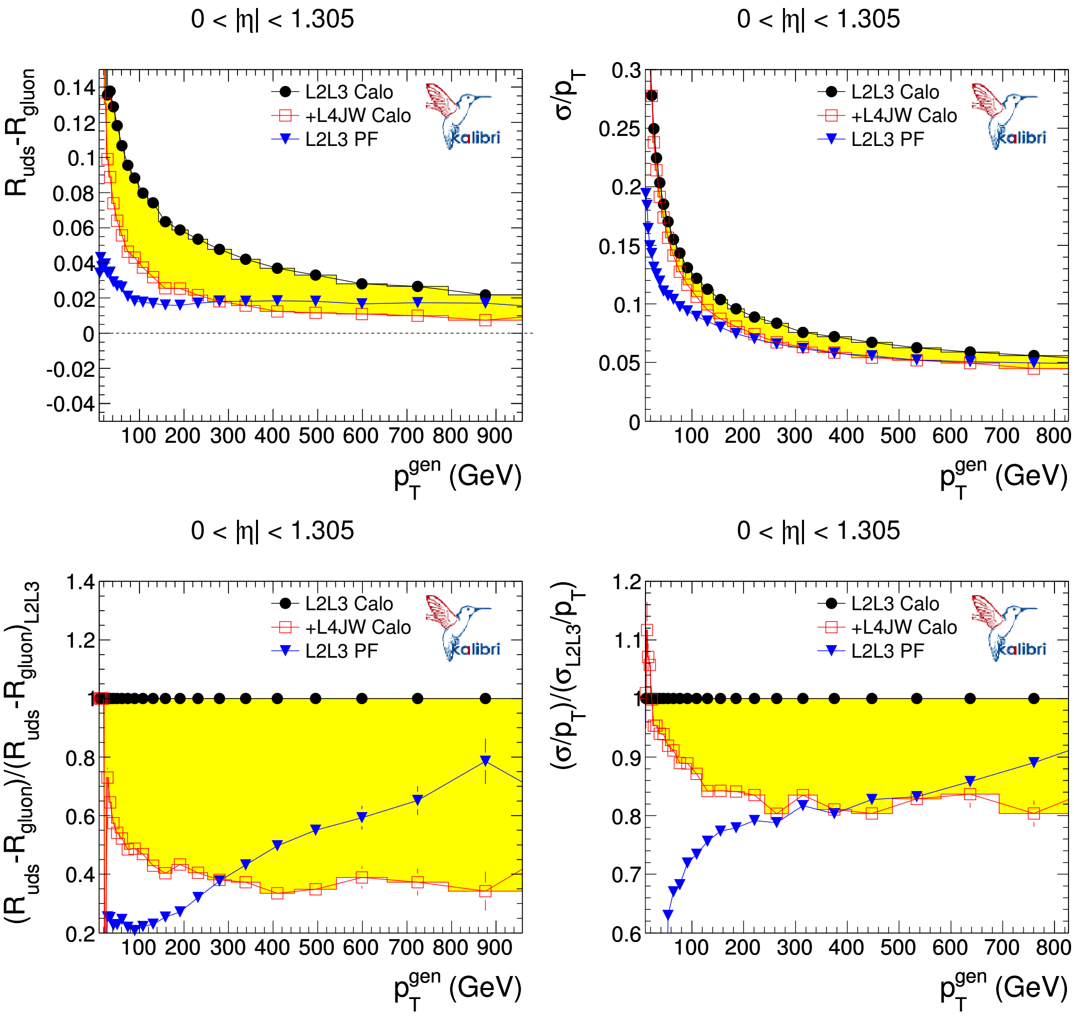

Figure 9.1.: Upper left plot: Difference of the mean response of gluon and light quark jets as a function of p_T^{gen} in the barrel region.
Upper right plot: Relative resolution as a function of p_T^{gen} in the barrel region.
Lower left plot: Difference of mean response of gluon and light quark jets scaled to the difference for L2L3-corrected calorimeter jets as a function of p_T^{gen} in the barrel region.
Lower right plot: Relative resolution scaled to the relative resolution after L2L3-correction (i.e. resolution improvement) as a function of p_T^{gen} in the barrel region. (black circles: L2L3-correction; blue triangles: L2L3-corrected PF-jets; red open squares: JW-correction).

simulated data in Chapter 7 yields an improvement of the energy resolution of up to 30% for jets in $1.305 < |\eta| < 2.65$ and a transverse momentum above 400 GeV. In the barrel region, the energy resolution is improved by $\approx 20\,\%$ for jets with a tranverse momentum above 250 GeV. An improvement of the resolution of more than $10\,\%$ is observed in all pseudorapidity regions for p_T^{gen}above 50-80 GeV. Concerning the difference of the mean jet response for gluon and light quark jets, the effect is decreased drastically over a wide

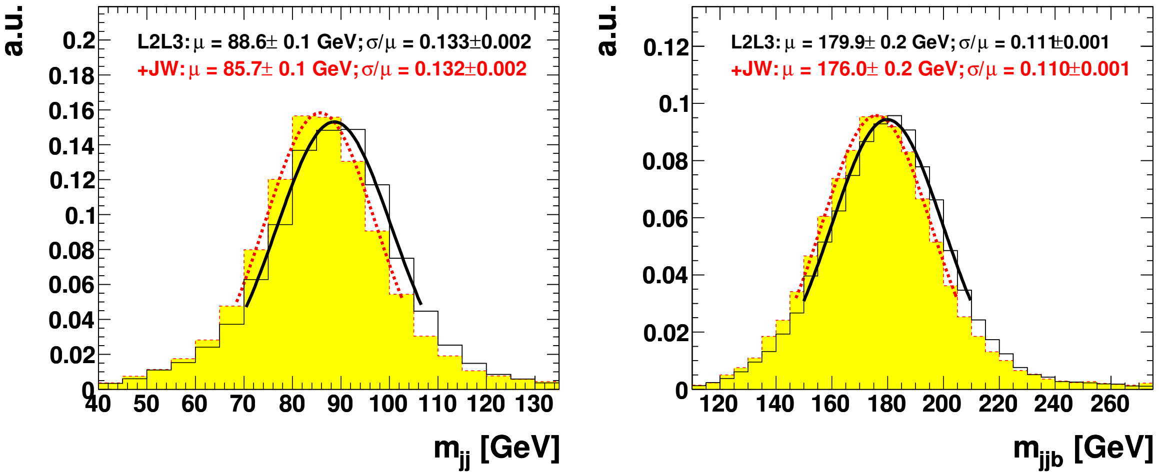

Figure 9.2.: Left plot: Two jet invariant-mass distribution of hadronically decaying W-bosons originating from top-quark decays.
Right plot: Three jet invariant-mass distribution of hadronically decaying top quarks.

p_T^{gen}-range. In the barrel region, the dependence is decreased by approximately 35-40 % for jets with $p_T^{gen} \approx 40$ GeV and decreased by about 60 % for jets with $p_T^{gen} \approx 300$ GeV. In forward regions and for very high p_T, the flavour dependence vanishes almost completely. The effects on simulated data for the barrel region are summarised in Figure 9.1.

On data from the 2010 run, first results of the performance of the proposed jet-width correction (see Chapter 8) were obtained using the dijet balance method with varying cuts on the additional jet activity. The width of the asymmetry as an indicator of the energy resolution was decreased by approximately 10 % at a transverse momentum of about 100 GeV by the jet-width correction and a good agreement between simulations and data was observed. For a full evaluation of the effect on the energy resolution determined from data, a larger amount of data will have to be recorded and a quantitative extrapolation to zero additional jet activity is needed.

In the future, the application of the jet-width correction as a standard correction in addition to the L2L3-corrections is planned. A further generalisation of the correction, in order to be applicable to jets reconstructed using the particle flow approach, is possible and a thorough evaluation of the performance and uncertainties of the correction on data should follow.
It will be possible to estimate the improvement of the jet-energy resolution using established methods [110–112], including a correct extrapolation to zero additional jet activity. The determination of the influence on the flavour dependence of the response is hard to quantify in data, but studies on different event samples could indicate whether the

expected behaviour is also observed on data. The influence of the improved jet-energy resolution and the decrease of the flavour dependence on a variety of physics studies has not yet been studied in detail. Depending on the transverse momentum of the jets, evidence of the effects of the correction will vary.

A preliminary study of the influence of the jet-width correction on the reconstruction of hadronically decaying top quarks has been performed in [113] on simulated data with techniques described in [90]. The mean value of the invariant mass distributions for W-bosons and top quarks as depicted in Figure 9.2 is significantly closer to the expected value, when the jet-width correction is applied. The expected value is $\approx$ 82 GeV for the W-boson and $\approx$ 172 GeV for the top quark as discussed in [90]. This suggests that the influence of the flavour response has been reduced by about 50 % by the jet-width correction in this top-quark reconstruction. Due to the relatively low average transverse momentum of the involved jets, the width of the invariant mass distribution is not significantly decreased.

For physics studies involving jets with a high transverse momentum, such as the search for resonances in the dijet mass spectrum, it is expected that the full effect of the proposed correction on the energy resolution and the flavour dependence of the response becomes visible.

Appendix A.

Candidate variables for jet shape correction

In Table A.1, most candidate variables examined during the work for the thesis are documented. This list includes some additional variables not explicitly presented in this thesis. These variables did not show a significantly improved calibration or were examined for cross checks only.

Variable	Definition	Comment
EMF	$\frac{E_{ECAL}}{E_{ECAL}+E_{HCAL}}$	studied in Section 5.1
CorrEMF	$\frac{E_{ECAL}-E_{em}^{gen}}{E_{ECAL}+E_{HCAL}}$	relies by construction on MCTruth (true energy carried by em. particles E_{em}^{gen}), performs better than EMF
$\sigma_{\varphi\varphi}$	$\sigma_{\varphi\varphi}=\sqrt{\frac{\sum p_{T,\text{Calo}}^{i}\cdot(\varphi_i-\varphi_{\text{Calo-Jet}})^2}{\sum p_{T,\text{Calo}}^{i}}}$	studied in Section 5.3.1
$\sigma_{\eta\eta}$	$\sigma_{\eta\eta}=\sqrt{\frac{\sum p_{T,\text{Calo}}^{i}\cdot(\eta_i-\eta_{\text{Calo-Jet}})^2}{\sum p_{T,\text{Calo}}^{i}}}$	studied in Section 5.3.2
$\sigma_{\varphi\varphi}^{\text{ECAL}}$	$\sigma_{\varphi\varphi}=\sqrt{\frac{\sum p_{T,\text{Calo}}^{i,ECAL}\cdot(\varphi_i-\varphi_{\text{Calo-Jet}})^2}{\sum p_{T,\text{Calo}}^{i}}}$	mentioned in Section 5.4, like $\sigma_{\varphi\varphi}$, but restricted to ECAL.
$\sigma_{\varphi\varphi}^{\text{HCAL}}$	$\sigma_{\varphi\varphi}=\sqrt{\frac{\sum p_{T,\text{Calo}}^{i,HCAL}\cdot(\varphi_i-\varphi_{\text{Calo-Jet}})^2}{\sum p_{T,\text{Calo}}^{i}}}$	mentioned in Section 5.4, like $\sigma_{\varphi\varphi}$, but restricted to HCAL.
$E_{rel}^{\text{EMF}_{tow}=0}$	$\frac{\sum_i^{\text{EMF}=0} E_{tower}^{i}}{E_{jet,raw}}$	studied in Section 5.2
$E_{rel}^{\text{EMF}_{tow}=1}$	$\frac{\sum_i^{\text{EMF}=1} E_{tower}^{i}}{E_{jet,raw}}$	studied in Section 5.2

$E_{rel}^{\mathrm{EMF}_{tow}=0\cdots 1}$	$\frac{\sum_i^{\mathrm{EMF}=0\cdots 1} E_{tower}^i}{E_{jet,raw}}$	studied in Section 5.2
A	$-0.7485 \cdot \sigma_{\varphi\varphi} + (-0.6631) \cdot \sigma_{\eta\eta}$	studied in Section 5.5.1
B	$(-0.6631) \cdot \sigma_{\varphi\varphi} + 0.7485 \cdot \sigma_{\eta\eta}$	studied in Section 5.5.1
JW	$JW = \frac{\sigma_{\varphi\varphi}+\sigma_{\eta\eta}}{2}$	studied in Section 5.5.2
-	$\sigma_{\eta\eta}^2 + \sigma_{\varphi\varphi}^2$	not better than JW
-	$\sqrt{\sigma_{\eta\eta}^2 + \sigma_{\varphi\varphi}^2}$	not better than JW
σ_R	$\sigma_R = \sqrt{\frac{\sum p_{T,\mathrm{Calo}}^i \cdot (\Delta R(\mathrm{Tower,Jet}))^2}{\sum p_{T,\mathrm{Calo}}^i}}$	worse performance than JW
σ_R^{norm}	$\sigma_R = \sqrt{\frac{\sum \frac{p_{T,\mathrm{Calo}}^i}{area} \cdot (\Delta R(\mathrm{Tower,Jet}))^2}{\sum \frac{p_{T,\mathrm{Calo}}^i}{area}}}$	energy depositions scaled by area of annulus corresponding to the tower; not better than JW
-	$\frac{\sigma_{\eta\eta}^2+\sigma_{\varphi\varphi}^2}{\sigma_{\varphi\varphi}}$	not better than JW
-	$\sigma_{\varphi\varphi} + E_{rel}^{\mathrm{EMF}_{tow}=1}$	not better than $\sigma_{\varphi\varphi}$ variable
-	$\frac{\sigma_{\varphi\varphi}}{\sigma_{\varphi\varphi}^{\mathrm{ECAL}}}$	not better than $\sigma_{\varphi\varphi}$ variable
$E_{rel,gen}^{\mathrm{EMF}_{tow}=1}$	$\frac{\sum_i^{\mathrm{EMF}=1} E_{tower}^i}{E_{jet,gen}}$	artificially enhanced performance in comparison to $E_{rel}^{\mathrm{EMF}_{tow}=1}$ for a binning in p_T^{gen}, for binning in p_T^{L2L3} no significantly better performance.
$E_{rel,L2L3}^{\mathrm{EMF}_{tow}=1}$	$\frac{\sum_i^{\mathrm{EMF}=1} E_{tower}^i}{E_{jet,L2L3}}$	same performance as $E_{rel}^{\mathrm{EMF}_{tow}=1}$

Table A.1.: Potential candidate variables under study

Appendix B.

p_T-dependence of parameters b, c, μ_{JW}, and σ_{JW}

In the following, the p_T-dependence of the correction parameters as given by bin-by-bin corrections with binning in $p_T^{gen}$is shown as in Section 6.3 for all η-regions and as a function of p_T^{L2L3}.

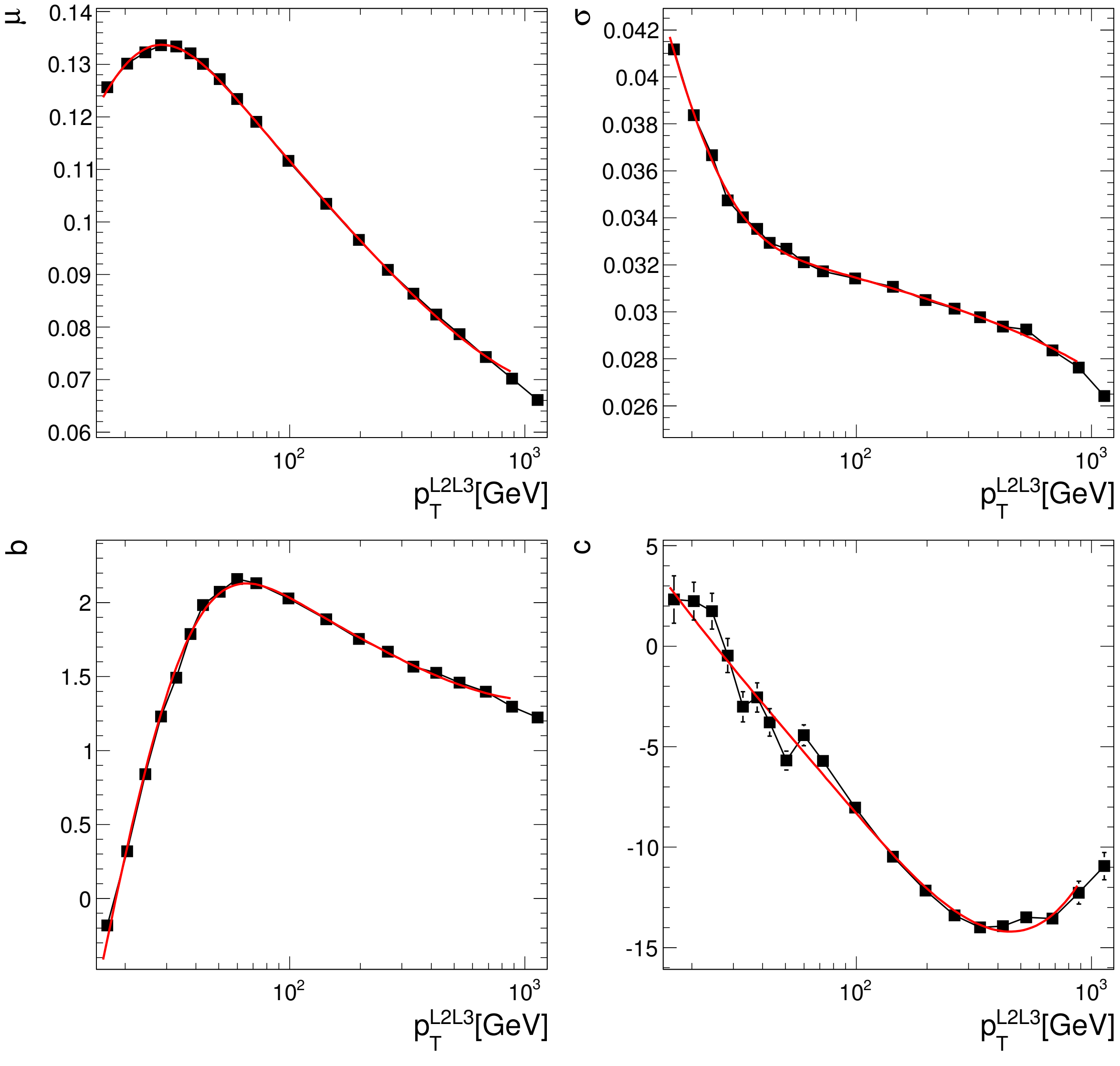

Figure B.1.: The p_T^{L2L3}-dependence of the four parameters b, c, σ, μ of the correction function in the barrel region ($0 < |\eta| < 1.305$) fitted with function from eq. 6.8.

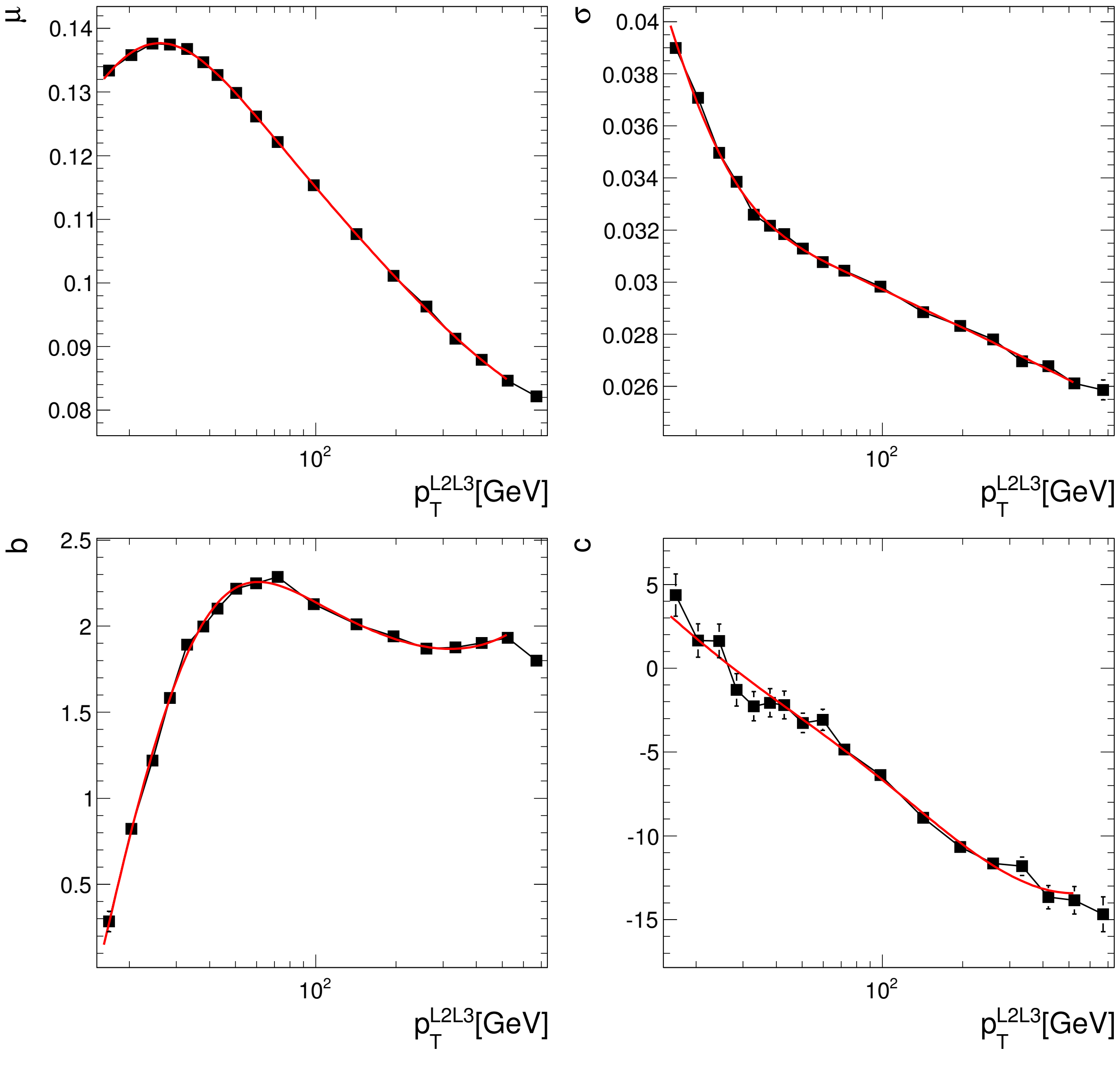

Figure B.2.: The p_T^{L2L3}-dependence of the four parameters b, c, σ, μ of the correction function in the endcap region ($1.305 < |\eta| < 2.65$) fitted with function from eq. 6.8.

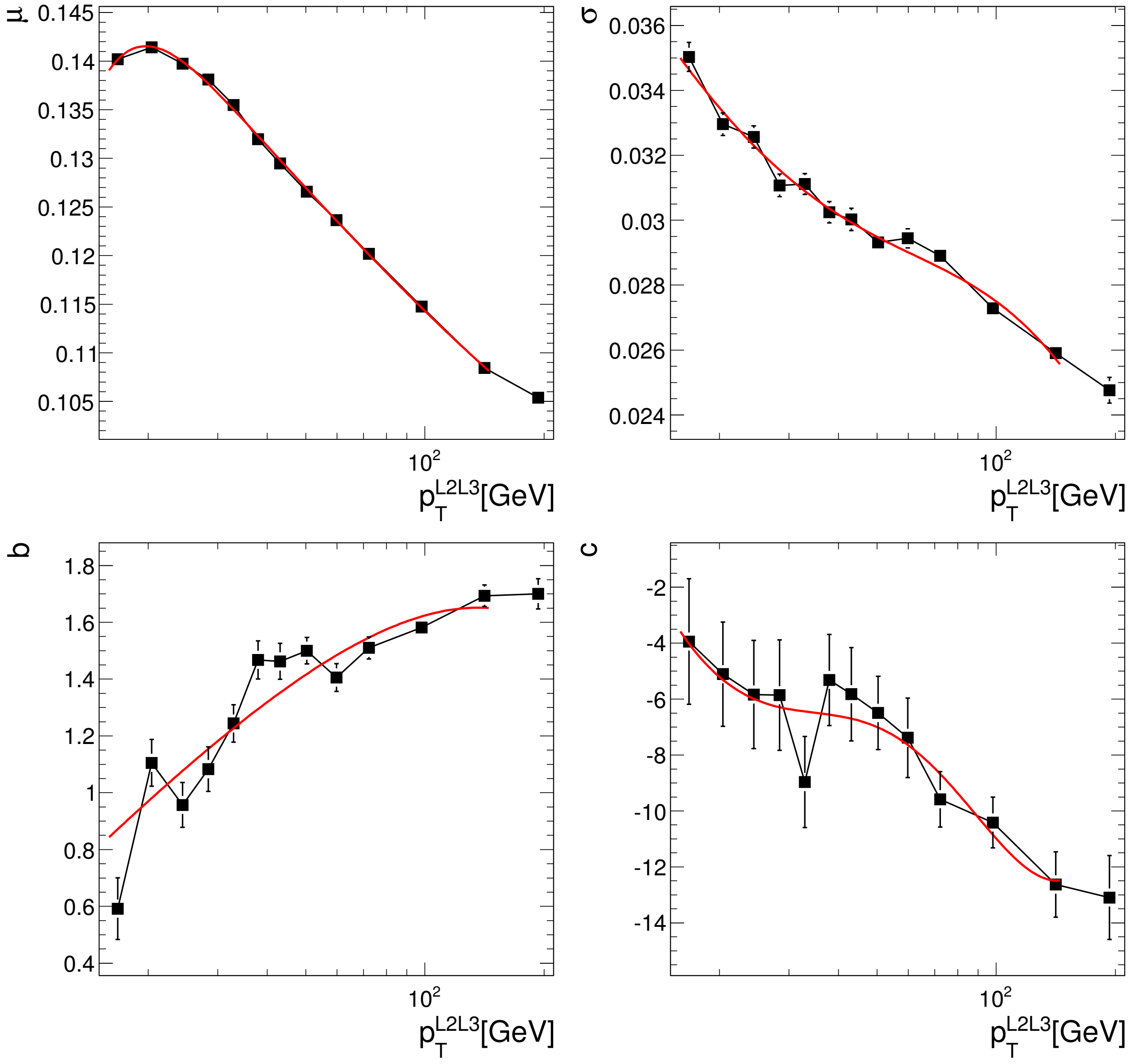

Figure B.3.: The p_T^{L2L3}-dependence of the four parameters b, c, σ, μ of the correction function in the hadron endcap region ($2.65 < |\eta| < 2.964$) fitted with function from eq. 6.8.

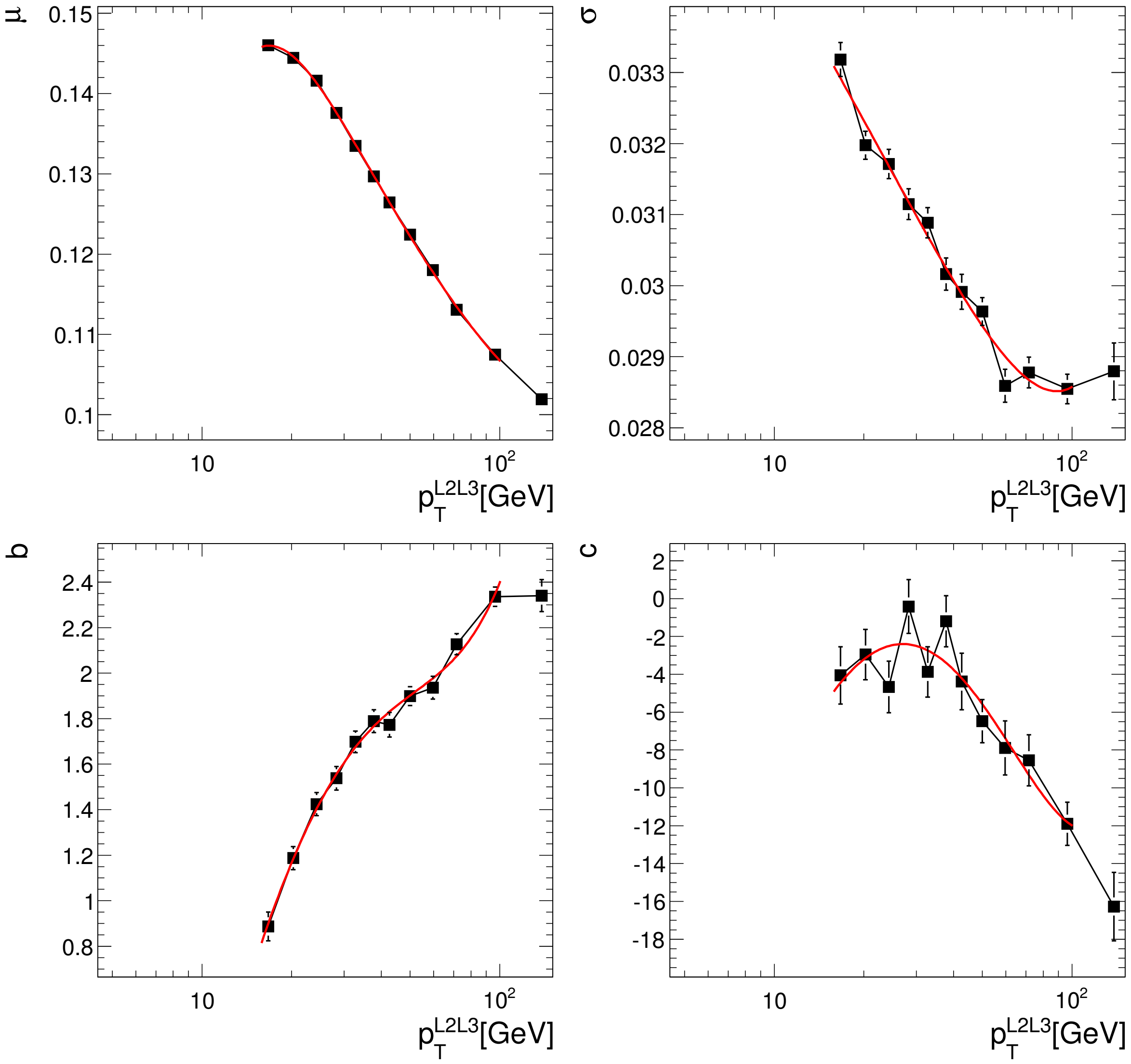

Figure B.4.: The p_T^{L2L3}-dependence of the four parameters b, c, σ, μ of the correction function in the forward region ($2.964 < |\eta| < 5.191$) fitted with function from eq. 6.8.

Appendix C.

Segmentation of HCAL towers

Tower index	η range		Detector	Size		Depth segments
	Low	High		η	ϕ	
1	0.000	0.087	HB, HO	0.087	5°	HB=1, HO=1
2	0.087	0.174	HB, HO	0.087	5°	HB=1, HO=1
3	0.174	0.261	HB, HO	0.087	5°	HB=1, HO=1
4	0.261	0.348	HB, HO	0.087	5°	HB=1, HO=1
5	0.348	0.435	HB, HO	0.087	5°	HB=1, HO=1
6	0.435	0.522	HB, HO	0.087	5°	HB=1, HO=1
7	0.522	0.609	HB, HO	0.087	5°	HB=1, HO=1
8	0.609	0.696	HB, HO	0.087	5°	HB=1, HO=1
9	0.696	0.783	HB, HO	0.087	5°	HB=1, HO=1
10	0.783	0.870	HB, HO	0.087	5°	HB=1, HO=1
11	0.879	0.957	HB, HO	0.087	5°	HB=1, HO=1
12	0.957	1.044	HB, HO	0.087	5°	HB=1, HO=1
13	1.044	1.131	HB, HO	0.087	5°	HB=1, HO=1
14	1.131	1.218	HB, HO	0.087	5°	HB=1, HO=1
15	1.218	1.305	HB, HO	0.087	5°	HB=2, HO=1
16	1.305	1.392	HB, HE	0.087	5°	HB=2, HE=1
17	1.392	1.479	HE	0.087	5°	HE=1
18	1.479	1.566	HE	0.087	5°	HE=2
19	1.566	1.653	HE	0.087	5°	HE=2
20	1.653	1.740	HE	0.087	5°	HE=2
21	1.740	1.830	HE	0.090	10°	HE=2
22	1.830	1.930	HE	0.100	10°	HE=2
23	1.930	2.043	HE	0.113	10°	HE=2
24	2.043	2.172	HE	0.129	10°	HE=2

25	2.172	2.322	HE	0.150	10°	HE=2
26	2.322	2.500	HE	0.178	10°	HE=2
27	2.500	2.650	HE	0.150	10°	HE=3
*28	2.650	3.000	HE	0.350	10°	HE=3
29	2.853	2.964	HF	0.111	10°	HF=2
30	2.964	3.139	HF	0.175	10°	HF=2
31	3.139	3.314	HF	0.175	10°	HF=2
32	3.314	3.489	HF	0.175	10°	HF=2
33	3.489	3.664	HF	0.175	10°	HF=2
34	3.664	3.839	HF	0.175	10°	HF=2
35	3.839	4.013	HF	0.174	10°	HF=2
36	4.013	4.191	HF	0.178	10°	HF=2
37	4.191	4.363	HF	0.172	10°	HF=2
38	4.363	4.538	HF	0.175	10°	HF=2
39	4.538	4.716	HF	0.178	10°	HF=2
40	4.716	4.889	HF	0.173	20°	HF=2
41	4.889	5.191	HF	0.302	20°	HF=2

Table C.1.: Sizes of the HCAL readout towers in η and ϕ as well as the segmentation in depth. The HF has a non-pointing geometry, and therefore the tower η ranges provided here correspond to $|z| = 11.2$ m. *The first two depth segments of tower 28 have a finer η segmentation, divided at $|\eta| = 2.868$; table taken from [59]

Appendix D.

Parameter tables

Table D.1.: Fixed parameters for μ_{JW} and σ_{JW}

μ_{JW} parameters	α	β	γ	δ	ϵ
$0. < \|\eta\| < 1.305$	2.22197	-2.43273	0.161247	-1.8384	-1.12056
$1.305 < \|\eta\| < 2.65$	2.211	-2.34235	0.196643	-1.71561	-1.20111
$2.65 < \|\eta\| < 2.964$	2.09358	-2.15426	0.409124	-2.36072	-2.00319
$2.964 < \|\eta\| < 5.192$	-1.83367	7.87148	-7.93116	2.17698	-0.351629
σ_{JW} parameters					
$0. < \|\eta\| < 1.305$	3.76558	-1.28309	-1.21227	4.97975	-1.06063
$1.305 < \|\eta\| < 2.65$	4.04847	-2.31725	0.363659	4.69276	-1.1739
$2.65 < \|\eta\| < 2.964$	15.1794	-29.3188	141.953	-5.74235	-0.27755
$2.964 < \|\eta\| < 5.192$	4.34203	-3.78074	24.1966	4477.12	-8.18597

Table D.2.: Results of fit for parameters b and c

b parameters	α	β	γ	δ	ϵ
$0. < \|\eta\| < 1.305$	3.56585	-2.94696	-4.14987	-1.29651	-8.37254
$1.305 < \|\eta\| < 2.65$	4.23050	-4.64314	10.8783	-1.20905	-8.62383
$2.65 < \|\eta\| < 2.964$	0.278775	2.84047	2.78045	-3.75321	-23.5930
$2.964 < \|\eta\| < 5.192$	-1.26146	8.91478	-41.4318	-98.7111	-46.1337
c parameters					
$0. < \|\eta\| < 1.305$	2.37207	-7.57939	2.13660	141.489	-28.0435
$1.305 < \|\eta\| < 2.65$	2.84147	-8.14719	2.33879	52815.8	-103.224
$2.65 < \|\eta\| < 2.964$	-7.35154	-4.59322	5.01315	8.19059	-0.048455
$2.964 < \|\eta\| < 5.192$	3.09711	-12.6187	17.9219	0.393632	-1.69317

Bibliography

[1] D. Griffiths, “Introduction to Elementary Particles”. Wiley-VCH, 2nd edition, 10, 2008.

[2] B. Martin and G. Shaw, “Particle Physics (Manchester Physics Series)”. Wiley, 3 edition, 12, 2008.

[3] F. Halzen and A. D. Martin, “Quarks and Leptons: An Introductory Course in Modern Particle Physics”. Wiley, 1st edition, 1, 1984.

[4] M. E. Peskin and D. V. Schroeder, “An Introduction To Quantum Field Theory (Frontiers in Physics)”,.

[5] K. Nakamura et al. (Particle Data Group), “Review of Particle Physics, 2010-2011. Review of Particle Properties, 2010-2011”, *J. Phys. G* **37** (2010), no. 7A, 075021.

[6] W. Commons, “Sketch of elementary particles of the Standard Model of particle physics”, *Website* **`http://commons.wikimedia.org/wiki/File:Standard_Model_of_Elementary_Particles.svg`** (8 November 2010).

[7] M. Gell-Mann, “A schematic model of baryons and mesons”, *Physics Letters* **8** (1964), no. 3, 214 – 215. `doi:DOI: 10.1016/S0031-9163(64)92001-3`.

[8] Nobelprize.org, “The Nobel Prize in Physics 1979”, *Website* **`http://nobelprize.org/nobel_prizes/physics/laureates/1979/`** (8 November 2010).

[9] CDF, D0 Collaboration, Tevatron New Physics and Higgs Working Group, “Combined CDF and D0 Upper Limits on Standard Model Higgs-Boson Production with up to 6.7 fb-1 of Data”, *ArXiv e-prints* (July, 2010) `arXiv:1007.4587`.

[10] S. P. Martin, “A Supersymmetry Primer”, in *Perspectives on Supersymmetry*, G. L. Kane, ed., pp. 1–+. 1998. `arXiv:arXiv:hep-ph/9709356`.

[11] J. Ellis and D. V. Nanopoulos, “Beyond the Standard Model of Cosmology”, in *The New Cosmology: Conference on Strings and Cosmology*, R. E. Allen, D. V. Nanopoulos, & C. N. Pope, ed., volume 743 of *American Institute of Physics Conference Series*, pp. 450–456. December, 2004. `arXiv:arXiv:astro-ph/0411153`.

[12] J. Ellis, “New Light on Dark Matter from the LHC”, *ArXiv e-prints* (October, 2010) `arXiv:1011.0077`.

[13] G. Dissertori, I. Knowles, and M. Schmelling, “Quantum Chromodynamics: High Energy Experiments and Theory (The International Series of Monographs on Physics)”. Oxford University Press, USA, 4, 2003.

[14] R. K. Ellis, W. J. Stirling, and B. R. Webber, “QCD and Collider Physics (Cambridge Monographs on Particle Physics, Nuclear Physics and Cosmology)”. Cambridge University Press, 12, 2003.

[15] G. Sterman and S. Weinberg, “Jets from Quantum Chromodynamics”, *Phys. Rev. Lett.* **39** (Dec, 1977) 1436–1439. `doi:10.1103/PhysRevLett.39.1436`.

[16] M. A. Dobbs, S. Frixione, E. Laenen et al., “Les Houches Guidebook to Monte Carlo Generators for Hadron Collider Physics”, *ArXiv e-prints* (March, 2004) `arXiv:arXiv:hep-ph/0403045`.

[17] B. Heinemann, “Physics at Hadron Colliders”, *CERN Summer Student Lecture Programme 2009* **`http://indico.cern.ch/scripts/SSLPdisplay.py?stdate=2009-06-29&nbweeks=8`**.

[18] J. C. Collins, D. E. Soper, and G. Sterman, “Factorization of Hard Processes in QCD”, *ArXiv e-prints* (September, 2004) `arXiv:arXiv:hep-ph/0409313`.

[19] J. M. Campbell, J. W. Huston, and W. J. Stirling, “Hard interactions of quarks and gluons: a primer for LHC physics”, *Reports on Progress in Physics* **70** (2007), no. 1, 89.

[20] T. Sjöstrand, S. Mrenna, and P. Skands, “PYTHIA 6.4 Physics and Manual”, `arXiv:hep-ph/0603175`. `doi:10.1088/1126-6708/2006/05/026`.

[21] M. Bähr, S. Gieseke, M. A. Gigg et al., “Herwig++ physics and manual”, *European Physical Journal C* **58** (December, 2008) 639–707, `arXiv:0803.0883`. `doi:10.1140/epjc/s10052-008-0798-9`.

[22] M. L. Mangano, F. Piccinini, A. D. Polosa et al., “ALPGEN, a generator for hard multiparton processes in hadronic collisions”, *Journal of High Energy Physics* **2003** (2003), no. 07, 001.

[23] J. Alwall, P. Demin, S. de Visscher et al., “MadGraph/MadEvent v4: the new web generation”, *Journal of High Energy Physics* **2007** (2007), no. 09, 028.

[24] V. N. Gribov and L. N. Lipatov, “Deep inelastic e p scattering in perturbation theory”, *Sov. J. Nucl. Phys.* **15** (1972) 438–450.

[25] T. Sjöstrand and A. de Roeck, “Monte Carlo generators for the LHC”, *CDS* **`http://cdsweb.cern.ch/record/794322`** (2005) Streaming video ; transparencies ; 4 DVD video. CERN, Geneva, 4 - 7 Apr 2005.

[26] G. Alexander, J. Allison, N. Altekamp et al., “A comparison of b and uds quark jets to gluon jets”, *Zeitschrift für Physik C Particles and Fields* **69** (1995) 543–560. `doi:10.1007/BF02907439`.

[27] OPAL Collaboration, “A model independent measurement of quark and gluon jet properties and differences”, *Zeitschrift für Physik C Particles and Fields* **68** (1995) 179–201. `doi:10.1007/BF01566667`.

[28] DELPHI Collaboration, “Investigation of the splitting of quark and gluon jets”, *The European Physical Journal C - Particles and Fields* **4** (1998) 1–17. `doi:10.1007/s100529800885`.

[29] CMS Collaboration, “Jet Transverse Structure and Momentum Distribution in pp Collisions at 7 TeV”, *CMS-PAS-QCD-10-014* **`http://cdsweb.cern.ch/record/1280685`** (2010).

[30] T. Kluge, K. Rabbertz, and M. Wobisch, “fastNLO: Fast pQCD Calculations for PDF Fits”, *ArXiv High Energy Physics - Phenomenology e-prints* (September, 2006) `arXiv:arXiv:hep-ph/0609285`.

[31] J. Huston, “LHC Guide to Parton Distributions and Cross Sections”, *ATL-PHYS-99-008* **`http://cdsweb.cern.ch/record/683851`** (Apr, 1999).

[32] R. Wigmans, “Calorimetry: Energy Measurement in Particle Physics”. International series of monographs on physics. Clarendon Press, Oxford, 2000.

[33] K. Nakamura et al. (Particle Data Group), “Passage of Particle Through Matter”, *J. Phys. G* **37** (2010), no. 7A, 285ff.

[34] K. Nakamura et al. (Particle Data Group), “Particle Detectors at Accelerators”, *J. Phys. G* **37** (2010), no. 7A, 300ff.

[35] R. K. Bock and A. Vasilescu, “The Particle Detector BriefBook”. Springer, 1998.

[36] R. Wigmans, “Calorimetry”, *AIP Conference Proceedings* **674** (2003), no. 1, 144–168. `doi:10.1063/1.1604077`.

[37] D. E. Groom, “A simplistic view of hadron calorimetry”, *AIP Conference Proceedings* **896** (2007), no. 1, 137–149. `doi:10.1063/1.2720464`.

[38] T. S. Virdee, “Experimental techniques”, *CERN-OPEN-2000-261* **`http://cdsweb.cern.ch/record/454176?ln=de`** (2000).

[39] SLAC, “EGS: Basic Simulation Tool”, *Website* **`http://www2.slac.stanford.edu/VVC/egs/basicsimtool.html`** (2010).

[40] C. W. Fabjan and T. Ludlam, “Calorimetry in high-energy physics”, *Ann. Rev. Nucl. Part. Sci.* **32** (1982) 335–389.

[41] CALICE Collaboration, “A high granularity calorimeter system optimised for the particle flow measurement of multi-jet final states at the ILC”, *Twiki* **`https://twiki.cern.ch/twiki/bin/view/CALICE/WebHome`** (2010).

[42] R. Wigmans, “The DREAM project–Towards the ultimate in calorimetry”, *Nuclear Instruments and Methods in Physics Research Section A: Accelerators,*

Spectrometers, Detectors and Associated Equipment **617** (2010), no. 1-3, 129 – 133. 11th Pisa Meeting on Advanced Detectors - Proceedings of the 11th Pisa Meeting on Advanced Detectors. `doi:DOI: 10.1016/j.nima.2009.09.118`.

[43] E. Bruning et al., "LHC design report. Vol. I: The LHC main ring", *CDS* **`http://cdsweb.cern.ch/record/782076`** (2004). CERN-2004-003-V-1.

[44] L. Evans and P. Bryant, "LHC Machine", *Journal of Instrumentation* **3** (2008), no. 08, S08001.

[45] T. S. Virdee, "Universal Laws, The Big Bang and Particle Physics part 2", *ECIS conference in the Hague* **`http://cms.web.cern.ch/cms/Resources/Website/Media/Presentations/files/Hague2.pdf`** (2001).

[46] D0 Collaboration Collaboration, "Search for High Mass Top Quark Production in $p\bar{p}$ Collisions at $\sqrt{s} = 1.8$ TeV", *Phys. Rev. Lett.* **74** (Mar, 1995) 2422–2426. `doi:10.1103/PhysRevLett.74.2422`.

[47] CDF Collaboration Collaboration, "Observation of Top Quark Production in $p\bar{p}$ Collisions with the Collider Detector at Fermilab", *Phys. Rev. Lett.* **74** (Apr, 1995) 2626–2631. `doi:10.1103/PhysRevLett.74.2626`.

[48] LEP EWWG, "The LEP Electroweak Working Group", *Website* **`http://lepewwg.web.cern.ch/LEPEWWG/`** (2010).

[49] The ALEPH Collaboration, The DELPHI Collaboration, The L3 Collaboration et al., "Precision electroweak measurements on the Z resonance", *Phys. Rep.* **427** (May, 2006) 257–454, `arXiv:arXiv:hep-ex/0509008`. `doi:10.1016/j.physrep.2005.12.006`.

[50] C. Lefvre, "The CERN accelerator complex. Complexe des acclrateurs du CERN", *CDS* **`http://cdsweb.cern.ch/record/1260465`** (Dec, 2008).

[51] ATLAS Collaboration, "ATLAS detector and physics performance : Technical Design Report, 1", *ATLAS-TDR-014; CERN-LHCC-99-014* **`http://cdsweb.cern.ch/record/391176`** (1999) 460.

[52] P. Cortese, C. W. Fabjan, L. Riccati et al., "ALICE physics performance: Technical Design Report". Technical Design Report ALICE. CERN, Geneva, 2005. revised version submitted on 2006-05-29 15:15:40.

[53] LHCb, "Technical Design Reports", *Website* **`http://lhcb.web.cern.ch/lhcb/TDR/TDR.htm`** (2010).

[54] O. Adriani, L. Bonechi, M. Bongi et al., "LHCf experiment: Technical Design Report". Technical Design Report LHCf. CERN, Geneva, 2006.

[55] V. Berardi, M. G. Catanesi, E. Radicioni et al., "Total cross-section, elastic scattering and diffraction dissociation at the Large Hadron Collider at CERN: TOTEM Technical Design Report". Technical Design Report TOTEM. CERN,

Geneva, 2004.

[56] CMS Collaboration, “CMS 3-D image for inclusion in presentations - white background”, *CMS Document 2716-v3* **https://cms-docdb.cern.ch/cgi-bin/DocDB/ShowDocument?docid=2716** (2010).

[57] CMS Collaboration, “Slice through the detector with particle trajectories”, *CDS* **http://cms.web.cern.ch/cms/Resources/Website/Media/Videos/Animations/files/CMS_Slice.gif** (2007).

[58] CMS Collaboration, “CMS technical design report, volume II: Physics performance”, *J. Phys.* **G34** (2007) 995–1579. doi:10.1088/0954-3899/34/6/S01.

[59] CMS Collaboration, “CMS Physics Technical Design Report Volume I: Detector Performance and Software”, *CERN-LHCC-2006-001; CMS-TDR-008-1* **http://cmsdoc.cern.ch/cms/cpt/tdr/** (2006).

[60] CMS Collaboration Collaboration, “The CMS experiment at the CERN LHC”, *JINST* **3** (2008) S08004. doi:10.1088/1748-0221/3/08/S08004.

[61] CMS Collaboration, “CMS ECAL Technical Design Report”, *CERN/LHCC 97-33* **http://cmsdoc.cern.ch/cms/TDR/ECAL/ecal.html** (1997).

[62] P. Jenni, M. Nessi, M. Nordberg et al., “ATLAS high-level trigger, data-acquisition and controls: Technical Design Report”, *ATLAS-TDR-016; CERN-LHCC-2003-022* **http://cdsweb.cern.ch/record/616089** (2003).

[63] L. Rossi, “Superconductivity: its role, its success and its setbacks in the Large Hadron Collider of CERN”, *Superconductor Science and Technology* **23** **http://stacks.iop.org/0953-2048/23/i=3/a=034001** (2010), no. 3, 034001.

[64] CMS Collaboration, “CMS Physics Results”, *Twiki* **https://twiki.cern.ch/twiki/bin/view/CMSPublic/PhysicsResults** (2010).

[65] ATLAS Collaboration, “ATLAS Experiment - Public Results”, *Twiki* **https://twiki.cern.ch/twiki/bin/view/Atlas/AtlasResults** (2010).

[66] CMS Collaboration, “Observation of long-range, near-side angular correlations in proton-proton collisions at the LHC”, *Journal of High Energy Physics* **2010** (2010) 1–38. 10.1007/JHEP09(2010)091.

[67] M. Lamont, “LHC report”, *Indico* **http://indico.cern.ch/conferenceDisplay.py?confId=113256** (12 November 2010).

[68] CMS Collaboration, “Luminosity Overview”, *CMS* **http:**

//cms-service-lumi.web.cern.ch/cms-service-lumi/overview.php (12 November 2010).

[69] S. Agostinelli, J. Allison, K. Amako et al., “G4–a simulation toolkit”, *Nuclear Instruments and Methods in Physics Research Section A: Accelerators, Spectrometers, Detectors and Associated Equipment* **506** (2003), no. 3, 250 – 303. `doi:10.1016/S0168-9002(03)01368-8`.

[70] Matthias Schröder, “Private communication”,.

[71] Gavin P. Salam, “Towards jetography”, *Eur. Phys. J. C* **67** (2010), no. 3-4, 637–686. `doi:10.1140/epjc/s10052-010-1314-6`.

[72] M. Cacciari, G. Salam, and G. Soyez, “FastJet package for jet algorithms”, *Website* **www.fastjet.fr** (2010).

[73] M. Cacciari, G. P. Salam, and G. Soyez, “The anti-k_t jet clustering algorithm”, *Journal of High Energy Physics* **http://stacks.iop.org/1126-6708/2008/i=04/a=063** (2008), no. 04, 063.

[74] G. P. Salam and G. Soyez, “A practical seedless infrared-safe cone jet algorithm”, *Journal of High Energy Physics* **5** (May, 2007) 86–+, `arXiv:0704.0292`. `doi:10.1088/1126-6708/2007/05/086`.

[75] V. Chetluru, J. Hirschauer, K. Ozdemir et al., “Update of calorimeter cell and tower thresholds for jet reconstruction in first CMS collision data”, *CMS AN 2010/024* **http://cms.cern.ch/iCMS/jsp/db_notes/noteInfo.jsp?cmsnoteid=CMS%20AN-2010/024** (2010).

[76] CMS Collaboration, “The Jet Plus Tracks Algorithm for Calorimeter Jet Energy Corrections in CMS”, *CMS PAS JME-09/023* **http://cdsweb.cern.ch/record/1190234** (2009).

[77] CMS Collaboration, “Particle-Flow Event Reconstruction in CMS and Performance for Jets, Taus, and MET”, *CMS PAS PFT-09/001* **http://cdsweb.cern.ch/record/1194487** (2009).

[78] CMS Collaboration, “Commissioning of the Particle-Flow reconstruction in Minimum-Bias and Jet Events from pp Collisions at 7 TeV”, *CMS PAS PFT-10/002* **http://cdsweb.cern.ch/record/1279341** (2010).

[79] S. Esen, G. Landsberg, G. Dissertori et al., “Plans for Jet Energy Corrections”, *CMS AN 2007/055* **http://cms.cern.ch/iCMS/jsp/openfile.jsp?tp=draft&files=AN2007_055_v3.pdf** (2007).

[80] CMS Collaboration, “Determination of the Jet Energy Scale in CMS with pp Collisions at $s = \sqrt{7}$ TeV”, *CMS PAS JME-10-010* **http://cdsweb.cern.ch/record/1308178** (2010).

[81] CMS Collaboration, “Offset Energy Correction for Cone Jets”, *CMS AN 2010/150*

http://cms.cern.ch/iCMS/jsp/db_notes/noteInfo.jsp?cmsnoteid=CMS%20AN-2010/150 (2010).

[82] A. Moraes, C. Buttar, and I. Dawson, “Prediction for minimum bias and the underlying event at LHC energies”, *Eur. Phys. J. C* **50** (2007), no. 2, 435–466. doi:10.1140/epjc/s10052-007-0239-1.

[83] CMS Collaboration, “Zero bias and HF-based minimum bias triggering for pp collisions at 14 TeV in CMS”, *CMS-PAS-QCD-07-002* **http://cdsweb.cern.ch/record/1152558/** (2010).

[84] R. Harris and K. Kousouris, “MC Truth L2 & L3 Factorized Jet Corrections at CMS”, *CMS AN 2008/003* **http://cms.cern.ch/iCMS/jsp/openfile.jsp?tp=draft&files=AN2008_003_v3.pdf** (2008).

[85] CMS Collaboration, “Constants and Parametrisations of Factorised Jet Energy Corrections”, *Website* **http://cmslxr.fnal.gov/lxr/source/CondFormats/JetMETObjects/data/** (2010).

[86] S. Esen and G. Landsberg, “MC Truth L4 EMF-Based Factorized Jet Corrections in CMS”, *CMS AN 2009/013* **http://cms.cern.ch/iCMS/jsp/openfile.jsp?tp=draft&files=AN2009_013_v2.pdf** (2009).

[87] K. Kousouris, “Update of the L4EMF correction for CaloJets”, *CMS Jet Energy Corrections Meeting* **http://indico.cern.ch/conferenceOtherViews.py?view=standard&confId=80699** (2010).

[88] CMS Collaboration, “Jet Flavour identification (MC truth)”, *CMS-TWiki* **https://twiki.cern.ch/twiki/bin/view/CMS/SWGuideBTagMCTools** (2010).

[89] J. Cammin, “Flavor Specific Jet Energy Corrections and Closure Tests for Factorized Jet Energy Corrections”, *CMS AN 2009/010* **http://cms.cern.ch/iCMS/jsp/openfile.jsp?tp=draft&files=AN2009_010_v2.pdf** (2009).

[90] S. Naumann-Emme, P. Schleper, H. Stadie et al., “Validation of the Jet Energy Corrections in Simulated Events with Top Quarks”, *CMS AN 2010/094* **http://cms.cern.ch/iCMS/jsp/db_notes/noteInfo.jsp?cmsnoteid=CMS%20AN-2010/094** (2010).

[91] A. Santocchia, “Parton Jet Correction”, *CMS AN 2008/084* **http://cms.cern.ch/iCMS/jsp/db_notes/noteInfo.jsp?cmsnoteid=CMS%20AN-2008/084** (2009).

[92] M. Voutilainen, F. Pandol, and D. del Re, “Particle Flow jet calibration with γ+jet events: p_T balance and missing-E_T projection fraction”, *CMS AN 2010/218* **http://cms.cern.ch/iCMS/jsp/openfile.jsp?tp=draft&files=AN2010_218_v1.pdf** (2010).

[93] R. M. Harris, K. Mishra, D. del Re et al., “Jet Energy Correction Using $Z \rightarrow (e^+e^-)$ + Jet p_T Balance and the Method for Combining Data Driven Corrections”, *CMS AN 2009/004* `http://cms.cern.ch/iCMS/jsp/db_notes/noteInfo.jsp?cmsnoteid=CMS%20AN-2009/004` (2009).

[94] V. Buge, D. Piparo, G. Quast et al., “Calibration of the absolute jet energy scale with $Z \rightarrow (\mu^+\mu^-)+$ jet events at CMS”, *CMS AN 2009/057* `http://cms.cern.ch/iCMS/jsp/db_notes/noteInfo.jsp?cmsnoteid=CMS%20AN-2009/057` (2009).

[95] K. Kousouris, “Measurement of the Relative Jet Energy Scale in CMS with pp Collisions at 7 TeV”, *CMS AN 2010/139* `http://cms.cern.ch/iCMS/jsp/db_notes/noteInfo.jsp?cmsnoteid=CMS%20AN-2010/139` (2010).

[96] University of Hamburg CMS group, “Kalibri Framework”, *CMS-TWiki* `https://twiki.cern.ch/twiki/bin/view/CMS/HamburgWikiAnalysisCalibration` (2010).

[97] V. Blobel, “Large-scale optimization with the limited-memory BFGS program LVMINI”, *Website* `http://www.desy.de/~blobel/largesc.html` (2007).

[98] J. Nocedal, “Updating Quasi-Newton Matrices with Limited Storage”, *Mathematics of Computation* **35** (1980) 773–782.

[99] Z. Qi, “Updating Cell Thresholds for the CMS Detector”, *Thesis, University of Rochester* `http://home.fnal.gov/~zqi/Threshold09/thesis_qi.pdf` (May 2009).

[100] CMS Collaboration, “Energy Response and Longitudinal Shower Profiles Measured in CMS HCAL and Comparison With Geant4”, Technical Report CMS-NOTE-2006-143. CERN-CMS-NOTE-2006-143, CERN, Geneva, May, 2007.

[101] CMS Collaboration, “Single-Particle Response in the CMS Calorimeters”, *CMS-PAS-JME-10-008* `http://cdsweb.cern.ch/record/1279141/?ln=de` (2010).

[102] C. Günter, “Studies of Single Hadron Calibration of the CMS Calorimeter”, *CMS-TS-2008/027* `http://cms.cern.ch/iCMS/jsp/db_notes/noteInfo.jsp?cmsnoteid=CMS%20TS-2008/027` (2008).

[103] CMS Collaboration, “Identification and filtering of uncharacteristic noise in the CMS hadron calorimeter”, *Journal of Instrumentation* **5** (2010), no. 03, T03014. `doi:10.1088/1748-0221/5/03/T03014`.

[104] B. Kolodzey, “Studie zur Flavour-Abhängigkeit von Jet-Korrekturen zum CMS-Kalorimeter bei LHC - Studies on the flavour dependence of jet energy corrections for the CMS calorimeters”, *Diploma Thesis, University of Hamburg* **N 4/4015, H47 Diplomarbeit** (2010) 155.

[105] R. Harris and K. Kousouris, "Determination of the Relative Jet Energy Scale at CMS from Dijet Balance", *CMS AN 2008/031* **http://cms.cern.ch/iCMS/jsp/db_notes/noteInfo.jsp?cmsnoteid=CMS%20AN-2008/031** (2009).

[106] R. M. Harris, "Jet Calibration from Dijet Balancing", *CMS AN 2005/034* **http://cms.cern.ch/iCMS/jsp/db_notes/noteInfo.jsp?cmsnoteid=CMS%20AN-2005/034** (2005).

[107] C. Autermann, C. Sander, P. Schleper et al., "Measurement of the Jet p_T Response Function in QCD Dijet Events using an Unbinned Maximum Likelihood Method", *CMS AN 2010/341* **http://cms.cern.ch/iCMS/jsp/db_notes/noteInfo.jsp?cmsnoteid=CMS%20AN-2010/341** (2010).

[108] Hauke Held, Philipp Schieferdecker, and Mikko Voutilainen, "Jet p_T Resolutions with the Asymmetry-Method", *CMS JetMET Meeting* **http://indico.cern.ch/conferenceOtherViews.py?view=standard&confId=94577** (2010).

[109] A. Smoron, L. Apanasevich, N. Varelas et al., "Data-Driven Method for Obtaining the Jet p_T Resolution at CMS", *CMS AN 2009/061* **http://cms.cern.ch/iCMS/jsp/openfile.jsp?tp=draft&files=AN2009_061_v5.pdf** (2009).

[110] C. Dragoiu, H. Held, P. Schieferdecker et al., "Measurement of the Jet Energy Resolution in $\sqrt{s} = 7$ TeV Collision Data with the Asymmetry Method", *CMS AN 2010/134(v2)* **http://cms.cern.ch/iCMS/jsp/db_notes/noteInfo.jsp?cmsnoteid=CMS%20AN-2010/134** (2010).

[111] E. Albayrak, C. Autermann, A. Bhatti et al., "Measurement of the Full Jet Energy Resolution Function for SUSY Analysis", *CMS AN 2010/151* **http://cms.cern.ch/iCMS/jsp/openfile.jsp?tp=draft&files=AN2010_151_v2.pdf** (2010).

[112] CMS Collaboration, "Measurement of the Jet Energy Resolutions and Jet Reconstruction Efciency at CMS", *CMS PAS JME 2009/007* **cdsweb.cern.ch/record/1194493/files/JME-09-007-pas.pdf** (2009).

[113] Sebastian Naumann-Emme, "Private communication",.

Acknowledgements

I would like to thank all those who contributed to the formation of this diploma thesis. Many were directly involved, many others I will inevitably miss in this incomplete list. Thank you all for your encouraging support!

I would like to thank Prof. Dr. Peter Schleper and Prof. Dr. Robert Klanner for their helpful comments and for giving me the opportunity to work in the CMS-group of the University of Hamburg and to become part of a world-wide collaboration.

During the last year I have worked closely with Hartmut Stadie whom I would like to express my gratitude for his support, kindly providing help and insight on any topic within short notice. This work would not have been possible without you!

I have enjoyed getting to know all colleagues of the research group and like the lively discussions during lunch and coffee breaks. I am looking forward to more...

Many thanks to Steven Aplin, Friederike Januschek, and Matthias Schröder, who have proofread my thesis and provided very valuable comments. I hope I have incorporated your insights. Thank you, Steve, for pointing out my worst English language flaws.

While it was the first time that I have worked with the CMS detector so closely over a long time, I have already touched upon the experiment before. I would like to thank the Imperial College CMS-group and Torsten Dahms for granting me more than just a glimpse at CMS during my stay in London and as a summer student at CERN.

The scholarship of the “Friedrich-Ebert-Stiftung” has been very valuable during the last years; I have enjoyed the seminars and enlightening discussions and was able to make the most of my University studies.

I would like to deeply thank my family, especially my girlfriend Stefanie; it reassures me that I can always count on you all. Over all the years, you have made me the person I am.